UC Santa Barbara

UC Santa Barbara Electronic Theses and Dissertations

Title

Molecular beam epitaxy of Group V-based materials with strong spin-orbit coupling

Permalink

https://escholarship.org/uc/item/1g92t4d5

Author

Dong, Jason Tianming

Publication Date

2024

Peer reviewed|Thesis/dissertation

eScholarship.org Powered by the California Digital Library
University of California

University of California
Santa Barbara

Molecular beam epitaxy of Group V-based materials with strong spin-orbit coupling

A dissertation submitted in partial satisfaction
of the requirements for the degree

Doctor of Philosophy
in
Materials

by

Jason Tianming Dong

Committee in charge:

Professor Christopher Palmstrøm, Chair
Professor James Speck
Professor Stephen Wilson
Professor Kunal Mukherjee

September 2024

The Dissertation of Jason Tianming Dong is approved.

Professor James Speck

Professor Stephen Wilson

Professor Kunal Mukherjee

Professor Christopher Palmstrøm, Committee Chair

June 2024

Molecular beam epitaxy of Group V-based materials with strong spin-orbit coupling

Copyright © 2024

by

Jason Tianming Dong

Acknowledgements

First and foremost, I would like to acknowledge my advisor, Professor Chris Palmstrøm. His knowledge in molecular beam epitaxy has been invaluable during my time here at UC Santa Barbara. His guidance has helped develop me into a better researcher and scientist. I would also like to acknowledge my committee members, Professor James Speck, Professor Stephen Wilson, and Professor Kunal Mukherjee for their advise and suggestions during the course of my PhD. Their questions have helped me gain a deeper insight into the materials systems I have worked on.

I would also like to acknowledge the help from the other Palmstrøm group members during my PhD. I would not have made any progress without the help from the other Palmstroøm group members in fixing equipment as well as their scientific input on my research. I would like to thank both past and present Palmstrøm group members: Aaron, Alex, Aranya, Connor, Dan P., Dan R., Elliot, Hadass, Michael, Mihir, Paul, Shinichi, Shirshendu, Shouvik, Teun, Tony, Wilson, and Yu. I would especially like to thank Hadass and Mihir for teaching how to grow on various chambers and Elliot for training me on how to use the scanning tunneling microscopes.

I would also like to acknowledge the support from the molecular beam epitaxy lab, specifically the help from Kurt Olsson and John English for tackling certain vacuum related challenges. I would also like to thank Doug Rehn and Bobby Brown from the UCSB Physics machine shop for their help with machining parts, often at the last minute, so that we could implement our experiments.

Much of the work that was done during my time at UCSB would not have been made possible without our collaborators. I would like to thank Prof. Vlad Pribiag and Prof. Sergey Frolov for their valuable collaborations on superconductor/semiconductor systems. I would also like to thank Prof. Mike Pepper, Dr. Stuart Holmes, Dr. Yilmaz

Gul, and Irene Villar-Rodriguez for the help with fabricating and studying semiconductor quantum wells. Without them, many of the studies I performed were not possible.

Finally, I would like to thank my friends and my family for their support to me during my time as a PhD student.

Curriculum Vitæ

Jason Tianming Dong

Education

2024	Ph.D. in Materials (Expected), University of California, Santa Barbara.
2019	B.S. in Materials Science and Engineering, Northwestern University.

Awards

Young Scientist Award PCSI 48 (Redondo, CA 2023)

Selected publications

J. T. Dong, H.S. Inbar, M. Pendharkar, T.A.J. van Schijndel, E.C. Young, C.P. Dempsey, C.J. Palmstrøm *Electronic structure of InSb (001), (110), and (111)B surfaces.* J. Vac. Sci. Technol. B 41(3), 032808 (2023).

J.T. Dong, H.S. Inbar, C.P. Dempsey, A.N. Engel, C.J. Palmstrøm *Strain Solitons in an Epitaxially Strained van der Waals-like Material.* Nano Letters 41(3), 032808 (2024).

J.T. Dong, Y. Gul, A.N. Engel, T.A.J. van Schijndel, C.P. Dempsey, M. Pepper, C.J. Palmstrøm *Enhanced mobility of ternary InGaAs quantum wells through digital alloying.* Phys. Rev. Materials 8, 064601 (2024).

J.T. Dong, Y. Gul, I. Villar-Rodreguez, A.N. Engel, C.P. Dempsey, S. N. Holmes, M. Pepper, C.J. Palmstrøm *Spin-orbit coupling in digital alloyed InGaAs quantum wells.* In preparation.

Other publications

Z. Sun, C. Huang, J. Guo, **J.T. Dong**, R.F. Klie, L.J. Lauhon, D.N. Seidman *Strain-Energy Release in Bent Semiconductor Nanowires Occurring by Polygonization or Nanocrack Formation.* ACS Nano 13(3), 3730-3738 (2019).

J.N. Olding, A. Henning, **J.T. Dong**, Q. Zhou, M.J. Moody, P.J.M. Smeets, P. Darancet, E.A. Weiss, L.J. Lauhon *Charge Separation in Epitaxial SnS/MoS_2 Vertical Heterojunctions Grown by Low-Temperature Pulsed MOCVD* ACS Appl. Mater. Interfaces 11(43), 40543-40550 (2019).

A.H. Adekoya, U. Zhang, M. Peters, J. Male, Y. Chart, **J. Dong**, R. Franks, A. Furlong, B. Guo, M.T. Agne, G. Olson, G.J. Snyder *Iterative Design of a high zT thermoelectric material* Appl. Phys. Lett. 119(20) 202101 (2021).

S. Chatterjee, F. Crasto de Lima, J.A. Logan, Y. Fang, H. Inbar, A. Goswami, C. Dempsey, **J. Dong**, S. Khalid, T. Brown-Heft, Y.-H. Chang, T. Guo, D.J. Pennachio, N. Wilson, S. Chikara, A. Suslov, A.V. Fedorov, D. Read, J. Cano, A. Janotti, C.J. Palmstrøm *Identifying the fingerprints of topological states by tuning magnetoresistance*

in a semimetal: The case of topological half-Heusler $Pt_{1-x}Au_xLuSb$ Phys. Rev. Materials 5, 124207 (2021).

A. Goswami, A.P. McFadden, T. Zhao, H. Inbar, **J.T. Dong**, R. Zhao, C.R.H. McRae, R.W. Simmonds, C.J. Palmstrøm., D.P. Pappas *Towards merged-element transmons using silicon fins: The FinMET* Appl. Phys. Lett. 121, 064001 (2022).

G.V. Graziano, M. Gupta, M. Pendharkar, **J.T. Dong**, C.P. Dempsey, C. Palmstrøm, V.S. Pribiag *Selective control of conductance modes in multi-terminal Josephson junctions* Nat Commun 13, 5933 (2022).

H.S. Inbar, D.Q. Ho, S. Chatterjee, M. Pendharkar, A.N. Engel, **J. T. Dong**, S. Khalid, Y.H. Chang, T. Guo, A.V. Fedorov, D.Lu, M. Hashimoto, D. Read, A. Janotti, C.J. Palmstrøm *Epitaxial growth, magnetoresistance, and electronic band structure of GdSb magnetic semimetal films* Phys. Rev. Materials 6(12), L121201 (2022).

M. Gupta, G.V. Graziano, M. Pendharkar, **J.T. Dong**, C.P. Dempsey, C.J. Palmstrøm, V.S. Pribiag *Gate-tunable superconducting diode effect in a three-terminal Josephson device* Nat Commun 14, 3078 (2023).

P. Zhang, A. Zarassi, L. Jarjat, V. Van de Sande, M. Pendharkar, J.S. Lee, C.P. Dempsey, A. McFadden, S. D. Harrington, **J.T. Dong**, H. Wu, A.-H. Chen, M. Hocevar, C.J. Palmstrøm, S.M. Frolov *Large second-order Josephson effect in planar superconductor-semiconductor junctions* SciPost Physics 16(1), 30 (2024).

A.N. Engel, C.P. Dempsey, H.S. Inbar, **J.T. Dong**, S. Nishihaya, Y. Chang, A.V. Fedorov, M. Hashimoto, D. Lu, and C.J. Palmstrøm *Growth and characterization of α-Sn thin films on In- and Sb-rich reconstructions of InSb(001)* Phys. Rev. Materials 8, 044202 (2024).

Abstract

Molecular beam epitaxy of Group V-based materials with strong spin-orbit coupling

by

Jason Tianming Dong

This dissertation explores the growth and the electronic properties of materials with strong spin orbit coupling. Thin films of materials with strong spin-orbit coupling are of interest for their potential applications in spintronics and topological quantum computing. The thin films are grown with molecular beam epitaxy, and their structural and electronic properties are investigated with scanning tunneling microscopy and low temperature electron transport.

The first part of this dissertation will investigate the engineering of the mobility and spin-orbit coupling of high mobility InGaAs quantum wells by digital alloying. The mobility of InGaAs quantum wells is significantly limited by alloy disorder scattering. The effect of digital alloying on the mobility of InGaAs quantum wells is investigated, and digital alloying is found to enable record high electron mobilities for InGaAs quantum wells. This record high mobility is due to a reduction in the alloy disorder scattering. In addition, we demonstrate tuning of the spin-orbit coupling in the InGaAs quantum wells by up to 138 meVÅ by digital alloying. These results demonstrate the ability of digital alloying to engineer and enhance the properties of ternary quantum wells.

The Fermi-level pinning of various InSb surfaces is studied in the second part of this dissertation. The observed Fermi-level pinning is consistent with a charge neutrality point near the valance band maximum. Sb is found to shift the Fermi-level pinning position towards the conduction band minimum, with the (001) surface becoming under electron accumulation when sufficient Sb is on the surface. In contrast, the (111)B surface is

found to be strongly pinned, with only minor changes to the Fermi-level pinning upon Sb deposition. The surface treatment of InSb is found to be important for the Fermi-level pinning position, which can be exploited to tailor the properties of InSb based devices.

The last part of this dissertation focuses on the formation of strain solitons in epitaxial bismuth thin films. Synthesizing ultrathin epitaxial bismuth thin films on nonmetallic substrates has remained a significant challenge. Here, the growth of high quality epitaxial bismuth thin films on an InSb (111)B substrate is demonstrated. In these thin films, the epitaxial strain induced in the bismuth from the substrate is relaxed by strain soliton formation. Strain solitons are topological defects in van der Waals materials that can host novel electronic properties, but have only been observed in exfoliated flakes or freestanding layers on mechanically strained bulk crystals. The first scalable approach towards the generation of strain solitons by epitaxial growth is demonstrated. Evidence of edge state localization within the strain solitons is also observed.

Contents

Curriculum Vitae **vi**

Abstract **viii**

1 Introduction **1**
1.1 Confinement and heterostructures 1
1.2 Spin-orbit coupling 4
1.3 Applications of materials with strong spin-orbit coupling 10
1.4 Overview of this thesis 17

2 Methods **19**
2.1 Molecular beam epitaxy 19
2.2 Scanning tunneling microscopy and spectroscopy 23
2.3 Electron transport 29

3 Enhanced mobility by digital alloying in InGaAs quantum wells **39**
3.1 Improving mobilities in InGaAs quantum wells 39
3.2 Experiment 41
3.3 Heterostructure design 43
3.4 Quantum well band structure 46
3.5 Magnetotransport 48
3.6 Scattering mechanisms 55
3.7 Metal-insulator transition in the quantum wells 59
3.8 Summary 60
3.9 Acknowledgements 61

4 Spin-orbit coupling in digital alloyed quantum wells **62**
4.1 Increasing spin-orbit coupling in InGaAs quantum wells 62
4.2 Experiment 65
4.3 Magnetotransport of a graded InAs/InGaAs DA quantum well 66
4.4 Gate control of spin splitting in a quantum well 70
4.5 Influence of digital alloying on the spin-orbit coupling 73

4.6 Summary . . . 77
4.7 Acknowledgements . . . 78

5 Fermi-level pinning in InSb surfaces **79**
5.1 Fermi-level pinning in semiconductor surfaces . . . 79
5.2 Experiment . . . 81
5.3 (001) Surface . . . 84
5.4 (110) Surface . . . 87
5.5 (111)B Surface . . . 88
5.6 Summary . . . 92
5.7 Acknowledgements . . . 94

6 Strain solitions in an epitaxial bismuth thin film **95**
6.1 Epitaxial bismuth thin films . . . 95
6.2 Strain solitons . . . 98
6.3 Experiment . . . 99
6.4 Strain soliton formation in bismuth thin films . . . 99
6.5 Bending of strain solitons . . . 102
6.6 Strain mapping of strain solitons . . . 104
6.7 Scanning tunneling spectroscopy of strain solitons . . . 106
6.8 Summary . . . 107
6.9 Acknowledgements . . . 108

7 Summary and future work **109**
7.1 Summary . . . 109

A Mobility modeling **115**

B MATLAB code of mobility modeling **118**

C MATLAB code of quantum well band structure calculation **124**

D Ohmic contact to various III-V materials **147**

E Field emission cleaning of a STM tip **149**

Bibliography **151**

Chapter 1

Introduction

1.1 Confinement and heterostructures

Confinement effects in thin films of materials can cause the position of the electronic bands within the material shift and modifications to the density of states of the material. Confinement effects typically begin to be observed when the thickness of the material is on the order of a few to tens of nanometers. In semimetals, confinement can cause semimetallic to semiconductor transitions. In semiconductors, confinement typically causes the electronic gap to increase as the material becomes smaller. When different semiconductors are interfaced with each other, there is typically a nonzero conduction and valence band discontinuity, or band offset. The band offsets can be used to create an electrostatic potential for charge carrier confinement. The various band offsets of selected III-V materials are shown in Fig. 1.1. These band discontinuities can be used to both inhibit and promote charge carrier motion. By tuning the confinement of a material with and the material thickness and selection of the heterostructure, these heterostructures can be designed and engineered to create devices such as lasers, heterojunction bipolar transistors, and high electron mobility transistors [1].

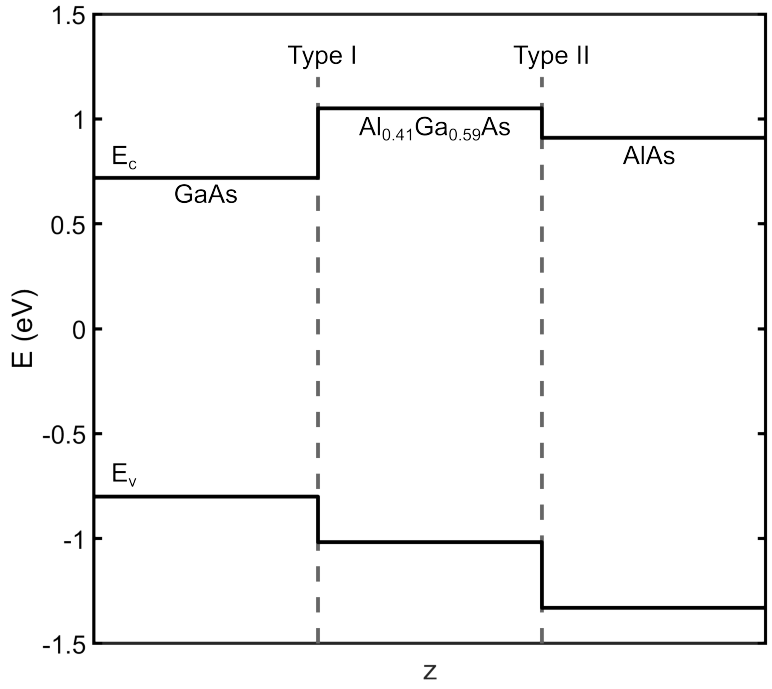


Figure 1.1: Band offset relative to the InSb valence band maximum for GaAs, $Al_{0.41}Ga_{0.59}As$, and AlAs. A type I interface is formed between GaAs/AlGaAs, and a type II interface is formed between AlGaAs/AlAs. Parameters used to generate the plot taken from [2].

When a material is inserted in between a material with either a positive conduction band offset (or a negative valance band offset), electrons (or holes) can become confined into the middle layer or channel. If the middle material is sufficiently thin, a quantum well (QW) can form. In this quantum well, charge carriers become confined into a two-dimensional plane, and the normally continuous bands can be quantized into discrete energy levels. In the case of a material of length (L) with infinite potential barriers surrounding it, the energy spacing of the energy levels is:

$$E_n = \frac{1}{m^*}(\frac{n\hbar\pi}{L})^2 \tag{1.1}$$

Where n is the index of the energy value and m^* is the effective mass of the band. In semiconductor heterostructures, the confinement due the band offset is finite, and there

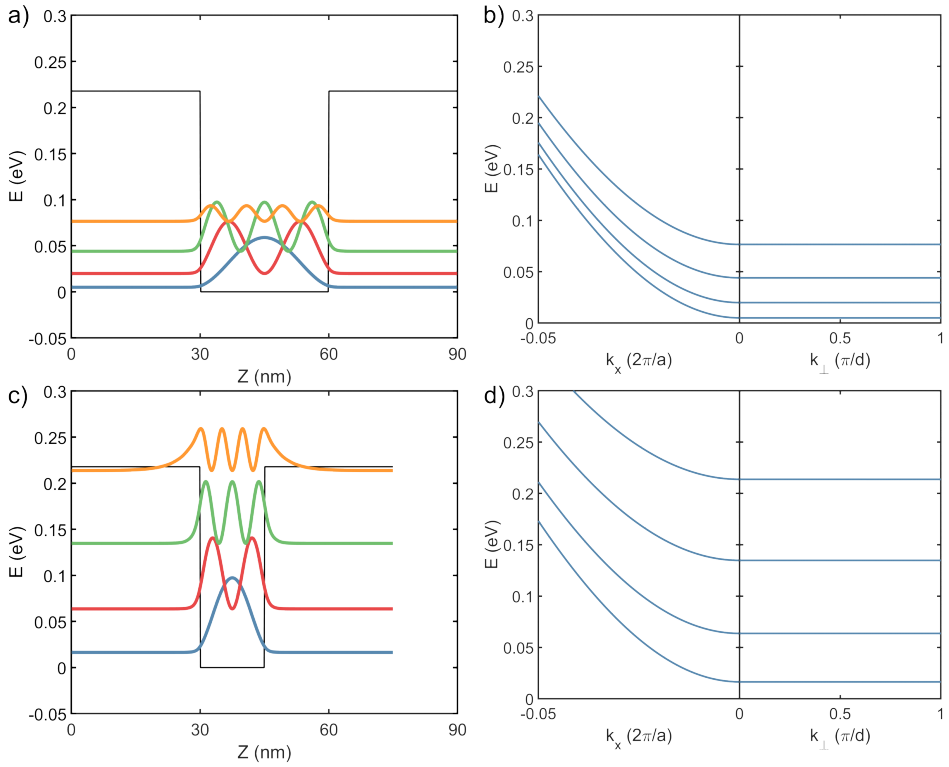


Figure 1.2: a) Heterostructure conduction band offsets and probability densities of a 30 nm GaAs QW with $Al_{0.24}GaAl_{0.76}As$ barriers. b) In plane and out of plane band dispersion of the quantum well. a) Heterostructure conduction band offsets and probability densities of a 15 nm GaAs QW with $Al_{0.24}GaAl_{0.76}As$ barriers. b) In plane and out of plane band dispersion of the quantum well.

is nonzero penetration of the wavefunction into the barrier layers.

The quantum wells can exhibit behavior characteristic of two-dimensional charge carriers. For example, AlGaAs has a straddling or type I band offset with GaAs (Fig. 1.1), the band offset between AlGaAs/GaAs causes both holes and electrons to be confined within the GaAs. The type I band offset the GaAs layer with AlGaAs can cause discrete quantum wells states to form in both the valence band and the conduction band. The probability densities of the conduction band subbands and the band structure of a 30 nm GaAs/AlGaAs QW, calculated with an 8 band $k \cdot p$ model described in [2], are shown in Fig. 1.2a & b. If the quantum well is two-dimensionally confined, there is no

out-of-plane dispersion of the subbands. The strength of the confinement and thus the energy separation of the discrete energy levels depends on the material's effective mass, thickness, and band offset. The strength of confinement and the energy level spacing can be increased by reducing the effective mass of the channel material, decreasing the quantum well thickness, or increasing the confining band offsets. The properties of a 15 nm GaAs QW are shown in Fig. 1.2c & d, where it can be observed the subband energy spacing significantly increases when the thickness of the GaAs layer decreases. The wavefunctions and energy levels of a quantum well can be modeled with approaches such as solving the Schröding-Poisson equation self-consistently [3] or with $k \cdot p$ perturbation theory [2]. In materials with a staggered or type II band offset, only one type of charge carrier becomes confined. For example, AlAs has a type II band offset with $Al_{1-x}Ga_xAs$ ($x > 0.20$), and AlGaAs can only be used to confined electrons and not holes in AlAs from the band offsets (Fig. 1.1). Beyond applications such as high electron mobility transistors, quantum wells can exhibit novel physical phenomenon such as the fraction quantum Hall effect and be used as a platform to study mesoscopic physics a [4].

1.2 Spin-orbit coupling

Spin-orbit coupling is a relativistic effect where a normally spin degenerate band can become spin split at zero external magnetic field (Fig. 1.3 a & b). The spin splitting arises due to electric fields within the material acting as an effective magnetic field and inducing the zero field spin splitting [5]. Spin-orbit coupling requires broken inversion symmetry in the material system to occur.

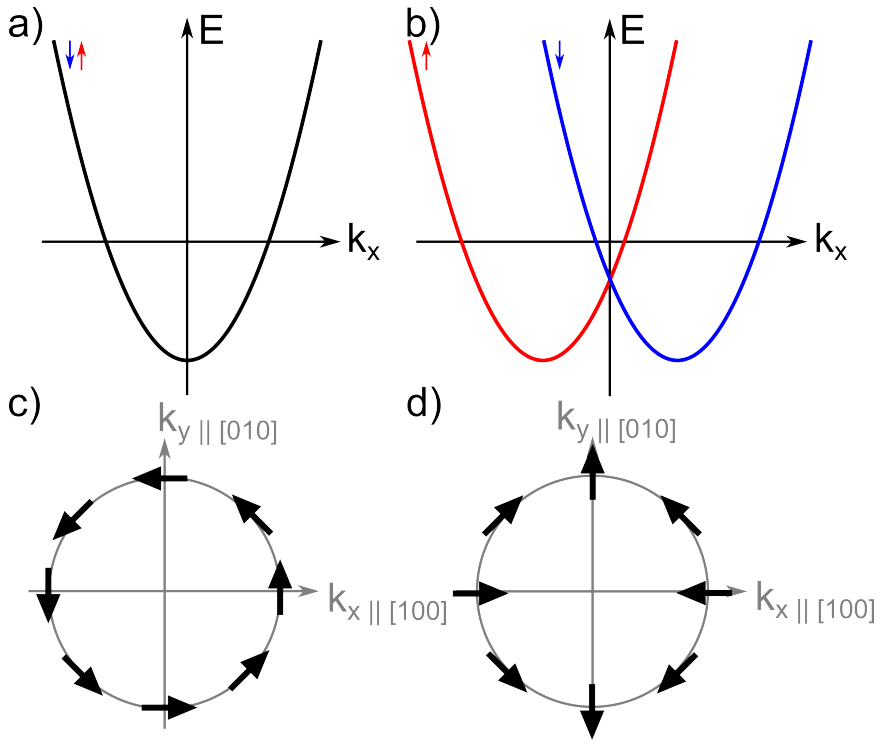


Figure 1.3: a) Schematic parabolic band dispersion of a spin degenerate band. b) Schematic spin splitting of a parabolic band due to spin-orbit coupling. c) Spin texture of a single spin non-degenerate Fermi-surface due to linear Rashba spin-orbit coupling in the [001] direction. d) Spin texture of a a single spin non-degenerate electron Fermi-surface of a III-V zincblende semiconductor due to Dresselhaus spin-orbit coupling. Note that the spin texture of the second spin non-degenerate band generated from spin-orbit coupling is opposite in direction of the schematics shown here.

1.2.1 Rashba and Dresselhaus spin-orbit coupling

In solid state materials, Rashba [6] and Dresselhaus [7] spin-orbit coupling are the primary mechanisms of spin-orbit coupling. Rashba spin-orbit coupling is due to inversion asymmetry in the heterostructure. Rashba spin-orbit coupling can be induced due to the band offset at a heterointerface, semiconductor band bending, or an external electric field induced with a gate electrode. Rashba spin-orbit coupling can be induced in bulk-like material systems with a gate electrode or surface band bending. Due to the dependence of the Rashba spin-orbit coupling on an electric field, the Rashba spin-orbit coupling can be gate tunable. The tunability of the Rashba spin-orbit coupling enables spin

manipulation in materials. The effect of the linear Rashba effect on a parabolic electron-like band dispersion with effective mass m^* can be defined with the following equation:

$$E_{\pm}(k) = \frac{\hbar^2 k^2}{2m^*} \pm \alpha|k| \tag{1.2}$$

Where α is the Rashba spin-orbit coupling parameter. The spin texture induced by the linear Rashba effect is isotropic always perpendicular to the electric field and the heterostructure and the momentum vector (Fig. 1.3c).

Dresselhaus spin-orbit coupling is due to broken inversion symmetry of the crystal structure. Noncentrosymmetric crystals such as the zincblende crystal structure of many of the III-V compounds posses Dresselhaus spin-orbit coupling. However, materials such as the Group IV semiconductors do not posses Dresselhaus spin-orbit coupling due to the diamond crystal structure being centrosymmetric. Since Dresselhaus spin-orbit coupling is dependent on the symmetry of the crystal structure, the spin texture induced by Dresselhaus spin-orbit coupling varies depending on the crystallographic direction. The spin texture due to Dresselhaus spin-orbit coupling on the [001] direction of a zincblende III-V is shown in Fig. 1.3d.

Deconvoluting the contributions to spin splitting between the Dresselhaus spin splitting and Rashba spin splitting is typically done from crystallographic orientation dependent measurements of the spin splitting [8–10]. The orientation dependence of Dresselhaus spin splitting enables measurements of the spin splitting where the Rashba and Dresselhaus spin splitting along the crystallographic directions where these two effects are competing with and enhancing each other. In the case of a electrons in III-V semiconductor with the inversion symmetry in the heterostructure is broken in the [001] direction, the direction where the Dresselhaus and Rashba effects are enhancing each other is the [110] direction, and the direction where the Dresselhaus and Rashba effects

are competing with each other is the $[1\bar{1}0]$ direction [11].

1.2.2 Spin-orbit coupling of electrons in zincblende III-V materials

In zincblende III-V materials, the Dresselhaus spin-orbit coupling typically provides a significantly smaller contribution to the total spin-orbit coupling than the Rashba spin-orbit coupling. From orientation dependent measurements of III-V quantum wells, the Dresselhaus spin splitting is typically 2-10 times smaller than the Rashba spin splitting [8–10, 12]. As a result, the Dresselhaus contribution is often ignored and only the Rashba spin-orbit coupling is considered in the spin-orbit coupling of the conduction band of III-V materials.

The Rashba parameter (α) can be separated in to two components, an electric field dependent component (α_{F_E}) and an interface dependent component (α_i):

$$\alpha = \alpha_{F_E} + \alpha_i \tag{1.3}$$

From the treatment by Winkler [13] using the $k \cdot p$ method, the α_{F_E} for electrons in zincblende III-V semiconductors can be treated as:

$$\alpha_{F_E} = \langle r_{41}^{6c6c} F_E \rangle \tag{1.4}$$

Where F_E is the electric field. r_{41}^{6c6c} is often approximated as being independent of the electric field. With this approximation, the equation becomes:

$$\alpha_{F_E} = r_{41}^{6c6c} \langle F_E \rangle \tag{1.5}$$

In bulk zincblende semiconductors, r_{41}^{6c6c} can be approximated as [13]:

$$r_{41}^{6c6c} = \frac{\hbar^2 E_p}{6m_0}\left(\frac{1}{E_g^2} - \frac{1}{(E_g + \Delta_{so})^2}\right)$$

Where E_g is the energy gap, Δ_{so} is the energy splitting of the split-off band from the valence band maximum, and E_p is the Kane energy. From this equation, it is expected that small band gap semiconductors have significantly larger Rashba parameters at the same electric field magnitudes, and the difference is $\propto E_g^{-2}$.

The $k \cdot p$ method can be used along with self consistent Schrödinger-Poisson solvers to calculate the α_{F_E} in a quantum well where the 1$^{\text{st}}$ subband is occupied [14,15]. Schäpers [15] introduced the following formalism:

$$\alpha_{F_E} = \frac{\hbar^2 E_p \hat{z}}{6m_0}\left(\langle\Psi(z)|\left(\frac{1}{(E - \Gamma_7(z) - \phi(z))^2} - \frac{1}{(E - \Gamma_8(z) - \phi(z))^2}\right)\phi'(z)|\Psi(z)\rangle\right. \quad (1.6)$$

Where $\hat{z}$ is the unit vector, $\Gamma_7(z)$ is the position dependence of the split-off band edge, $\Gamma_8(z)$ is the position dependence of the valance band edge, ϕ is the electrostatic potential, and $|\Psi|^2$ is the probability density. The energy E is often taken as the conduction band edge or the Fermi energy. The effect of the electrostatic potential on the α is relatively small and can often be neglected. If this contribution is neglected, the quantum-confined Stark effect is neglected, and E is treated as the conduction band edge (Γ_6), then an equivalent r_{41}^{6c6c} can be defined for a quantum well:

$$r_{41}^{6c6c} = \frac{\hbar^2 E_p}{6m_0}\left(\langle\Psi(z)|\left(\frac{1}{(\Gamma_6(z) - \Gamma_7(z))^2} - \frac{1}{(\Gamma_6(z) - \Gamma_8(z))^2}\right)|\Psi(z)\rangle\right. \quad (1.7)$$

In practice, r_{41}^{6c6c} tends to decrease with carrier density and thus E, and the decrease is $\propto E^{-2}$ [15]. For quantum wells with more than one subband being occupied, the contribution due to the coupling between the different subbands of the quantum well needs

to be accounted for [16]. In the absence of intersubband coupling, the α_{F_E} coefficient in quantum wells tends to be lower than that of the bulk, where the nonzero probability density in the larger band gap barrier material and the increase in the effective band gap due to confinement results in a lower Rashba coefficient.

The interface Rashba parameter, α_i, is the contribution to the Rashba parameter from heterointerfaces. Schäpers [15] introduced a formalism based on the $k \cdot p$ method for calculating the Rashba parameter of electrons in III-V heterostructures:

$$\alpha_i = \frac{\hbar^2 E_p \hat{z}}{6m_0} \sum_n \left(\frac{\Delta\Gamma_7}{2(E - \Gamma_7^+ - \phi(z_n))^2} + \frac{\Delta\Gamma_7}{2(E - \Gamma_7^- - \phi(z_n))^2} - \frac{\Delta\Gamma_8}{2(E - \Gamma_8^+ - \phi(z_n))^2} - \frac{\Delta\Gamma_8}{2(E - \Gamma_8^- - \phi(z_n))^2}\right)|\Psi(z_n)|^2 \quad (1.8)$$

Where n is the index for every interface in the heterostructure, $\Delta\Gamma_7$ is the split-off band offset of at the interface, $\Delta\Gamma_8$ is the valence band offset of at the interface, and $\pm$ is an index for the top and bottom material at the interface. For the interface Rashba parameter to be nonzero, the interface needs to be asymmetric or an asymmetric wavefunction is required. This interface term does have some dependence of the electric field within the heterostructure, through the effect of the electric field on the electrostatic potential and increased asymmetry of the wavefunction due to the quantum-confined Stark effect. Larger valance band offsets and smaller band gaps are required in order to increase the magnitude of the interface Rashba effect. From this treatment for calculating the Rashba spin-orbit coupling, small band gap materials such as InAs or InSb are expected to posses strong spin-orbit coupling.

1.3 Applications of materials with strong spin-orbit coupling

Thin films of materials with strong spin-orbit coupling have become of interest due to their potential applications for spintronics and topological quantum computing. As a result, significant efforts have been made towards improving the material quality and understanding the spin-orbit coupling within these materials.

1.3.1 Spintronics

Classical computing is primarily done with field effect transistors (FET), which can exist in two states: an on state and an off state. In a FET, the on state is when electrical current can pass through the FET, and the off state is when electrical current cannot pass through the FET. In contrast, the spin FET proposed by Datta and Das [17] operates on the spin of an electron instead of the resistance of the channel. Spin-FETs are potentially promising because they offer new functionalities such as nonvolatile information storage and reconfigurable output characteristics to the transistors [18]. Spin-orbit coupling is important to spin FETs. Spin polarized bands generated from spin-orbit coupling can be used as a spin injector and a spin filter. In addition, the tunability of spin-orbit coupling in solid state materials through the Rashba effect can be exploited to manipulate the spin in the spin FET.

In a spin FET, a spin current is injected into a semiconductor through a spin injector. The spin injector is often a ferromagnetic contact. This spin current exits the semiconductor through a spin filter, which is also typically a ferromagnetic contact. In the spin FET, the top gate induces Rashba spin-orbit coupling into the semiconductor and generates an effective magnetic field perpendicular to the current direction and the

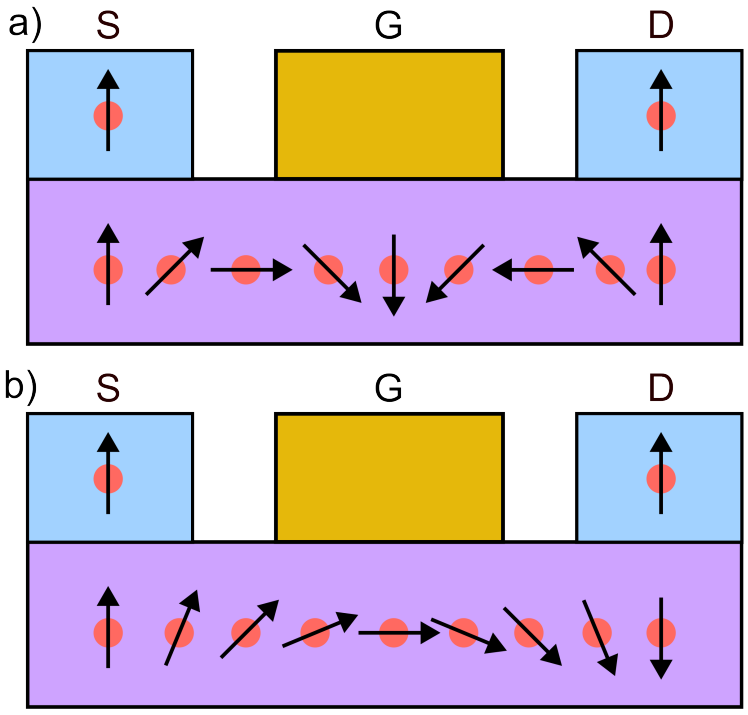


Figure 1.4: Schematic Datta and Das spin FET [17] in the a) on state b) and the off state.

direction of the electric field induced by the top gate. If the orientation of the spin injected into the semiconductor is perpendicular to the effective magnetic field generated by the Rashba effect, the spin will begin to precess around the Rashba field. By tuning the Rashba spin-orbit coupling and thus the strength of the effective magnetic field, the spin precession can be controlled with a gate electrode such that the spin precession results in either a spin that is parallel (on) or a spin that is perpendicular (off) to the spin filter as (Fig 1.4a & b). While ferromagnetic contacts are typically used as spin injectors and spin filters, it is possible to utilize spin-orbit coupling in the semiconductor as the spin injector and filter. All electrical spin injection, manipulation, and detection based on Rashba spin-orbit coupling has been demonstrated in an InGaAs quantum well [19]. The major limiting factors in spin FETs are the spin polarized electron injection and extraction efficiencies at the source and drain contacts as well as randomization of the

spin state in the channel due to scattering [18].

It is desirable that the semiconductor of a spin FET is a high mobility quantum well of a semiconductor with strong spin-orbit coupling such as InGaAs, InAs, or InSb. It is also desirable to have ballistic transport across the channel to prevent the randomization of the spin orientation due to scattering [20] and thereby increase the on/off ratio. As a consequence, high mobility materials are required to increase the mean free path of electrons within the material. In addition, the spin precession length becomes shorter as the spin-orbit coupling increases. Thus, materials with strong spin-orbit coupling are preferred to reduce the channel length to both enable better scaling and to reduce the mobility requirements for ballistic transport. Due to these considerations, it is still of interest to improve the mobilities of quantum wells of InGaAs, InAs, and InSb to fabricate better spin FETs.

1.3.2 Non-abelian anyons and topological quantum computing

In quantum mechanics, a particle exchange operator ($\hat{P}_{1,2}$) acting on a wavefunction comprised of two particles can be defined:

$$\hat{P}_{1,2}\psi(r_1, r_2) = \psi(r_2, r_1) = e^{i\theta}\psi(r_1, r_2) \tag{1.9}$$

The system should return to the original state if the particles are exchanged twice:

$$\hat{P}_{1,2}\hat{P}_{1,2}\psi(r_1, r_2) = \hat{P}_{1,2}\psi(r_2, r_1) = e^{2i\theta}\psi(r_1, r_2) = \psi(r_1, r_2) \tag{1.10}$$

For $e^{2i\theta}\psi(r_1, r_2) = \psi(r_1, r_2)$ to remain true, $e^{2i\theta} = 1$ and thus $\theta = n\pi$, where n is an integer. The θ can be separated into two cases: a case where n is an even integer, and a case where n is an odd integer. If the case of a single exchange event is considered

in the system, cases can be defined as the following: In the case where n is even and $\theta = 0, 2\pi, 4\pi, ...$

$$\hat{P}_{1,2}\psi(r_1, r_2) = \psi(r_2, r_1) = \psi(r_1, r_2) \tag{1.11}$$

In the case where n is odd and $\theta = 1\pi, 3\pi, ...$

$$\hat{P}_{1,2}\psi(r_1, r_2) = \psi(r_2, r_1) = -\psi(r_1, r_2) \tag{1.12}$$

The first case where n is even represents the exchange operation for a boson, and the second case where n is odd represents the exchange operation for a fermion. The exchange operator can be used to define a boson and a fermion. In addition, from the exchange operator, the wavefunctions of a boson are symmetric under exchange and can occupy the same state. In comparison, the wavefunctions of a fermion is antisymmetric under exchange and cannot occupy the same state. The property of fermions being antisymmetric under exchange gives rise to the Pauli exclusion principle. This treatment of the exchange operator is not exactly correct but is useful for obtaining an intuitive understanding of particle exchange.

In materials with less than three spatial dimensions, such as a two-dimensional electron gas or a nanowire, quasiparticles termed anyons can exist. Abelian anyons are quasiparticles that can have an arbitrary θ after exchange, and thus after the particles are exchanged twice, the system does not return to the same state and instead the wavefunctions acquires a complex phase of $e^{2i\theta}$. Non-abelian anyons are a type of anyons where the state of the system changes in addition to the phase change after particle exchange. This property of non-abelian anyons can be potentially exploited for topological quantum computing [21].

Quantum computing is a type of computing that allows for the bit, which are called

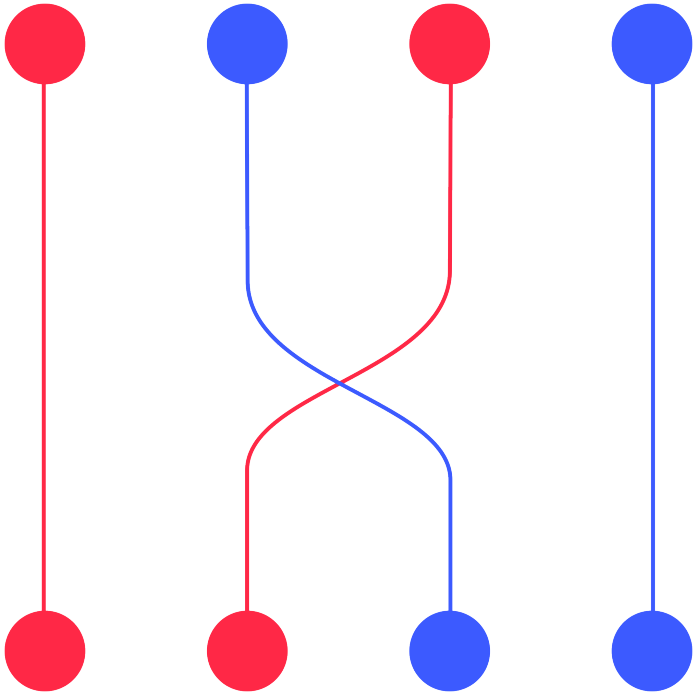


Figure 1.5: Schematic braiding of two pairs of Majorana zero modes, with the vertical axis being time. Majorana zero modes are created as pairs, and qubit operations can be performed by braiding or exchanging the Majorana zero modes. After the operations are performed, the Majorana zero modes can be fused and then readout of the state can be done after fusion.

qubits in quantum computers, to exist in a superposition of a 0 and 1 state instead of being either 0 or 1 [22, 23]. Quantum computing has potential applications in cryptography as well as simulation of quantum systems [24]. Currently, there have been demonstrations of quantum computing with 100s of qubits [25]. However, it has been predicted that several thousand qubits may be required for a useful quantum computer. Currently it is a significant scaling challenge to increase the number of qubit within a quantum computer [26], and a major scaling limitation is the error rates of qubits. Error rates within the qubit can be compensated for with error correction [27]. However, error correction increases the number of physical qubits required in the system. Because of these issues, large quantities of qubits are required for a useful quantum computing and

scaling the number remains a substantial challenge. Topological quantum computing is a potentially promising approach towards quantum computing with low error rates and rapid scaling that uses non-abelian anyons.

One approach towards topological quantum computing is with Majorana zero modes [28]. Majorana zero modes are quasiparticles that are their own anti-particle and form in pairs. Majorana zero modes are expected to be non-abelian anyons. In topological quantum computing with Majorana zero modes, the quantum information with the exchange operations of the Majorana zero modes. Logical operations can be performed by exchanging the Majorana zero modes (Fig 1.5). Due to the Majoran zero modes being non-abelian anyons, exchange operations change the quantum state of the system. The exchange operations are called braiding. After the operations are performed, the Majorana zero modes can be fused by bringing them together and annihilating the Majorana zero modes. Depending on the quantum state of the system, an electron or a hole will be generated. Readout of the operation is done by detecting the formation of the electron or the hole. The parity of the superconductor must be preserved in order for the detection of a single electron or hole being added to the system. Due to the quantum information being stored in the position of the quasiparticles, the system is only sensitive to noise that can cause the quasiparticles to exchange. If the quasiparticles are spatially separated from each other at sufficient distances, the system should be relatively insensitive to noise or perturbations due to an accidental exchange event from noise being extremely unlikely. This approach towards performing quantum computing offers with potentially low error rates and rapid scaling of qubits [21].

Majorana zero modes are predicted to be hosted within p-wave topological superconductors [28, 29]. This type of superconductivity requires an inverted band character. The inverted band character can be stabilized with strong spin-orbit coupling (Fig 1.6). Two potential approaches towards realizing a p-wave topological superconduc-

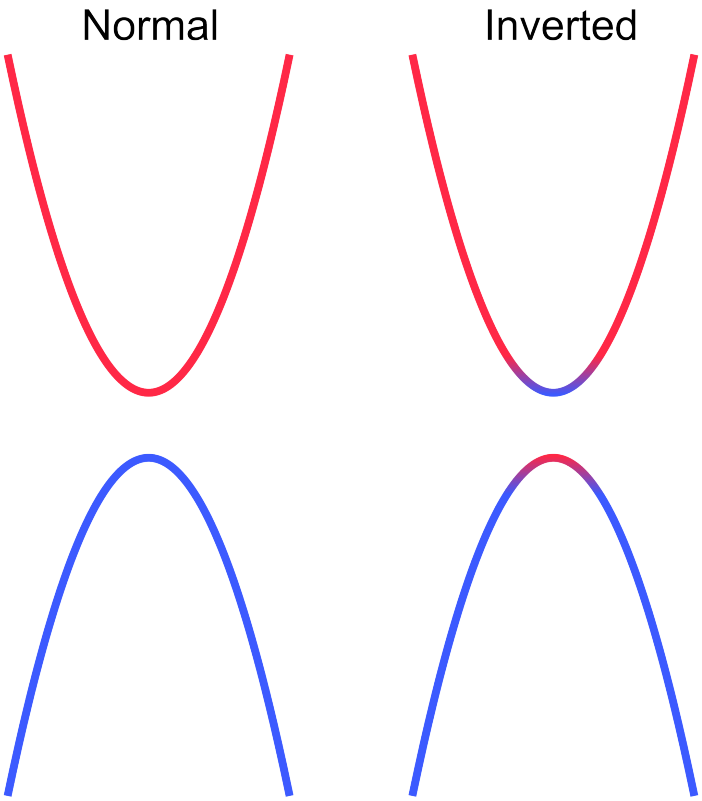


Figure 1.6: Schematic normal insulator and insulator with an inverted band ordering due to spin-orbit coupling.

tors are topological insulator/superconductor heterostructures [30, 31] or hybrid superconductor/semiconductor heterostructures [32, 33]. In both of these systems, a non-superconducting material is hybridized with a trivial s-wave superconductor to create a topological superconductor. In the case of the semiconductor/superconductor heterostructures, a magnetic field is also required to drive the system into the topologically nontrivial regime. To date, experimental evidence of Majorana zero modes has been lacking. Disorder within the material can create signatures similar to the expected properties of Majorana zero modes [34–36]. As a result, there is no general consensus that Majorana zero modes have been experimentally observed. From current experimental results, if Majorana zero modes do exist, they likely exist over a very narrow parameter space and

scaling up these devices would be a significant challenge due to the extreme fine tuning required to operate the device in the topological superconducting regime [37]. Theoretical work has shown that reducing disorder by improving mobilities and increasing the spin-orbit coupling of materials is expected to increase the topological superconducting gap and increasing the parameter space in which the Majorana zero modes can be observed [37]. If the topological gap can be significantly increased, it may be easier to find conclusive evidence of Majorana zero modes and therefore establish topological quantum computing with Majorana zero modes as a viable approach towards quantum computing. As a consequence, improving the mobility and increasing the spin-orbit coupling of the semiconductors and topological insulators is of interest.

1.4 Overview of this thesis

This dissertations explores the study of the growth and the electronic properties of epitaxial group V based thin films. Three different material systems will be explored: high mobility InGaAs quantum wells, InSb, and epitaxial bismuth thin films. In chapter 2, an overview of the methods used in this dissertation will be discussed. Principles of molecular beam epitaxy, scanning tunneling microscopy, and magnetotransport will be discussed. Chapter 3 explores the improvement of the mobility of InGaAs quantum wells by digital alloying. The works focusing on impact of digital alloy has on the charge carrier scattering in a high mobility quantum well, and how the heterostructures can be designed to improve the mobility to record breaking numbers. Chapter 4 explores the impact of digital alloying on the spin-orbit coupling of the InGaAs quantum wells, and how digital alloying can be used to both increase and decrease the spin-orbit coupling of the InGaAs quantum wells. Chapter 5 investigates the Fermi-level pinning of InSb surfaces with scanning tunneling microscopy, and how the pinning position can be modified depending

on the surface treatment. In chapter 6, the growth and relaxation of heteroepitaxial bismuth thin films is explored. Finally, the conclusions of this work and the potential future work are give in chapter 7.

Chapter 2

Methods

2.1 Molecular beam epitaxy

Molecular beam epitaxy (MBE) is a physical vapor deposition technique performed in ultra-high vacuum (Fig 2.1). In a MBE chamber, elemental source material is thermally heated until the material provides a sufficiently high vapor pressure of the element for deposition. In ultra-high vacuum, the mean free path of the elements in the vapor form is longer than the source to sample distance. As a result, the vapor travels as non-interacting beams and relies on line of sight to impinge upon the substrate. The beams can be either atomic beams or molecular beams, depending on if the element evaporates as a molecule or an atom. Upon impinging on the substrate, the element can interact with the substrate and any other elements present on the substrate surface to generate an epitaxial thin film. Typical growth rates of MBE grown thin film range from 10s of nm to 2 μm per hour.

In MBE, the main control variables are the fluxes of the source material and the temperature of the substrate. Both the flux of atoms on the surface and the substrate temperature influence the kinetics of the atoms and the surface chemistry, which in turn

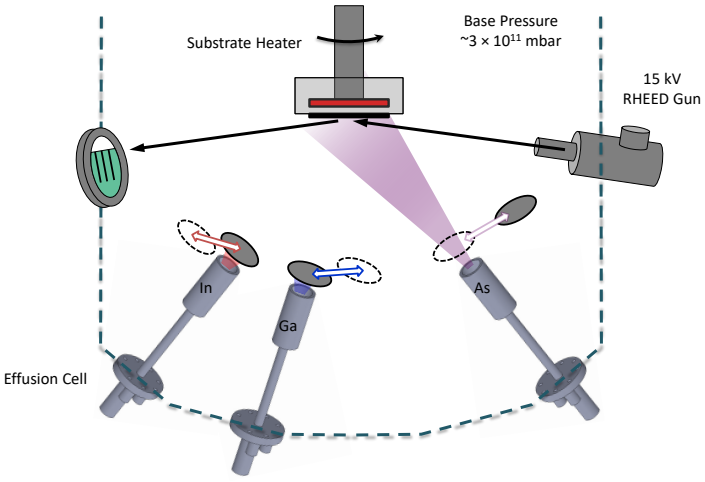


Figure 2.1: Schematic of a MBE. Beams of source material from thermally heating the material travel towards the substrate, which is heated. The beams can be prevented from impinging upon the samples with shutters, which block line of sight of the beams onto the substrate surface.

influences the growth mode, the crystalline phase, and the crystalline quality of the epitaxial thin film. MBE grown thin films using high purity source material can have extremely low unintentional background doping due to the ultra-high vacuum environment and high source material purity, and also have atomically abrupt interfaces within the thin film. These properties of MBE grown thin films have enabled record breaking mobilities of two-dimensional electron gases [38].

In a MBE chamber, there is often *in-situ* monitoring of the sample surface with reflection high energy electron diffraction (RHEED). RHEED allows for a qualitative determination of the surface roughness and crystalline quality. RHEED also allows for the determination of the growth rate by monitoring the fluctuations of RHEED intensity due to the interference of the RHEED pattern during layer-by-layer growth. In this dissertation, the atomic fluxes of the group III cells were determined using RHEED

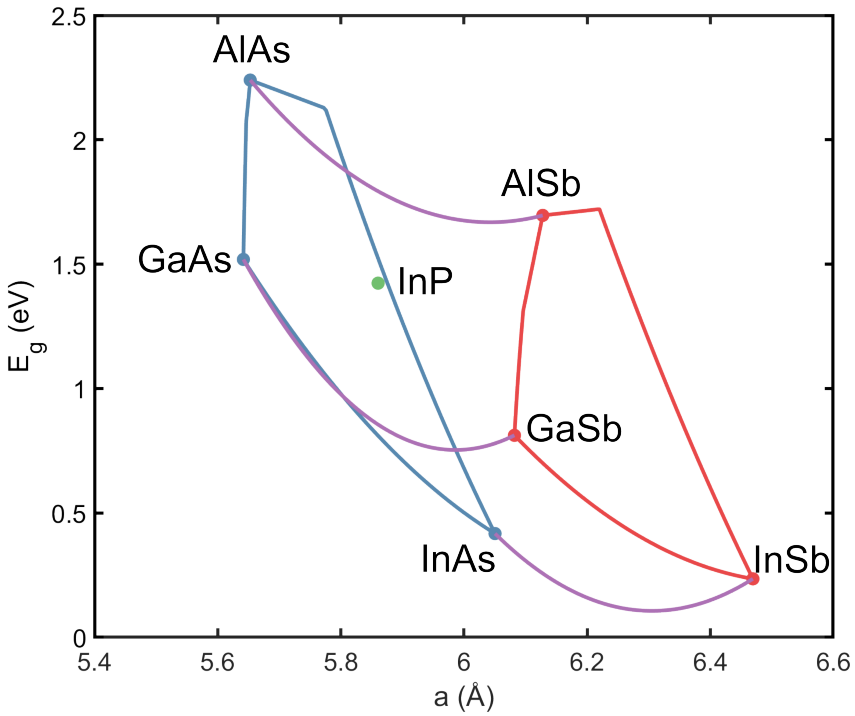


Figure 2.2: Band gap and lattice constant of selected III-V binaries and ternaries at T = 0 K. Parameters used to generate the plot are taken from [2].

oscillations.

MBE growth can be done as homomorphic, pseudomorphic, or metamoprhic [39, 40]. In homomorphic growth, the same material is epitaxially grown on itself. Homomorphic growth is important for creating devices such as PN diodes where the carrier density varies in the growth direction. Pseudomorphic growth is the growth of coherently strained materials on a substrate that is comprised of a different material. In order for the growth to be considered pseudomorphic, the material must remain strained and cannot relax. Because of this constraint, the total thickness able to be grown by pseudomorphic growth is limited by the lattice mismatch between the epilayer and the substrate, and thereby can limit the heterostructure design and possible material combinations. In the III-V materials, the variation of properties such as the band gap (Fig 2.2) is often accompanied by significant changes in the lattice constant of the material. If the growth is restricted

to being homomorphic or pseudomorphic, the thicknesses and the properties of the III-V thin film can become heavily constrained. It is therefore desirable for the growth of relaxed materials on a lattice mismatched substrate, also known as metamorphic growth.

In comparison to homomorphic or pseudomorphic growth, metamorphic growth often requires thicker epilayers to grow a high quality thin film [39]. Since metamorphic growth is by definition relaxed, dislocation formation necessarily occurs. Misfit dislocations form to allow the lattice constant of the epilayer to relax. The relaxation by dislocation formation can cause two detrimental effects in the epitaxial thin films: increased roughness and threading dislocations formation in the thin film. Increased roughness can lower charge carrier mobilities due to increased interfacial roughness scattering of charge carriers. During the relaxation process, a given misfit dislocation typically has a finite line length and terminates with two threading dislocations. The threading dislocations then propagate throughout the rest of the epilayer to the surface of the film. The density of threading dislocations formed in a thin film can be reduced by increasing the misfit dislocation length length, which enables fewer threading dislocations to be formed during the relaxation process. Threading dislocations can lower the performance of the device by serving as leakage paths for charge carriers or sites of non-radiative recombination. These detrimental effects of relaxation can be mitigated by growing the metamorphic thin film thicker. Thicker growth typically results in smoother thin films [39], and thicker films allow the threading dislocations to terminate at the sides of the thin film instead of the surface and enables threading dislocation annihilation through the increased likelihood of dislocation-dislocation interaction in thicker films, thereby reducing the threading dislocation density. In addition to thicker growth, the quality of the metamorphic thin film can be improved by grading the lattice constant from the substrate to the desired lattice constant and by adding dislocation filtering layers. Slow grading of the lattice constant is believed to help prevent the formation of threading dislocations [41] and dislocation

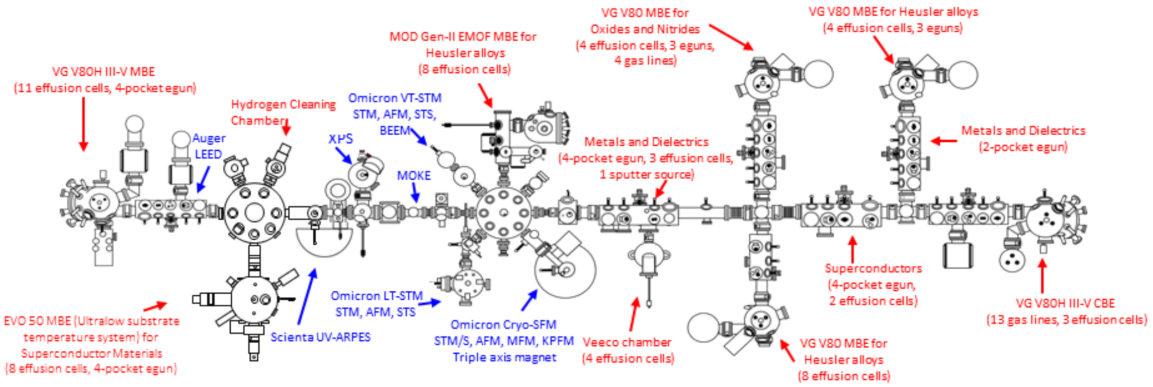


Figure 2.3: Schematic of the Palmstrøm lab group interconnected ultahigh vacuum growth and characterization facility.

filters such as a strained superlattice, which generate strain fields that can bend threading dislocations and prevent them from propagating towards the surface and penetrating the active region of the device [42, 43].

The MBE growth done in this dissertation was performed with the Palmstrøm lab group interconnected ultahigh vacuum growth and characterization facility. A schematic of the interconnected facility is shown in Fig. 2.3. In this dissertation, III-V MBE growth was performed in the VG V80H III-V MBE system. Oxide removal with atomic hydrogen cleaning was done in a bi-directional transfer chamber. The growth of bismuth thin films was performed in the modfied Gen-II MBE system. Due to the interconnected nature of this system, *in vacuo* scanning tunneling microscopy was able to be performed by transferring a sample into the scanning tunneling microscope while maintaining a pristine surface.

2.2 Scanning tunneling microscopy and spectroscopy

Scanning tunneling microscopy (STM) is a scanning probe microscopy technique invented by Binning and Rohrer [44], for which they were awarded the 1981 Nobel prize in

physics. Scanning tunneling microscopy is based on vacuum tunneling between a sharp tip and a sample. The tunneling current between the tip and the sample is sensitive to the local density of states. The tip can be raster scanned across the surface of a sample to obtain information about the topography of the surface. Scanning tunneling microscopy can directly probe the local density of states of the surface of materials at the atomic scale.

2.2.1 Vacuum tunneling

Tersoff and Hamann developed a theory of quantum tunneling in a STM based on a time dependent perturbation theory [45]. Their theory was developed on the tunneling formalism from Bardeen. The tip and the sample are treated as two independent subsystems, and a tunneling current occurs through the transition of a charge carrier between the tip and the sample. The tunneling current for between tip and sample states ψ_μ^t and ψ_ν^s with energies E_μ^t and E_ν^s under an applied bias of V:

$$I = \frac{4\pi e}{\hbar} \sum_{\mu,\nu} f(E_\mu^t)(1 - f(E_\nu^s))|M_{\mu\nu}|^2 \delta(E_\mu^t - E_\nu^s) \tag{2.1}$$

The Fermi-Dirac distributions f in the equation imply that tunneling occurs from an occupied state into an unoccupied state. The delta function restricts the tunneling condition to elastic tunneling. $M_{\mu\nu}$ is the matrix element. Assuming the tip and sample states are on a continuum, the summation can be converted into an integral over the density of tip and sample states:

$$I = \frac{4\pi e}{\hbar} \int dE \rho_s(E + eV)\rho_t(E) f(E + eV)(1 - f(E))|M_{\mu\nu}|^2 \tag{2.2}$$

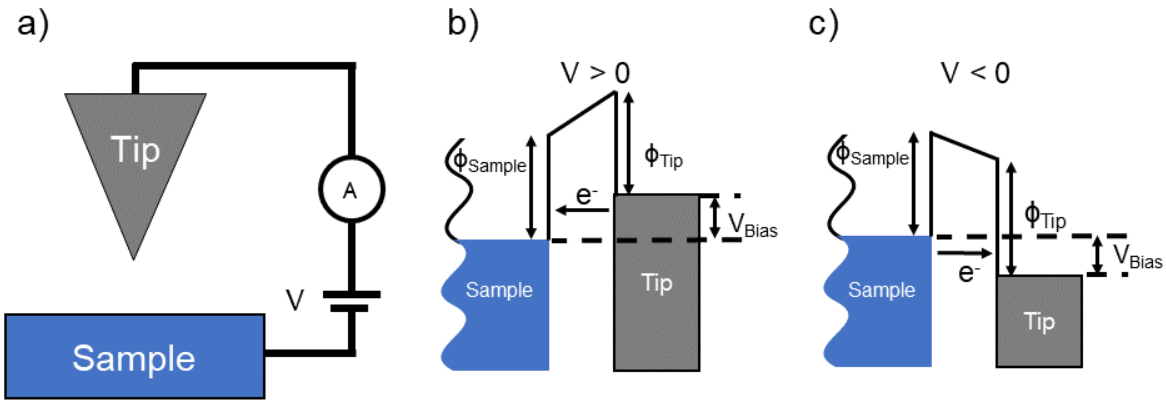


Figure 2.4: a) Schematic STM experiment. Schematic tunneling between the tip and sample at positive b) and negative c) biases.

Tersoff and Hamann then modeled the tip as a spherical potential well. They assumed that the tip has a spherically symmetric wave function. With these approximations and assumptions, the matrix element is energy independent. The tunneling current equation then becomes:

$$I = \frac{4\pi e}{\hbar}|M_{\mu\nu}|^2\rho_t \int dE\rho_s(E+eV)\rho_t(E)f(E+eV)(1-f(E)) \tag{2.3}$$

Since tunneling requires the transport of current between the tip and sample, a strict requirement for STM measurements is the samples must be conductive.

2.2.2 Strain extraction from a STM image

In an STM image, finer features on the surface such as the atoms or the surface reconstruction are often visible. If these features are periodic, then the strain on the surface can be directly measured with STM by measuring the displacements of the atoms or the lattice points of the surface reconstruction from the perfect lattice. The geometric phase analysis [46] and the Lawler-Fujita algorithm [47] can both be utilized to extract the displacement of the lattice points from a perfect lattice. The geometric phase

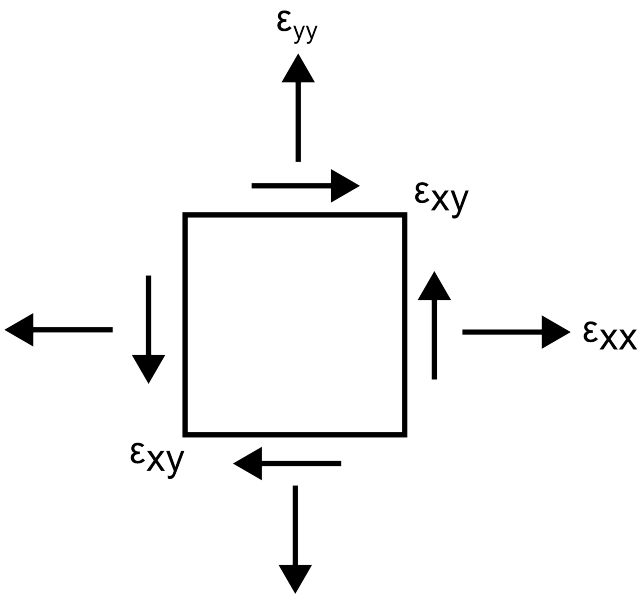


Figure 2.5: Schematic two-dimensional strain state.

analysis is typically used to extract strain of high resolution transmission electron microscopy images, while the Lawler-Fujita algorithm has been typically used to extract strain from atomic resolution STM images. Hamidian *et al.* describe the implementation of the Lawler-Fujita algorithm in detail [48]. Both algorithms utilize inverse fast Fourier transforms of two reciprocal lattice points to extract atomic displacements and are mathematically similar to each other. With these algorithms, the spatially varying in-plane atomic displacements ($u_x(r)$, $u_y(r)$) can be extracted. The partial derivatives of the spatially varying displacements can be taken, obtaining $\frac{\partial u_x(r)}{\partial x}$, $\frac{\partial u_x(r)}{\partial y}$, $\frac{\partial u_y(r)}{\partial x}$, and $\frac{\partial u_y(r)}{\partial y}$. The in-plane strain tensor (Fig. 2.5) can now be determined:

$$\epsilon(r) = \begin{bmatrix} \frac{\partial u_x(r)}{\partial x} & \frac{\partial u_x(r)}{\partial y} + \frac{\partial u_y(r)}{\partial x} \\ \frac{\partial u_y(r)}{\partial x} + \frac{\partial u_x(r)}{\partial y} & \frac{\partial u_y(r)}{\partial y} \end{bmatrix} = \begin{bmatrix} \epsilon_{xx}(r) & \epsilon_{xy}(r) \\ \epsilon_{yx}(r) & \epsilon_{yy}(r) \end{bmatrix} \tag{2.4}$$

Additionally, the rotation tensor can also be determined:

$$\omega(r) = \begin{bmatrix} 0 & \frac{\partial u_x(r)}{\partial y} - \frac{\partial u_y(r)}{\partial x} \\ \frac{\partial u_y(r)}{\partial x} - \frac{\partial u_x(r)}{\partial y} & 0 \end{bmatrix} = \begin{bmatrix} 0 & \omega_{xy}(r) \\ \omega_{yx}(r) & 0 \end{bmatrix} \tag{2.5}$$

The maps of the $\omega(r)$ and $\epsilon(r)$ often have artifacts at the edges of the image due to the inverse Fourier transform process assuming translational symmetry of the image. As a result, the data at the edges is typically discarded for the analysis and generation of the $\omega(r)$ and $\epsilon(r)$ images.

High resolution STM images can often take up to an hour to acquire. Due to this long acquisition process, artifacts in the measured atomic displacement can occur due to effects such as thermal drift of the STM tip and piezo creep, resulting in a slow spatially varying background of atomic displacements. Low temperature measurement can reduce but not eliminate the effect of these artifacts in the measurement. To remove the effect of these artifacts, a low order polynomial subtraction is typically applied to either the displacement vector or the partial derivatives of the displacement vector [49–51]. With this background subtraction, the local strain state of the surface can be determined with STM.

2.2.3 Scanning tunneling spectroscopy

The local density of states of a sample can be directly measured using scanning tunneling spectroscopy (STS). In an STS measurement, the current between the tip and sample at different voltages is typically measured with constant tip-sample separation. Differentiating the tunneling current from the equations above and assuming the tip

density of states can be approximated as energy independent, the dI/dV becomes:

$$\frac{dI}{dV} \propto \rho_t \frac{d}{dV} \int dE \rho_s(E + eV) f(E + eV)(1 - f(E)) \tag{2.6}$$

From the equation above the dI/dV is directly proportional to the local sample density of states that is broadened by Fermi-Dirac distributions.

While the dI/dV can be obtained by numerically differentiating the tunneling current, the dI/dV is typically obtained with a lock-in amplifier to improve the signal to noise. A small sinusoidal dV, with amplitude V_m, is applied to the system, and corresponding dI response is measured. The energy resolution (ΔE) of STS is given by the following equation [52]:

$$\Delta E \simeq \sqrt{(3.3kT)^2 + (2.5V_m)^2} \tag{2.7}$$

The energy resolution is limited by the lock-in amplifier applied V_m and thermal broadening. STS performed at low temperatures can have sub meV energy resolution.

2.2.4 Tip induced band bending

In performing STS of semiconducting samples, the voltage drop between the tip and sample is not completely in the vacuum region between the tip and sample, this effect is called tip induced band bending. There is some voltage drop in the semiconductor. The voltage drop across the semiconductor bends the bands; the extent of tip induced band bending depends on the material in question, the carrier concentration of the material, and the applied voltage. Higher carrier densities within the semiconductor can reduce the magnitude of the tip induced band bending. Tip induced band bending can causes shifts in the location of the conduction and valence band edges. It is the reason why band gaps measured by STS are often larger than the true band gap of the sample. Quantitative

models exist to account for tip induced band bending and recover the true density of states of the sample [53, 54]. These models are effective mass models, and require the knowledge of the band structure, carrier concentration, the effective masses, the dielectric constant, the tip sample separation, the tip sample contact potential difference, and the tip radius. The last three parameters are not parameters that will be known *a priori* and instead are treated as fitting parameters that are adjusted to provide a better fit to experimental data. The major challenge with utilizing these models is that the sample's band structure and electronic properties have to be well understood in order to accurately model the effect of tip induced band bending and recover the true local density of states.

2.3 Electron transport

2.3.1 Single carrier transport and the Hall effect

With the Drude model, the mobility of a charge carrier can be defined as:

$$\mu = \frac{e\tau}{m^*} \tag{2.8}$$

Where μ is the charge carrier mobility, e is the elementary charge, m^* is the effective mass, and τ is the scattering time. Charged defects such as impurities and dislocations can lead to charge carrier scattering and reduce the scattering time. Higher quality materials tend to have higher charge carrier mobilities. With the mobility now being defined, the conductivity of the material can be defined with the carrier density (n):

$$\sigma = ne\mu = \frac{ne^2\tau}{m^*} \tag{2.9}$$

The resistivity of the sample can be defined as $\rho = 1/\sigma$. In most experiments, the

resistance of the sample can be measured by applying a current (I) through the sample and measure the voltage (V) drop across the sample. With these two quantities, the resistance can be defined using Ohm's law:

$$R = \frac{V}{I} \tag{2.10}$$

Often the 4 point resistance measurements are used to measure resistance. In a 4 point resistance measurement, current is sourced through two electrodes, and the voltage drop across the sample is measured with the other two electrodes. The advantage of the 4 point resistance method is that the contact resistance is not measured in this set up, and only the sample resistance is measured.

ρ is an intensive quantity that relates to the resistance of a sample. From resistance measurements, the ρ can be determined. van der Pauw determined a method of measuring the resistivity from four point resistance measurements on the edges of an arbitrarily shaped sample [55]. Measurements with the van der Pauw geometry are often convenient because measurement can be performed without fabrication by soldering on contacts to the edges of the sample (Fig 2.6 a). Procedures for obtaining Ohmic contacts for van der Pauw measurements on various III-V semiconductors are described in Appendix D. For a perfect square sample that is isotropic, the sheet resistance (R_S) is:

$$R_S = \frac{\pi R}{ln(2)} \tag{2.11}$$

For arbitrary shaped samples, a horizontal (R_H) and vertical (R_V) resistance can be defined by averaging the resistance along the two directions. The sheet resistance then

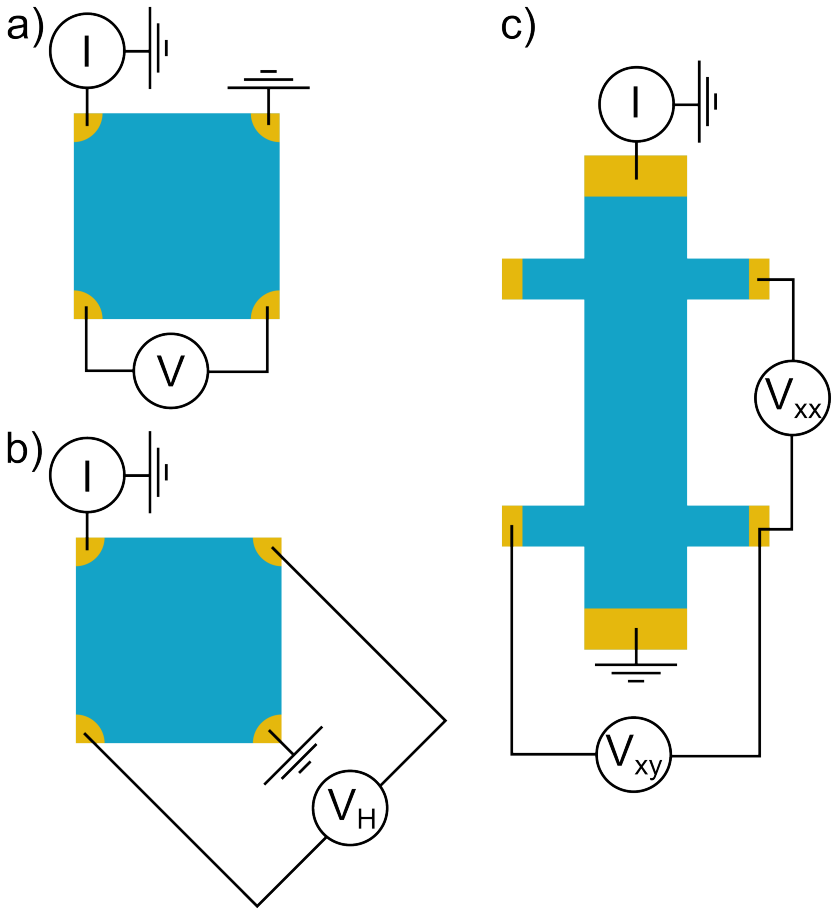


Figure 2.6: Schematic measurement in the van der Pauw geometry for a sheet resistance measurement a) and b) Hall measurement. c) Schematic measurement of a Hall bar.

be determined by solving the following equation:

$$e^{\frac{-\pi R_H}{R_S}} + e^{\frac{-\pi R_V}{R_S}} = 1 \tag{2.12}$$

The sheet resistance can also be measured with a Hall bar (Fig 2.6 c), where the R_S can be given by the with of the Hall bar (w) and the spacing between the arms of the

Hall bar (l) from the resistance of the Hall bar:

$$R_S = \frac{Rw}{l} \tag{2.13}$$

The resistivity can now be determined with the following equation:

$$\rho = R_S t \tag{2.14}$$

Where t is the thickness of the sample. While the above treatment has shown that the resistivity and the conductivity of a material can be measured with resistance measurement, it is often of interest to quantify the charge carrier mobility. To do so, the carrier density of the material system has to be measured. The carrier density in a material system can be measured with the Hall effect.

A magnetic field (B) pointing out of plane of a sample and perpendicular to the current generates a Lorentz force upon the current. This Lorentz force causes the current to deflect, and as a result a voltage transverse to the direction of the current travel can be measured. This voltage is the Hall voltage (V_H). In a material system with a single carrier, the Hall voltage is dependent on the current passing through the sample, and the sheet carrier density of the sample (n_s):

$$V_H = \frac{IB}{en_s} \tag{2.15}$$

This equation can be rearranged to the following:

$$n_s = \frac{IB}{eV_H} = \frac{B}{eR_H} \tag{2.16}$$

The equation is also defined in terms of the Hall resistance (R_H). The sign of the Hall

voltage can be used to determine if the carrier type is electron or holes. Larger R_H is indicative of lower carrier densities and the R_H should be linear with B. If multiple carriers are present within the material system, a nonlinear R_H dependence on B can be observed. The Hall resistance can be conveniently measured on a Hall bar or in the van der Pauw geometry under an applied magnetic field. The n_s is the two-dimensional carrier density, and can be converted to the three dimensional carrier density with the following:

$$n = \frac{n_s}{t} \tag{2.17}$$

With the resistivity and the carrier density being known, the mobility of the sample can be determined with the following equation:

$$\mu = \frac{1}{en_s R_S} \tag{2.18}$$

If the effective mass of the sample is known, the transport lifetime (τ_t) can now be determined from the mobility measured using the Hall effect and the zero field resistivity with the following equation:

$$\tau_t = \frac{\mu m^*}{e} \tag{2.19}$$

Calculating the lifetime can be useful for comparison of scattering of charge carriers between material systems that posses different effective masses.

The above treatment is for the case of the sample being isotropic. If there is anisotropy in the system, due to either the material or the measurement configuration then the conductivity and resistivity can be expressed as a tensor. The conductivity and resistivity can be converted to each other with the following equations:

$$\sigma_{xx} = \frac{\rho_{xx}}{\rho_{xx}^2 + \rho_{xy}^2} \tag{2.20}$$

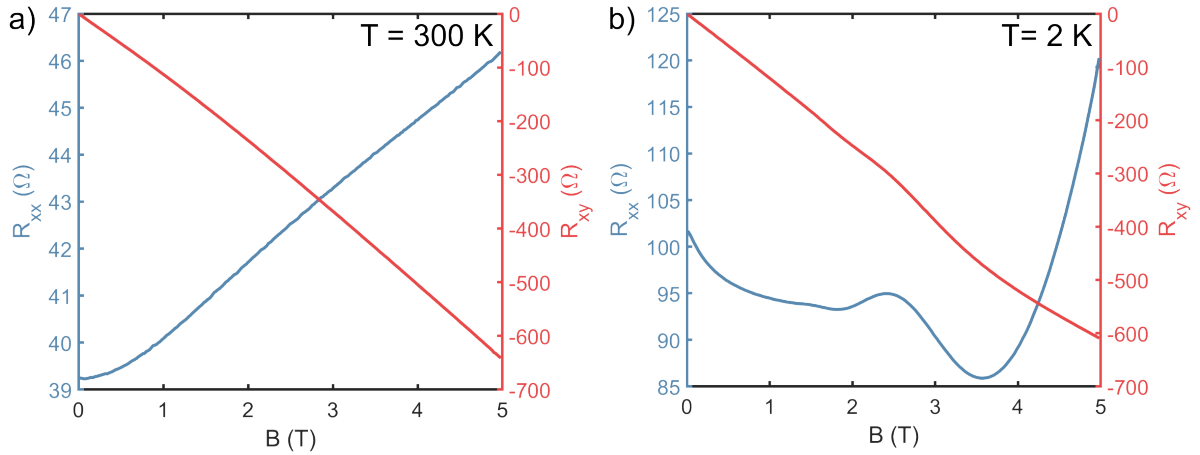


Figure 2.7: a) Magnetotransport of a 1 μm thick Si doped GaAs layer at 300 K. b) Magnetotransport of the same sample at 2 K. Measurements done in the van der Pauw geometry.

$$\sigma_{xy} = \frac{\rho_{xy}}{\rho_{xx}^2 + \rho_{xy}^2} \tag{2.21}$$

The isotropic ρ is now has now a directional dependence and becomes ρ_{xx}, ρ_{yy}, and ρ_{zz}. The ρ_{xy} can be defined from the Hall measurements:

$$\rho_{xy} = R_{xy}t \tag{2.22}$$

For isotropic samples in the van der Pauw or Hall bar measurement geometries, $\rho_{xy} = 0$ at zero magnetic field. In two-dimensional systems, $\rho_{xy} = R_{xy}$ and $\rho_{xx} = R_S$. Magnetotransport in the van der Pauw geometry of a 1 μm thick Si doped GaAs epilayer is shown in Fig. 2.7a. The Hall resistance is linear, except for some slight non-linear behavior at $B = 0$ T. This slight non-linearity is likely due to contact asymmetry from imperfect soldered contacts on the sample.

2.3.2 Magnetotransport at high magnetic fields

At low temperatures and high magnetic fields, oscillations in the magnetotransport can be observed in materials. In the same 1 μm thick Si doped GaAs epilayer, these oscillations can be observed at T = 2 K (Fig. 2.7b). These oscillations in resistance are Shubnikov-de Haas (SdH) oscillations. The oscillations are periodic in 1/B. The oscillations are observed at low temperatures in high mobility samples. When an uniform magnetic field is applied to a sample, the electrons within the sample form cyclotron orbits around the magnetic field. The energy of the orbits is quantized to Landau levels, and peaks and troughs occur in the density of states of the sample due to the Landau level quantization. As the magnetic field applied on the sample changes, the Landau level quantization changes and the peaks and troughs of the density of states due to the Landau levels can pass through the Fermi-level. As the Landau levels pass the Fermi-level, oscillations in the conductance and thus the resistance occur as the magnetic field is swept. The Landau levels are broadened due to disorder and thermal broadening, which is why samples with high mobility and low measurement temperatures are required to observe SdH oscillations. The landau level are spaced in energy by:

$$\hbar\omega_c = \frac{\hbar eB}{m^*} \tag{2.23}$$

The frequency of the oscillation can be used to extract the Fermi-surface of the sample that is generating the SdH oscillations. Since the oscillations are period in 1/B, the frequency (f) of the oscillations can be expressed in units of Tesla. The carrier density for a spin degenerate Fermi-surface without any valley degeneracy is:

$$n = \frac{2ef}{h} \tag{2.24}$$

For a spin split Fermi-surface, the carrier density can be expressed as:

$$n = \frac{ef}{h} \tag{2.25}$$

In two-dimensional electron gases without any parallel conduction, the carrier density extracted from SdH oscillations is in exact agreement with the carrier density from Hall measurements.

SdH oscillations can also be used to extract the effective mass and the quantum lifetime of the sample. The amplitude in resistance of a SdH oscillation is [56, 57]:

$$\Delta R = 4R_0\chi(T)e^{-\pi/\omega_c\tau_q} \tag{2.26}$$

where τ_q is the quantum lifetime, R_0 is the zero-field resistance, w_c is the cyclotron frequency $w_c = qB/m^*$, and $\chi(T)$ is the thermal damping, which is defined as:

$$\chi(T) = (2\pi^2 kT/\hbar\omega_c)/sinh(2\pi^2 kT/\hbar\omega_c) \tag{2.27}$$

To extract the effective mass, the temperature dependence of the oscillation amplitude is measured, and then the decay of the oscillation amplitude is fitted to the $\chi(T)$. The effective mass of quantum wells is often different than that of the bulk material due to hybridization of the quantum well with the barrier material. With the thermal damping now known, the ΔR can be normalized by $4R_0$ and $\chi(T)$. If the logarithm is taken of the normalized ΔR, then the following equation can be obtained:

$$ln(\frac{\Delta R}{4R_0\chi(T)}) = -\frac{\pi m^*}{eB\tau_q} \tag{2.28}$$

The logarithm of the normalized oscillation amplitude can be plotted for different

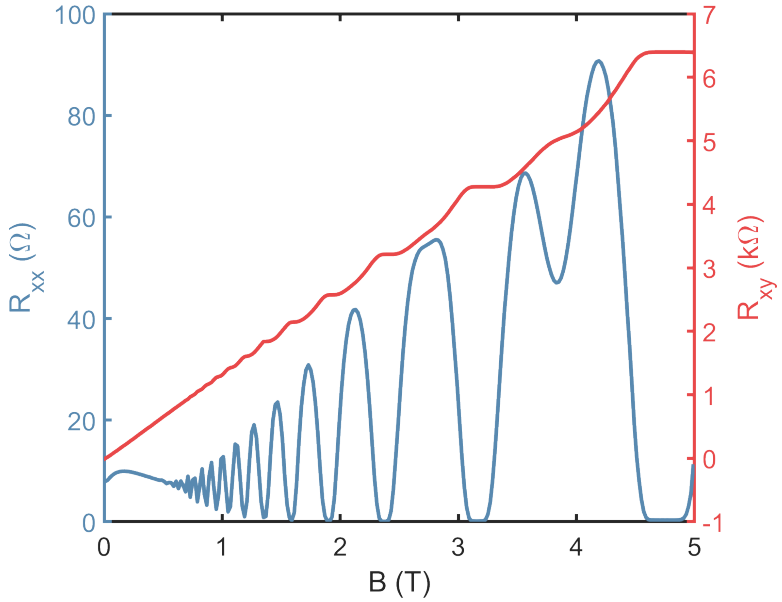


Figure 2.8: Magnetotransport of a GaAs 2D electron gas at 2 K measured in the van der Pauw geometry. The integer quantum hall effect is visible.

oscillations in $1/B$ and then be fitted to a line to extract the quantum lifetime. These plots are often called "Dingle plots". The quantum lifetime relates to the broadening of the Landau levels. The transport lifetime is insensitive to small angle scattering, and is often significantly larger than the quantum lifetime in quantum wells [57]. Additionally, the quantum mobility can also be calculated with this quantum lifetime.

At larger magnetic fields, the Landau levels can become spin split due to Zeeman splitting of the spin degenerate Landau levels. The change in energy due to the Zeeman effect is:

$$\Delta E = g\mu_B B \tag{2.29}$$

where g is the g factor of the charge carrier. In free electrons, the g factor is 2. In solid state materials, the g factor can be significantly greater than 2 for small band gap semiconductors with strong spin-orbit coupling [58]. For these high g factor materials, the spin splitting of the Landau levels can be observed at lower magnetic field.

At high enough magnetic fields, the Landau levels become completely isolated from

each other and the integer quantum Hall effect can be observed in two-dimensional systems [59]. In the integer quantum Hall effect, when the Fermi-level is between Landau levels, The ρ_{xx} and σ_{xx} become zero and the bulk of the sample is insulating. In this state, conduction only occurs through edge state. The Hall resistance becomes quantized in units of:

$$\rho_{xy} = \frac{h}{e^2\nu} \tag{2.30}$$

where ν is an integer filling factor. If there is parallel conduction, the ρ_{xx} and σ_{xx} will decrease but not become zero. When the Fermi-level is in a Landau level, the bulk is conducting and the ρ_{xx} and σ_{xx} are nonzero, and ρ_{xy} will no longer be quantized. The integer quantum Hall effect in a GaAs 2D electron gas is shown in Fig 2.8, where the integer quantum hall effect and vanishing magneto resistance is observed. Zeeman splitting of the Landau levels can be observed beginning at B = 2.9 T.

Chapter 3

Enhanced mobility by digital alloying in InGaAs quantum wells

3.1 Improving mobilities in InGaAs quantum wells

InGaAs quantum wells with high In content (In $\geq$ 75%) have a smaller electron effective mass, smaller band gap energy, larger g-factor [58], and larger spin-orbit coupling [60, 61] compared to GaAs quantum wells. These properties of InGaAs quantum wells make high electron mobility quantum wells promising materials for topological quantum computing [32,33] and spintronics [17]. While alloying the GaAs with InAs both enables the tunability of the properties and enhances certain properties of the quantum wells, it introduces random alloy disorder in the material. This intrinsic random alloy disorder leads to alloy disorder scattering of charge carriers and is a limiting factor in high electron mobility InGaAs quantum wells. The current state of the art mobilities in high In content InGaAs quantum wells is $\sim$ 430,000 cm^2/V s [62] and alloy disorder scattering is a major scattering mechanism near the peak mobility [62, 63]. Reducing disorder and improving the mobilities in InGaAs is especially important in the application of topological quantum

computing, where it has been experimentally difficult to determine if this material can be used due to the high disorder in the material system [37]. Reducing the intrinsic alloy disorder scattering poses a significant challenge towards improving the mobilities of InGaAs quantum wells.

Digital alloys (DA) are an alternative approach to alloying by growing the material as a short period superlattice [64] instead of a random alloy. While the properties of digital alloys often closely resemble that of the random alloys, properties such as the band gap [64–66] and effective mass [67] can vary significantly. Digital alloys have been predominately implemented in optoelectronic devices such as low excess noise avalanche photodetectors [68] and low series resistance distributed Bragg reflectors [69]. There have been some studies on the transport of heterostructures grown with digital alloys, such as magnetically doped semiconductor quantum wells [70], parabolic quantum wells [71], and coupled multiple quantum wells [72, 73]. Digital alloys are potentially promising in improving the transport mobility of semiconductor alloys. By growing a digital alloy as an ordered structure comprised of binary semiconductors, which intrinsically do not posses any alloy disorder, it is expected that there is no alloy disorder scattering within the material and the transport mobility will increase [74, 75]. However, a systematic investigation in the effects of digital alloying on the alloy disorder scattering of charge carrier transport has yet to be performed.

In this work, random and digital alloy InGaAs quantum wells grown metamorphically on InP substrates are compared. InAs/GaAs and InAs/InGaAs superlattices are implemented as digital alloy quantum wells. The InAs/InGaAs DA quantum well has an enhanced mobility of 545,000 cm^2/V s, which is the highest reported mobility for high In content InGaAs quantum wells. The mobility of the InAs/GaAs DA quantum well is found to be reduced in comparison to the random alloy sample. By analyzing the scattering mechanisms of the different quantum wells, the enhancement of the InAs/InGaAs

DA mobility is due to a reduction in the alloy disorder scattering and the reduction of the InAs/GaAs DA mobility due to increased interfacial roughness and background impurity incorporation. Our results demonstrate that digital alloying is a promising way to improve the mobility of III-V semiconductor alloys, however care must be made with the growth and design of the digital alloys in order to enhance the mobility.

3.2 Experiment

Samples were grown on epi-ready semi-insulating Fe-doped InP (001) wafers (AXT Inc.) in a VG V80H MBE system. The oxide was desorbed by heating the InP wafers under an As_2 flux until the metal rich transition to a (4×2) surface reconstruction was observed by reflection high energy electron diffraction. This transition is used to calibrate the pyrometer temperature to 515 °C. After oxide desoprtion, 100 nm of a nearly lattice matched superlattice of 4 nm $In_{0.52}Al_{0.48}As$/ 1 nm $In_{0.52}Ga_{0.48}As$ was grown at 480 °C. The substrate was then cooled down to 340 °C, and a step graded buffer layer was grown from $In_{0.575}Al_{0.425}As$ to $In_{0.825}Al_{0.175}As$ in 50 nm thick steps, where the composition of In would change 2.5% each step. The buffer layer is then reverse stepped to $In_{0.75}Al_{0.25}As$ in 50 nm thick steps of 2.5% In composition changes. After the completion of the graded buffer layer, the substrate is heated to a pyrometer temperature of 470 °C where an $In_{0.75}Al_{0.25}As$ bottom barrier, a 30 nm $In_{0.81}Ga_{0.19}As$ quantum well, and an $In_{0.75}Al_{0.25}As$ top barrier are grown.

Mesas for Hall bars were fabricated using wet chemical etching with a mixture of H_2SO_4:H_2O_2:H_2O (1:8:120). Following mesa definition, NiGeAu contacts were deposited and subsequently annealed at 450 °C for 2 minutes to form ohmic contacts to the quantum well. A 30 nm AlO_x gate dielectric was deposited with atomic layer deposition. Finally, a Ti/Au top gate was deposted on the Hall bar. Fabrication was performed by Y. Gul.

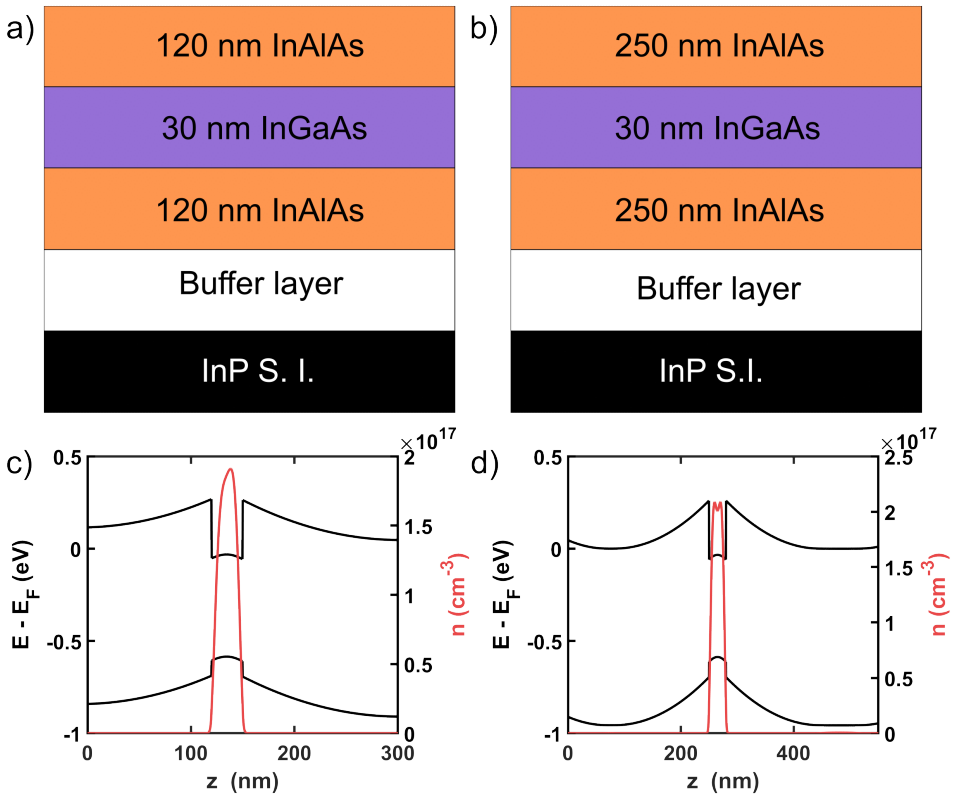


Figure 3.1: Heterostructure schematic for InAlAs barriers of a) 120 nm thickness and b) 250 nm thickness. 1D Schrödinger-Poisson of the c) 120 nm thick InAlAs barrier and d) 250 nm thick InAlAs barrier.

The width of the Hall bar was 80 μm, with an arm spacing of 740 μm. The ratio of the Hall bar width to the spacing of the arms was 9.25. Magnetotransport measurements were performed in a Quantum Design Physical Property Measurement System at 2 K using standard low frequency AC lock-in measurements, with an AC current of 0.5 μA. The two-dimensional electron gas (2DEG) carrier density was modulated by applying a voltage to the top gate electrode. Measurements of samples in the van der Pauw geometry were done with annealed InSn contacts performaed at 2 K with an AC current of 1 μA.

3.3 Heterostructure design

Unintentionally doped heterostructures [76, 77] and modulation doped heterostructures [61, 62] have been reported to be in electron accumulation. In the case of unintentionally doped heterostructures, it is believed that point defects in the InAlAs layer serve as an deep level donors to the InAlAs [76]. Due to the band alignments between the InAlAs and the InGaAs, the donor energies lie above the conduction band edge of the InGaAs, and doping occurs by charge transfer from the deep level donors to the quantum well. The density of the deep level donors can be modified by varying the growth conditions, and the origin of the deep level donors is believed to be an As intersitial point defect [78]. Both modulation doped and unintentionally doped heterostructures were investigated as part of this work. The quantum wells grown in this study are found to be in electron accumulation with unintentional doping. The quantum wells were typically overdoped, with the second subband being in electron accumulation as grown. The sheet carrier density of the quantum wells was found to have increased with modulation doping, with a doping efficiency of approximately 50% for a Si δ layer with a setback of 60 nm. However, modulation doping was found to be unnecessary, with modulated doped samples having a 12 % reduction in peak mobility, which is likely due to remote impurity scattering from the δ layer.

The thickness of the top and bottom $In_{0.75}Al_{0.25}As$ barriers are found to be of significant importance. In the InGaAs/InAlAs heterostructures, the unintentional deep donor levels in the InAlAs serve as the dopant source of the material. If the top and bottom barriers are too thick, then charge transfer from these layers to the InGaAs cannot occur, and electron accumulation can occur within the top and bottom layers. For quantum wells with top or bottom barrier thicknesses exceeding 200 nm, parallel conduction was observed in the magnetotransport. This process is modeled with a 1D Schrödinger-

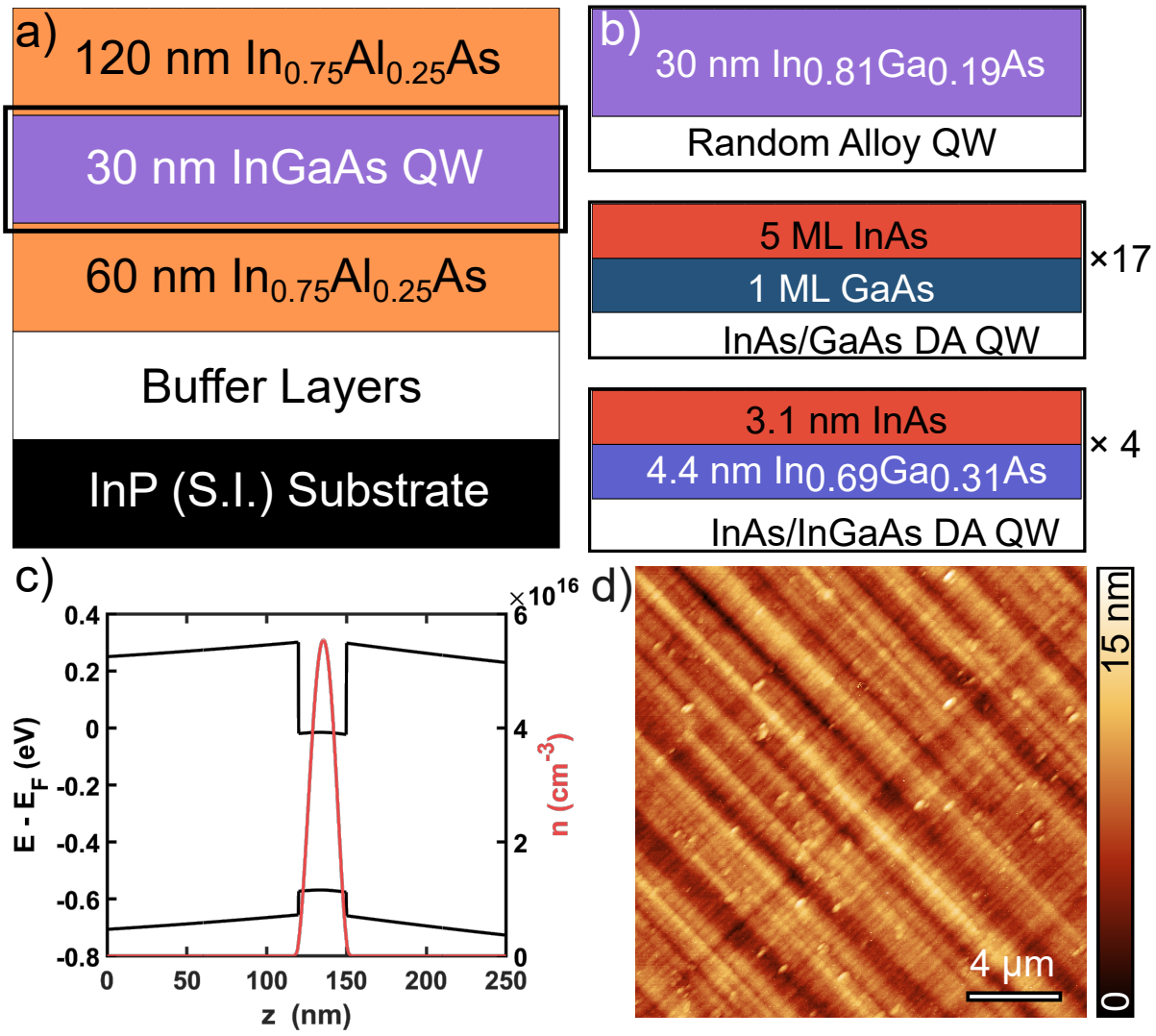


Figure 3.2: a) Sample structure schematic, consisting of a 30 nm thick InGaAs quantum well buried 120 nm from the surface. The quantum wells were grown metamorphically on InP subsrates. b) Different samples in the study: a random alloy quantum well, a 17 period InAs/GaAs digital alloy quantum well, and a 4 period InAs/InGaAs digital alloy quantum well. c) Self consistent Schrödinger-Poisson simulation of the sample structure. d) Representative AFM micrograph of InAlAs top barrier, cross hatching typical of metamorphic growth is observed. AFM courtesy of T. A. J. van Schijndel. Reprinted with permission from [79]. Copyright 2024 by the American Physical Society.

Poisson using the methods described in [3], and shown in Fig. 3.1, where the conduction band edge of the 250 nm InAlAs barriers begins to touch the Fermi-level. To prevent parallel conduction within the barriers, the barrier thickness is required to be thin enough to allow charge transfer from the donor states into the InGaAs layer.

The layer schematic for the samples investigated with gated magnetotranpsort in this work are shown in Fig. 3.2(a). The InGaAs quantum well is grown as either a random alloy or a digital alloy, shown schematically in Fig. 3.2(b). The 30 nm random alloy sample serves as a reference point for comparison with the digital alloyed quantum wells. Two different digital alloy quantum wells with a total thickness of 30 nm are grown: an InAs/GaAs digital alloy quantum well consisting of 17 periods of 5 monolayers of InAs and 1 monolayer of GaAs and an InAs/InGaAs digital alloy quantum well consisting of 4 periods of 3.1 nm of InAs and 4.4 nm of $In_{0.69}Ga_{0.31}As$. For the digital alloy samples, a 1 second growth interrupt between the layers was included to improve the ordering at the interfaces. The 1D Schrödinger-Poisson calculations of the heterostructure band structure are shown in Fig. 3.2(c), showing the accumulation of electrons in the InGaAs quantum wells in the unintentionally doped heterostructure. The surface morphology of the InAlAs top barrier is shown in the atomic force micrograph shown in Fig. 3.2(d). A cross-hatched morphology typical of metamorphic growth is observed, with the rms roughness of the InAlAs top barrier over a 400 μm^2 area typically 1-2 nm.

The GaAs layer thickness in the InAs/GaAs digital alloy could not exceed 1 monolayer, growth thicker than 1 monolayer resulted in the relaxation of the GaAs layer. Evidence of this relaxation is seen in the extremely anisotropic resistance of the InAs/GaAs digital alloy quantum wells. The magnetotresistance anisotropy for a InAs/GaAs digital alloy with a 2 monolayer thick GaAs layer is shown in Fig. 3.3. The anisotropy factor between the two directions is 143. This magnetoresistance anisotropy is indicative of relaxation of the quantum well by self assembly into quantum wires [80, 81]. For

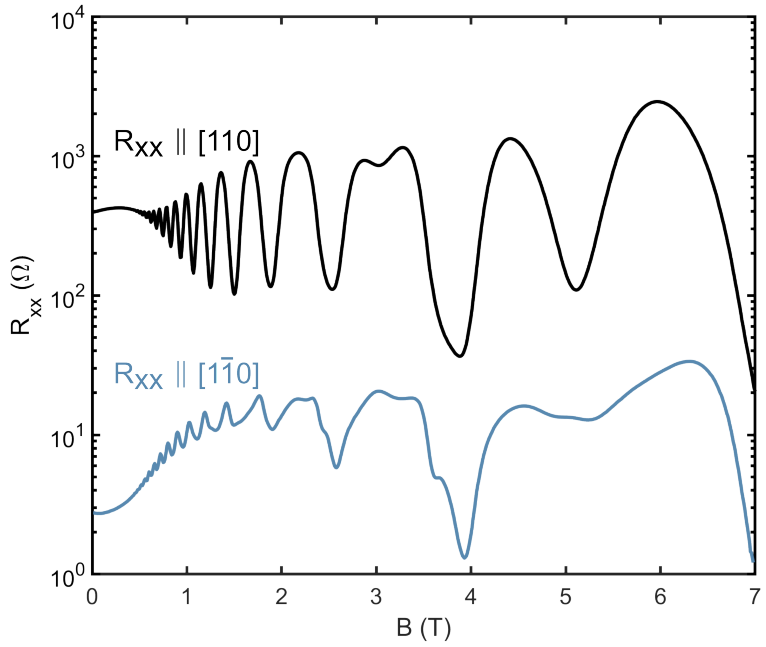


Figure 3.3: Orientation dependent magnetoresistance of a 2 monolayer thick GaAs/9 monolayer thick InAs digital alloy quantum well at 2 K.

InAs/GaAs digital alloys with GaAs period thickness less than 1 monolayer, the resistance anisotropy was not observed. The design of the InAs/GaAs digital alloy quantum wells is constrained by the critical thickness of the GaAs layer on the virtual InAlAs substrate, and these results indicate the management of the strain of digital alloys with extremely different lattice constants is an important design consideration.

3.4 Quantum well band structure

The band structure of the random and digital alloy quantum wells was computed using the $k \cdot p$ method for heterostructures with the envelope function approximation, using the methods described in [2]. The first four conduction band subband energies and their associated probability densities ($|\psi|^2$) for the three different samples are plotted in Fig. 3.4. The $|\psi|^2$ of the random alloy and the InAs/GaAs DA quantum wells are

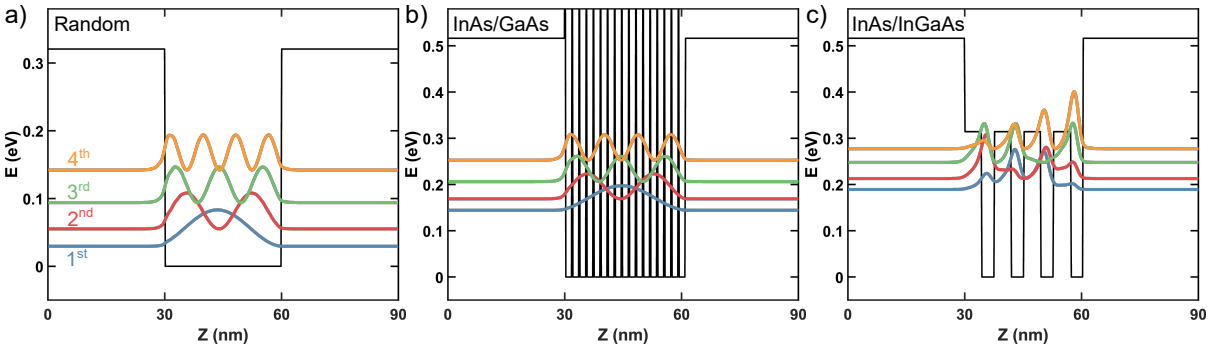


Figure 3.4: Plots of the conduction band edges and the $|\psi|^2$ of the first four conduction band subbands of the: a) random alloy, b) InAs/GaAs DA, and c) InAs/InGaAs DA quantum wells calculated with the $k \cdot p$ method. Reprinted with permission from [79]. Copyright 2024 by the American Physical Society.

sinusoidal-like envelop functions over the channel of the quantum well. However, for the $|\psi|^2$ in the InAs/InGaAs digital alloy, the $|\psi|^2$ are the sinusoidal-like envelope functions of the quantum well with peaks in the InAs layers and troughs in the InGaAs regions. Although the InAs/InGaAs digital alloy still has alloy disorder present through the use of the InGaAs layers, the overall alloy disorder scattering may be reduced by having the electron preferring to reside in the InAs regions of the digital alloy. The band parameters of the quantum wells are summarized in Table 3.1, which contains the predicted energy gap of the quantum wells, the subband spacing between the 1^{st} and 2^{nd} electron subbands, the 1^{st} subband effective mass (m^*), and the nonparabilicity factor (α). α is defined with: $E(1+\alpha E) = \frac{\hbar^2 k^2}{2m^*}$, where E is the Fermi energy and k is the Fermi wavevector.

From the $k \cdot p$ calculations, it is expected that subbands form in the digital alloy

Table 3.1: $k \cdot p$ results including band gap energy (E_g), subband spacing ($E_2 - E_1$), 1_{st} subband effective mass (m^*), and effective mass nonparabilicity (α). Reprinted with permission from [79]. Copyright 2024 by the American Physical Society.

Sample	E_g (meV)	$E_2 - E_1$ (meV)	m^* (m_e)	α
Random Alloy	573	25.7	0.0347	1.955
InAs/GaAs DA	566	24.7	0.0334	2.134
InAs/InGaAs DA	551	23.6	0.0345	2.324

and random alloy quantum wells, with the digital alloy quantum wells having a slightly smaller subband spacing than the random alloy quantum wells. The predicted effective masses and nonparabilicity of the quantum wells is not expected to change significantly. However, it is predicted that the InAs/GaAs DA quantum well to have a slightly smaller effective mass compared to the InAs/InGaAs DA and the random alloy quantum wells. The predicted results for the InAs/GaAs DA may be incorrect, as the $k \cdot p$ method can be less accurate in simulation of monolayer thick heterostructures, which is discussed in depth in [82].

3.5 Magnetotransport

An optical image of a Hall bar used in this study with the schematic wiring diagram is shown in Fig. 3.5(a). The R_{xx} and R_{xy} from B = 0 T to B = 14 T for the random and digital alloy quantum wells is shown in Fig. 3.5(b-d), with $n_{2DEG} = 3.52 \times 10^{11}$, 2.78×10^{11}, and 3.60×10^{11} cm^{-2} for the random alloy, InAs/GaAs DA, and InAs/InGaAs DA, respectively. n_{2DEG} is the sheet electron density extracted from the Hall measurements. The integer quantum Hall effect is observed along with vanishing magnetoresistance for all samples. In both of the digital alloy quantum wells, single band transport is observed and the transport does not resemble the coupled multiple quantum well transport observed in GaAs/AlAs digital alloy quantum wells [72, 73]. This difference is potentially due to stronger coupling between the sublattices of the digital alloy compared to the GaAs/AlAs. Plots of the magnetoresistance at various gate voltages for the different samples are shown in Fig. 3.6. At lower (more negative) gate voltages, a single set of Shubnikov–de Haas oscillations is observed in all of the quantum wells. At higher gate voltages, the second subband becomes occupied and an additional set of oscillations is observed for all of the samples. These results demonstrate the formation of a high quality two-dimensional

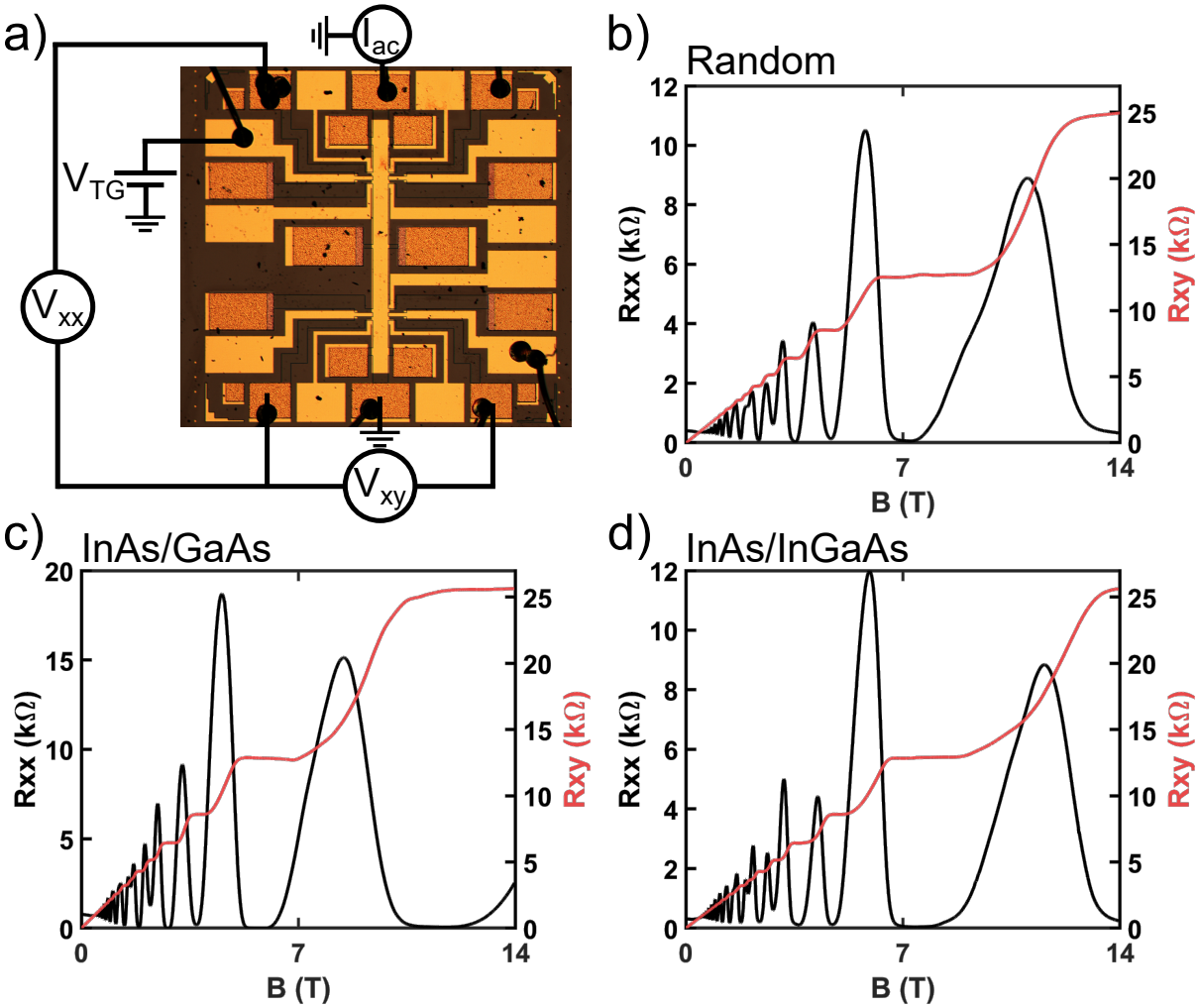


Figure 3.5: a) Optical image of the Hall bar and schematic sample wiring. 2 K magnetotransport of the: b) random alloy sample at $n_{2DEG} = 3.52 \times 10^{11}$ cm^{-2}. c) InAs/GaAs DA sample at $n_{2DEG} = 2.78 \times 10^{11}$ cm^{-2}. d) InAs/InGaAs DA sample at $n_{2DEG} = 3.60 \times 10^{11}$ cm^{-2}. Reprinted with permission from [79]. Copyright 2024 by the American Physical Society.

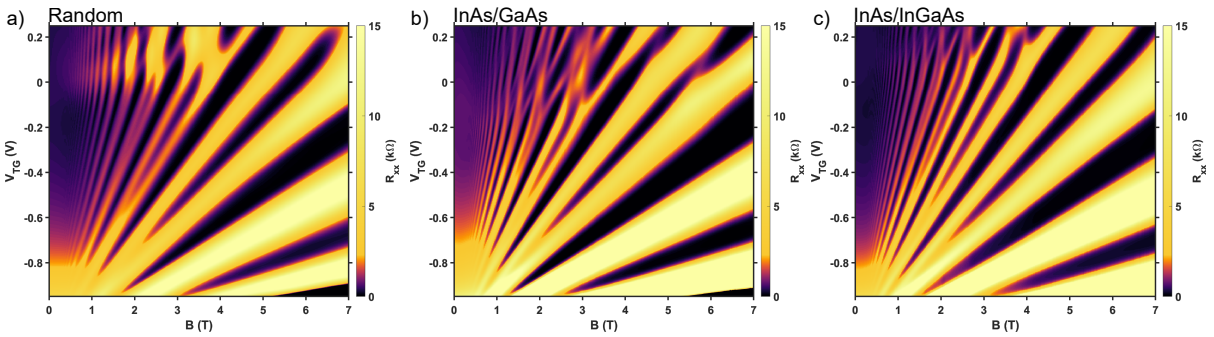


Figure 3.6: R_{xx} at different top-gate voltages and magnetic fields for: a) random alloy, b) InAs/GaAs DA, and c) InAs/InGaAs DA. Reprinted with permission from [79]. Copyright 2024 by the American Physical Society.

Table 3.2: Sample parameters including the peak mobility, carrier density at the peak mobility, the effective mass from thermal damping, and the estimated Fermi energy at the peak mobility. Reprinted with permission from [79]. Copyright 2024 by the American Physical Society.

Sample	μ_{max} (10^3 cm^2/Vs)	n_{2DEG} at μ_{max} (10^{11} cm^{-2})	m^* (m_e)	ε_f at μ_{max} (meV)
Random Alloy	460	3.13	0.030 ± 0.001	25.0
InAs/GaAs DA	281	2.59	0.030 ± 0.001	20.7
InAs/InGaAs DA	545	3.37	0.033 ± 0.002	24.5

electron gas devoid of parallel conduction in the random alloy quantum well and the digital alloy quantum wells.

From the magnetotransport at various gate voltages, the mobility at different carrier densities can be determined and are shown in Fig. 3.7 for the different quantum wells. The random alloy digital alloy quantum well has a peak mobility of 460,000 cm^2/Vs at a n_{2DEG} of 3.13×10^{11} cm^{-2}, the InAs/GaAs DA quantum well has a peak mobility of 281,000 cm^2/Vs at a n_{2DEG} of 2.59×10^{11} cm^{-2}, and the InAs/InGaAs DA quantum well has a peak mobility of 545,000 cm^2/Vs at a n_{2DEG} of 3.37×10^{11} cm^{-2}. The mobility of the random alloy quantum well is slightly higher than the mobility of 430,000 cm^2/Vs reported in the current state of the art high In content InGaAs quantum wells [62]. The InAs/InGaAs DA quantum well has a higher peak mobility at a higher carrier density

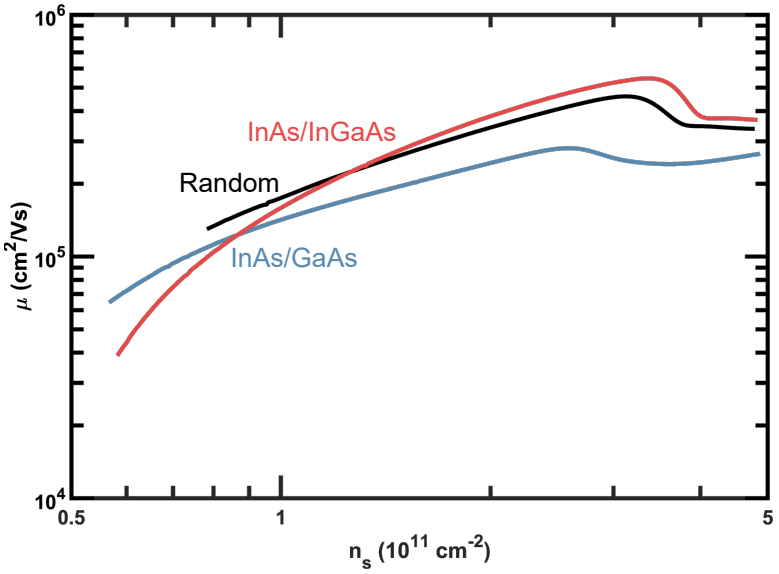


Figure 3.7: The dependence of mobility on sheet carrier density for the three different samples. Carrier density was varied by modifying the top gate voltage. Reprinted with permission from [79]. Copyright 2024 by the American Physical Society.

than the random alloy quantum well, while the InAs/GaAs DA samples have a lower peak mobility at a lower carrier density than the random alloy quantum well. From the results shown in Fig. 3.6, the decrease in mobility after the peak mobility in all of the samples is likely due to intersubband scattering.

The electron effective mass is extracted from the thermal damping on the Shubnikov–de Haas oscillations (Fig. 3.8). The oscillations are isolated by subtracting a low order polynomial background from the data. The temperature dependence of the peak magnitude of the oscillations are fit to equation 2.27 to extract the effective mass for different oscillations. The effective masses from the different oscillations were averaged to obtain the effective mass of the quantum well. The effective masses were used to estimate the Fermi energy at the peak mobility and to estimate the subband splitting. These results are summarized in Table 3.2. All of the samples have smaller effective masses than the predicted effective masses from the $k \cdot p$ calculations, and in the case of the random alloy and the InAs/GaAs DA quantum wells, they have smaller effective masses than

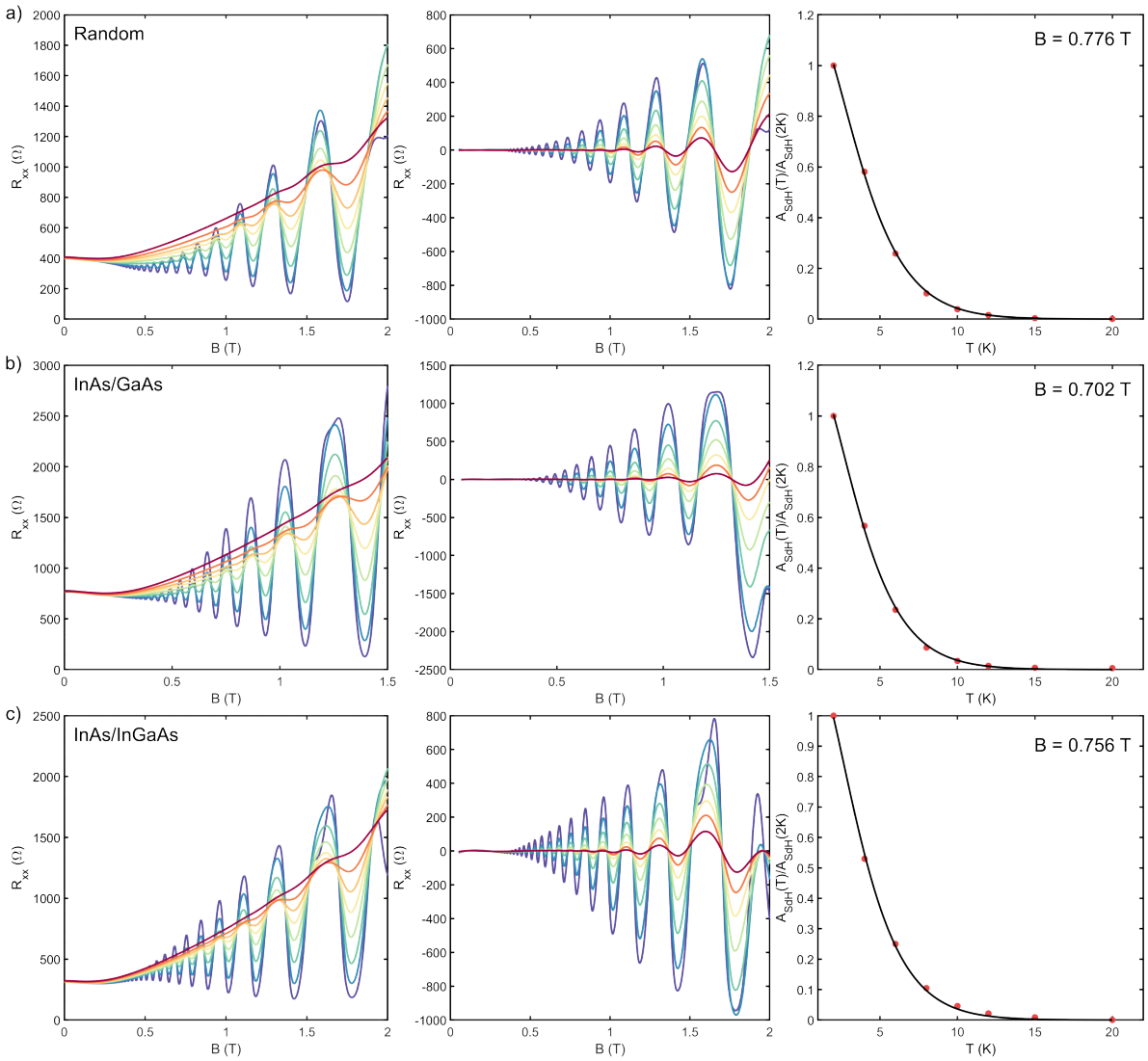


Figure 3.8: Temperature dependence of the SdH oscillations, with the raw magnetoresistance, the magnetoresistance after background subtraction, and the fit to the thermal damping of the oscillations for a) the random alloy QW, b) the InAs/GaAs DA QW, and c) the InAs/InGaAs DA QW. The measurement temperature ranged from 2 K to 20 K.

Table 3.3: The transport lifetimes (τ_t) and quantum lifetimes (τ_q) of the samples at the peak mobility as well as the ratio of the two lifetimes and the onset of Shubnikov de-Haas oscillations (B_{on}). Reprinted with permission from [79]. Copyright 2024 by the American Physical Society.

Sample	τ_t (ps)	τ_q (ps)	τ_t/τ_q	B_{on} (T)
Random Alloy	7.85	0.21	37.4	0.23
InAs/GaAs DA	4.79	0.27	17.7	0.23
InAs/InGaAs DA	10.23	0.31	33.0	0.22

0.0314 m_e, which is the expected bulk effective mass of InGaAs accounting for strain effects calculated using $k \cdot p$ [2]. This reduction in effective mass is likely due to electron-electron correlations, and has been observed before in GaAs quantum wells [83]. The subband energies estimated from the effective mass and the peak carrier density for the random and the InAs/InGaAs DA are within ~ 1 meV of the predicted subband energies, and the higher carrier density at the peak mobility for the InAs/InGaAs quantum well is due to the larger effective mass of the InAs/InGaAs sample. However, the InAs/GaAs DA quantum well subband energy is significantly different than the predicted, and may be due to the aforementioned potential inaccuracies of the $k \cdot p$ method for monolayer heterostructures.

With the effective mass of the samples known, the transport (τ_t) and quantum (τ_q) lifetimes of the samples at the peak mobility are given in Table 3.3. The transport lifetimes were calculated from the following equation: $\tau_t = \frac{\mu m^*}{e}$. The quantum lifetime was extracted from the amplitude of the quantum oscillations normalized by the thermal damping of the oscillations using equation 2.28. The Dingle plots used to extract the quantum lifetime is shown in Fig. 3.9. Deviations from linear behavior in the Dingle plots can be observed. These deviations are likely due to inhomogeneities in the quantum well [56, 57]. The magnetic field onset (B_{on}) of the SdH oscillations is often correlated with the quantum lifetime and is provided in the table. The difference in transport lifetime between the different samples reflects the differences in the mobility, with the

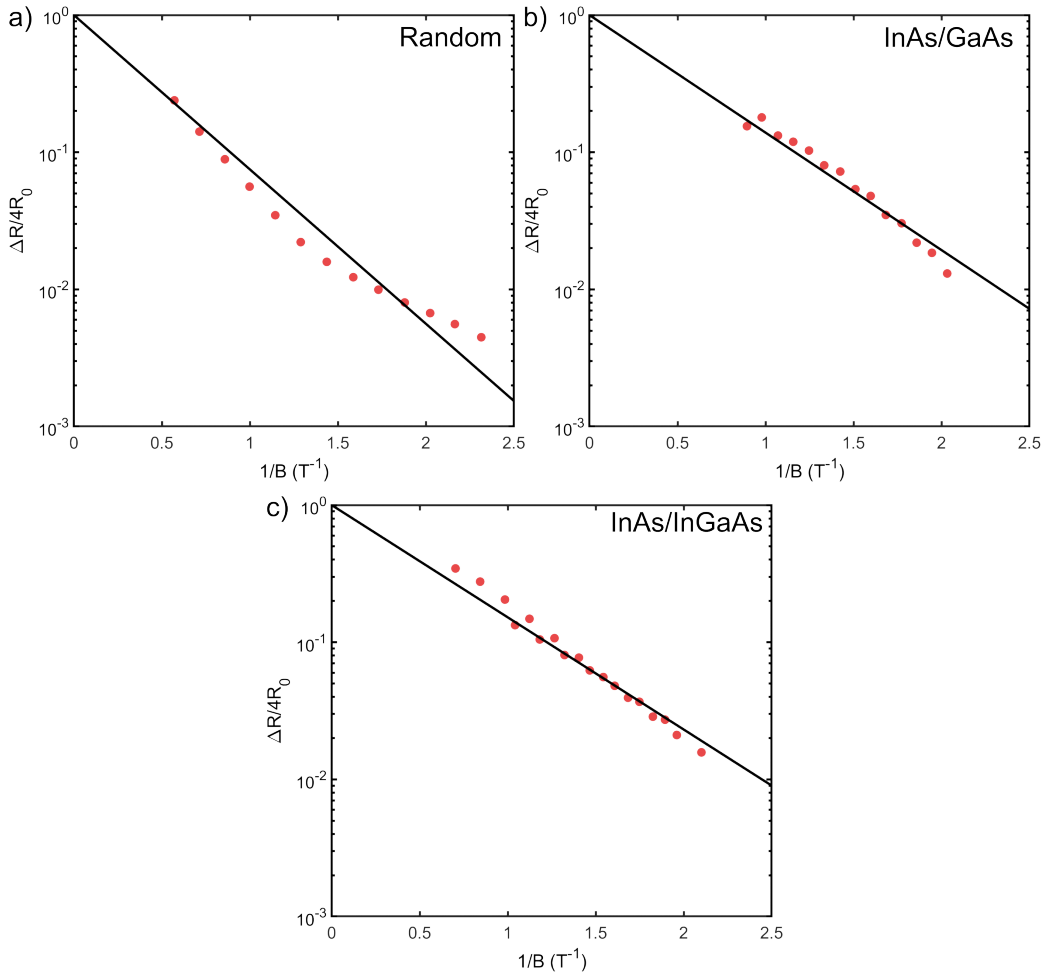


Figure 3.9: Dingle plots for the a) random alloy, b) InAs/GaAs DA, and c) InAs/InGaAs.

InAs/InGaAs DA QW having the highest lifetime and the InAs/GaAs DA QW having the lowest lifetime. All of the samples have similar B_{on}, which indicates that the quantum lifetimes are similar. From the extracted quantum lifetimes of the samples, the random alloy sample has the lowest quantum lifetime, and the two DA samples have higher lifetimes, with the InAs/InGaAs DA having the highest quantum lifetime. The ratio of the transport lifetimes to the quantum lifetime is also provided in the table. The transport lifetime is significantly higher than the quantum lifetime, consistent with the transport lifetime being insensitive to small angle scattering, while the quantum lifetime is sensitive to all scattering events, and is generally more sensitive to long range scattering [84]. These results indicate that digital alloying can improve the quantum lifetime in quantum wells.

3.6 Scattering mechanisms

To understand the differences in the mobility and the scattering mechanisms for the different samples, the mobilities were modeled using a calculation for the elastic scattering time of electrons in the two-dimensional electron gas [85]. The calculations accounted for background impurity scattering [86], interfacial roughness scattering [87, 88], remote impurity scattering [86], and alloy disorder scattering [89]. Zero temperature was assumed and intersubband scattering was not considered. The exact details of the calculations are given in appendix A. The remote impurity scattering was treated as a fixed sheet charge of 2×10^{12} cm^{-2} at the top surface of the quantum well, which is an overestimate of the surface state density of InAlAs [90–93]. However, the exact surface state density of the remote impurities at the surface is found to be not important, as the contribution of remote impurity scattering from the top surface is found to have negligible effect on the mobility of the quantum wells due to the depth of the quantum well from the surface. The parameters for the other scattering mechanism were varied to obtain good agreement

Table 3.4: Mobility modeling parameters including alloy disorder potential (dV), background impurity density (n_{BI}), interface roughness (Δ), and correlation length (Λ). Reprinted with permission from [79]. Copyright 2024 by the American Physical Society.

Sample	dV (eV)	n_{BI} (cm^{-3})	Δ (Å)	Λ (nm)
Random Alloy	0.44	1.5×10^{15}	6	13
InAs/GaAs DA	0.44	2.4×10^{15}	21	3
InAs/InGaAs DA	0.38	1.6×10^{15}	6	13

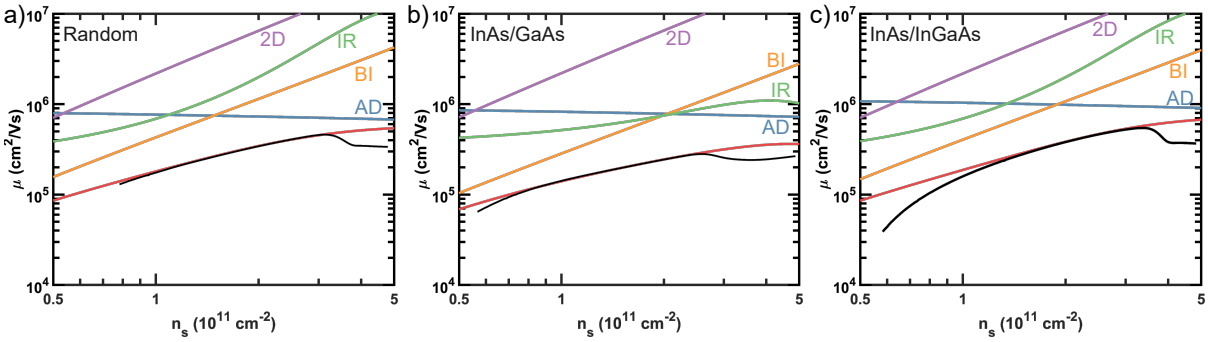


Figure 3.10: Experimentally measured mobility and calculated mobility at various sheet carrier densities for the: a) random alloy, b) InAs/GaAs DA, and c) InAs/InGaAs quantum wells. The total mobility and the individual mobilities for the different scattering mechanisms including: interfacial roughness scattering (IR), two-dimensional remote impurity scattering (2D), background impurity scattering (BI), and alloy disorder scattering scattering (AD) are plotted. Reprinted with permission from [79]. Copyright 2024 by the American Physical Society.

with the experimental data, and are given in Table 3.4. The transport lifetimes due to the different scattering were calculated independently, and the total mobility was computed using Matthiessen's rule [94].

The mobilities of the samples at different carrier densities and the calculated mobilities are shown in Fig. 3.10. The calculated total mobility and the mobility for the different scattering mechanisms are also shown. There is good agreement between the calculated mobility and the measured mobility for all of the samples at higher carrier densities until the peak mobility is reached, where the measured mobility begins to decrease due to intersubband scattering between the 1st and 2nd subbands, which is not accounted

for with the mobility calculations. In all of the samples, two distinct regimes can be observed, alloy disorder scattering dominates at higher carrier densities and background impurity scattering dominates at lower carrier densities. This behavior is similar to what has been observed in prior studies of InGaAs quantum wells [62, 63].

A higher background impurity density is required to accurately model the mobilities of the InAs/GaAs (2.4×10^{15} cm^{-3}) and the InAs/InGaAs (1.6×10^{15} cm^{-3}) digital alloy quantum wells than the random alloy quantum well (1.5×10^{15} cm^{-3}). The background impurity densities extracted from the modeling are similar to what has been previously reported in InGaAs quantum wells [62, 63, 76]. The InAs/GaAs DA has more interfaces, with the 17 periods of InAs/GaAs, than the InAs/InGaAs DA, with 4 periods, and has a higher estimated background impurity density than the InAs/InGaAs DA. This trend suggests that the higher background impurity density is due to impurity incorporation at the interfaces of the digital alloy during growth, which has been observed to occur at the interfaces of superlattices grown by MBE [95,96]. The origin of these additional impurities could be from the brief growth interrupt during the growth of the digital alloys. From these results, it is desirable to reduce the number of periods in the superlattice to reduce the background impurity density and therefore the background impurity scattering for the growth of high mobility samples.

The interfacial roughness in the random and InAs/InGaAs digital alloy is estimated from the model to be 6 Å. This value is smaller than the roughness measured by atomic force microscopy of the InAlAs top barrier, which we attribute due to the InGaAs layers being smoother than the InAlAs layers at the growth temperature. The interfacial roughness of the random and InAs/InGaAs DA quantum wells is comparable to prior studies of the interfacial roughness of InGaAs quantum wells [62]. However, the modeled interfacial roughness of the InAs/GaAs is significantly higher, with a roughness of 21 Å. The increased roughness becomes a significant scattering mechanism at higher carrier

densities in the InAs/GaAs digital alloy. The increased roughness is likely due to the growth of rougher GaAs islands as the GaAs layer in the InAs/GaAs digital alloy. GaAs has been reported to grow as islands on InAs layers [97]. These results demonstrate that the optimal growth temperature of the constituent layers of the digital alloy is an important consideration, and can result in rougher growth and enhanced interfacial roughness scattering.

In order to accurately model the experimental data, the alloy disorder potential in the random alloy quantum well is estimated to be 0.44 eV. This value is larger than the 0.3 eV reported previously in InGaAs quantum wells [62], but closer to the expected value of 0.5 eV of InGaAs [98]. We find that the same alloy disorder potential of 0.44 eV is required to obtain a good agreement to the experimental InAs/GaAs DA mobility curves, which we propose is due to significant intermixing in the InAs/GaAs layers creating alloy disorder. In the InAs/InGaAs digital alloy, the alloy disorder potential is estimated to be 0.38 eV from the modeling, this alloy disorder potential is smaller than the alloy disorder of the random alloy. The reduction in the alloy disorder potential is likely due to the electrons preferentially residing in the InAs regions of the digital alloy, as seen in the $k \cdot p$ results in Fig. 3.4c, and as a consequence the electron do not spend as much time in the regions of the quantum well that posses alloy disorder. The overall increase in mobility observed in the InAs/InGaAs DA quantum well over the random alloy quantum well is due to this reduction in alloy disorder scattering. These results as a whole suggest that digital alloying can be used to reduce alloy disorder scattering in quantum wells and the importance of the heterostructure design and the interfaces in the mobility of digital alloy quantum wells.

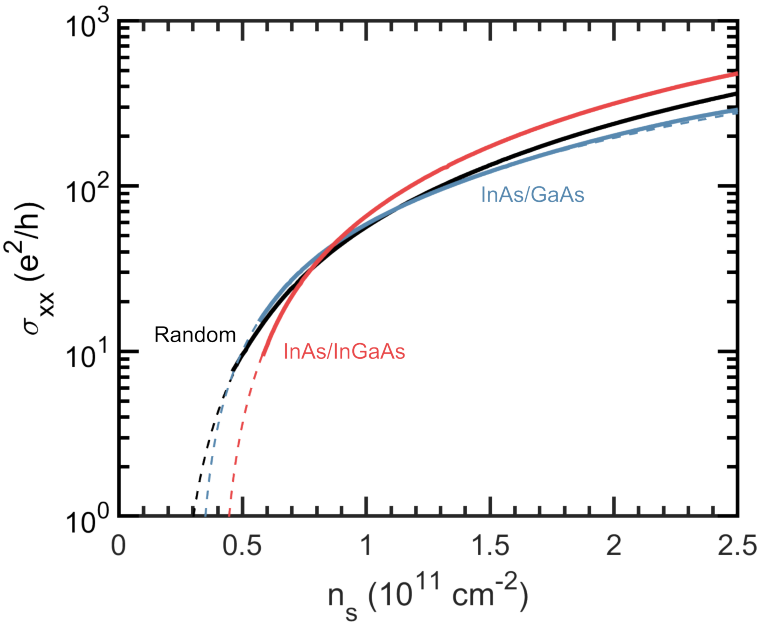


Figure 3.11: The dependence of the conductivity on sheet carrier density for the three different samples.

3.7 Metal-insulator transition in the quantum wells

The measured mobility begins to diverge from the calculated and is lower than what the calculations would predict at carrier densities lower than $\sim 1 \times 10^{10}$ cm^{-2}. This deviation in mobility is due to a metal-insulator transition in the quantum wells [99–101]. The metal-insulator transition can be described as a percolation transition, where at low carrier densities and thus less screening of disorder, disorder begins to trap the charge carrier into localized regions. Conduction can now be described as percolation of charge carriers between these conduction regions. The percolation transition can be characterized by fitting carrier density dependence of the conductivity near the transition region to a simple power law:

$$\sigma_{xx}(n) \propto (n - n_c)^{\delta} \tag{3.1}$$

Table 3.5: Fitting parameters to the low carrier density conductivity of the quantum wells including the percolation density (n_c) and power law exponent (δ).

Sample	n_c (cm^{-2})	δ
Random Alloy	2.27×10^{10}	1.73
InAs/GaAs DA	3.18×10^{10}	1.33
InAs/InGaAs DA	4.03×10^{10}	1.59

Where n_c is the percolation density or the carrier density at which the samples become insulating. δ is predicted to be 4/3 for two-dimensional systems [102].

The conductivity at different sheet carrier densities as well as the fit to the power law is shown in Fig. 3.11. The results of the fits are summarized in Table 3.5. The fitted δ for the random alloy and the InAs/InGaAs DA are not 4/3, which is potentially due to the measurement temperature of 2 K. The δ has been reported to have a temperature dependence, and converges towards 4/3 at mK temperatures [103]. An increase in the n_c can be observed for the digital alloyed samples, with the InAs/InGaAs DA sample having the highest n_c. The increase in n_c is potentially due to the sublattice of the digital alloy serving as an additional localization mechanism. At low carrier densities, charge carriers can also become trapped in the InAs sublattice. The n_c of the InAs/GaAs DA is lower than the n_c of the InAs/InGaAs DA, and is potentially due to quantum confinement increasing the effective conduction band edge of in the InAs sublattice for the InAs/GaAs DA, reducing the effect of the sublattice carrier trapping.

3.8 Summary

In summary, digital alloys can be used as an alternative to random alloys in semiconductor quantum wells and increase the quantum well mobility by reducing the alloy disorder scattering. The quantum lifetime is also found to increase by digital alloying. Single subband transport, the integer quantum Hall effect, and the absence of parallel

conduction are observed in the random and digital alloys. However, increased background impurity density is observed in the digital alloys, likely due to incorporation of impurities at the interfaces. The results indicate the digital alloy should be grown with as few periods as possible to improve the mobility of the digital alloy quantum wells over that of the random alloy. Additionally, the quality of the interfaces and the growth conditions are important, otherwise alloy disorder and enhanced interfacial roughness scattering can be introduced into the digital alloy quantum wells and subsequently reduce the mobility. Finally, increased localization of charge carriers at low carrier densities was observed in digital alloyed samples, and the percolation density of the digital alloyed samples increased. These results should be generally applicable to other semiconductor alloys, and can be used to increase the mobility in other material systems.

3.9 Acknowledgements

This growth of the quantum wells was supported by University of California Multiple Campus Award No. 00023195. Modeling efforts of the quantum wells was supported by the Department of Energy under award No. DE-SC0019274. The use of shared facilities of the NSF Materials Research Science and Engineering Center (MRSEC) at the University of California Santa Barbara (Grant No. DMR 2308708) and the Nanotech UCSB Nanofabrication Facility is acknowledged.

Chapter 4

Spin-orbit coupling in digital alloyed quantum wells

4.1 Increasing spin-orbit coupling in InGaAs quantum wells

Spin-orbit coupling (SOC) is relativistic effect that can cause normally spin degenerate bands to become spin split due to inversion symmetry breaking. InGaAs quantum wells with strong spin-orbit coupling are potentially useful for spintronics [17, 19], topological quantum computing [32, 33], and as a platform for mesoscopic physics experiments [104, 105]. Increasing the spin-orbit coupling of the quantum well is often desirable. In spin field effect transistors, a stronger spin orbit coupling enables shorter channel length and thus allows for better scaling. In the application of topological quantum computing, increasing the spin-orbit coupling is expected to increase the topological gap of the system. The reported topological gaps are ~ 10 μeV [37], and the parameter space the topological gap is reported to exist is extremely narrow, making the scaling of

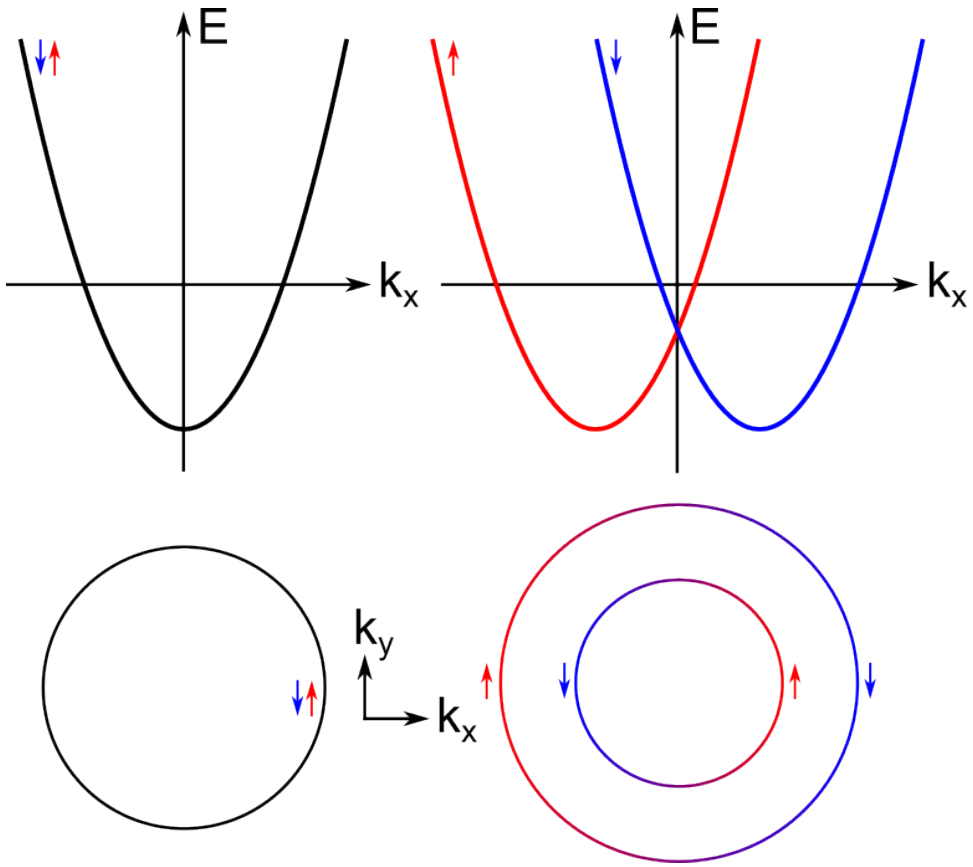


Figure 4.1: Schematic band dispersion and Fermi-surface without (left) and with Rashba spin-orbit coupling (right).

multiple devices challenging. Increasing the spin-orbit coupling is a potential approach to address these problems.

In III-V quantum wells such as InGaAs, Dresselhaus [7] and Rashba [6] spin-orbit coupling are both present. The change in the Fermi-surface due to Rashba spin splitting is shown in Fig 4.1. Dresselhaus spin-orbit coupling arises from the inversion asymmetry of the crystal structure, while Rashba spin-orbit coupling arises from inversion asymmetry of the heterostructure due to interfaces and electric fields within the heterostructure. The Dresselhaus spin splitting is typically significantly smaller than the Rashba spin splitting in III-V quantum wells [8–10,12]. The spin-orbit coupling in the heterostructures can be increased with the Rashba effect. By increasing the electric field within the

quantum well, typically with a gate electrode, the Rashba spin-orbit coupling can be increased. Increasing the spin-orbit coupling of the system with an external electrical field can cause detrimental effects in the heterostructure. At larger gate voltages and larger electric fields, the mobility of the system can decrease due to the quantum confined Stark effect increasing interfacial roughness scattering [88], and the second subband can become occupied, which can also reduce mobility due to intersuband scattering [12,106,107]. It is desirable to increase the spin-orbit coupling of the material system without significantly reducing the charge carrier mobility of the system to take advantage of the potential benefits high spin-orbit coupling can offer.

Digital alloying is a potential approach towards increasing the spin-orbit coupling of the system. Digital alloys (DA) are short period superlattices that can approximate the properties of random alloys. Increases in the charge carrier mobility by digital alloying was demonstrated in Chapter 3. Digital alloying can allow for increased asymmetry in the heterostructure by being able to form asymmetric interfaces at the top and bottom interface as well as an easy method of compositional grading within the heterostructure by varying the relative sublattice thicknesses. Due to these properties of digital alloys, it is anticipated that they may be a promising method to increase the spin-orbit coupling of the system. To date, negligible changes in the spin-orbit coupling in triangular GaAs quantum wells have been demonstrated by digital alloying [108], and it has been predicted that digital alloying can induce modest changes to the Rashba spin-orbit coupling in triangular InGaAs and InSb quantum wells [109].

In this work, the effect of digital alloying on the spin-orbit coupling in $In_{0.81}Ga_{0.19}As$ QW grown on InP substrates is investigated. A random alloy QW, a nongraded InAs/GaAs DA QW, a nongraded InAs/InGaAs DA QW, and a 3% compositionally graded InAs/InGaAs DA were studied. Significant increases in the Rashba coefficient were observed in the InAs/GaAs DA sample, while more modest changes were observed in the graded and

nongraded InAs/InGaAs DA sample. The changes in both of the InAs/InGaAs DA samples can qualitatively be explained with $k \cdot p$ theory, while the changes in the InAs/GaAs DA sample require further investigation. The Rashba coefficient in graded DA sample is also found to be more responsive to the gate voltage. These results are indicative that digital alloying is a promising approach towards engineering the spin-orbit coupling in semiconductor quantum wells.

4.2 Experiment

The samples consisted of a 30 nm $In_{0.81}Ga_{0.19}As$ quantum well with a 120 nm thick $In_{0.75}Al_{0.25}As$ top barrier grown on a metamophic InAlAs virtual substrate on a semi-insulating InP (001) wafers with solid source molecular beam epitaxy in a VG V80H MBE system. The exact details of the growth are given in Chapter 3. The samples consisted of a random alloy QW, a InAs/GaAs DA QW, a InAs/InGaAs DA QW, and a 3% graded InAs/InGaAs DA QW. The InAs/GaAs consisted of a 17 period superlattice of 1 monlayer of InAs and 5 monolayers of GaAs. The nongraded InAs/InGaAs DA QW consisted of a 4 period superlattice of InAs and $In_{0.69}Ga_{0.31}As$. The 3% compositional grading was implemented by varying the relative thickness of InAs and InGaAs but maintaining a total period thickness of 7.5 nm. The exact layer structure is given in Fig. 4.2. In all of the DA QW, the bottom interface of the QW is an InAs/InAlAs, while the top interface of the QW is an (In)GaAs/InAlAs interface.

Hall bars were fabricated to study the electrical transport properties. The Hall bar mesa was etched with wet chemical etching using a mixture of H_2SO_4:H_2O_2:H_2O (1:8:120). Ohmic contacts to the quantum well were formed with NiGeAu contacts annealed at 450 ^oC for 2 minutes. To modulated the carrier density in the Hall bar, a 30 nm AlO_x gate dielectric was deposited with atomic layer deposition followed by a Ti/Au top gate

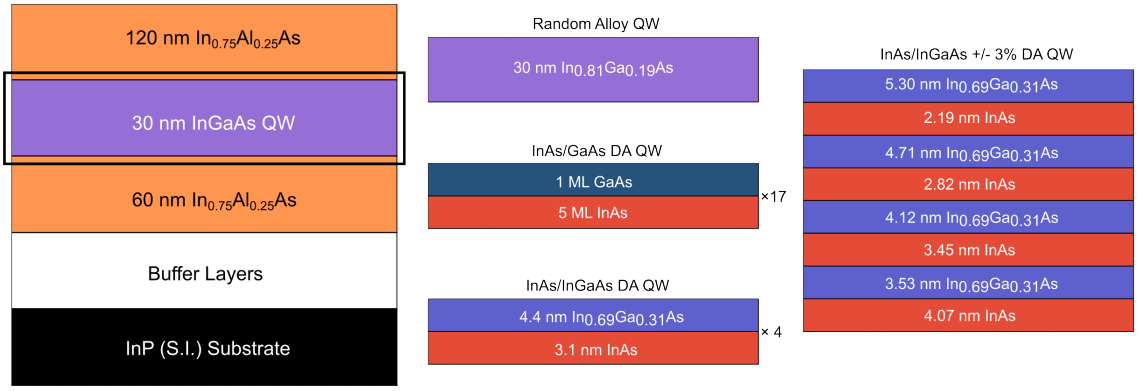


Figure 4.2: Schematic layer structure consisting of a 30 nm InGaAs quantum well buried 120 nm from the surface on the left. Layer structure of the different quantum wells, consisting of a random alloy quantum well, a InAs/GaAs DA quantum well, a InAs/InGaAs DA quantum well, and a 3% graded InAs/InGaAs DA quantum well.

electrode. Fabrication was performed by Y. Gul. The width of the Hall bar was 80 μm, with an arm spacing of 740 μm. The ratio of the Hall bar width to the spacing of the arms was 9.25. The ratio of the Hall bar width to the spacing of the arms was 9.25. Unless stated otherwise, transport measurements were performed at 2 K. Temperature dependent measurements were performed with a modulation field, using the experiment methods described in [61].

4.3 Magnetotransport of a graded InAs/InGaAs DA quantum well

The predicted band structure with $k \cdot p$ and the magnetotransport of the graded InAs/InGaAs DA QW is shown in Fig. 4.3. From the probability density of the 1^{st} electron conduction band subband, the wavefunction of the QW is asymmetric due to the compositional grading implemented by the digital alloying, there are peaks of probability density in the InAs regions of the quantum well and troughs in the InGaAs regions. The magnetotransport of the 3% graded QW shows the integer quantum Hall effect with

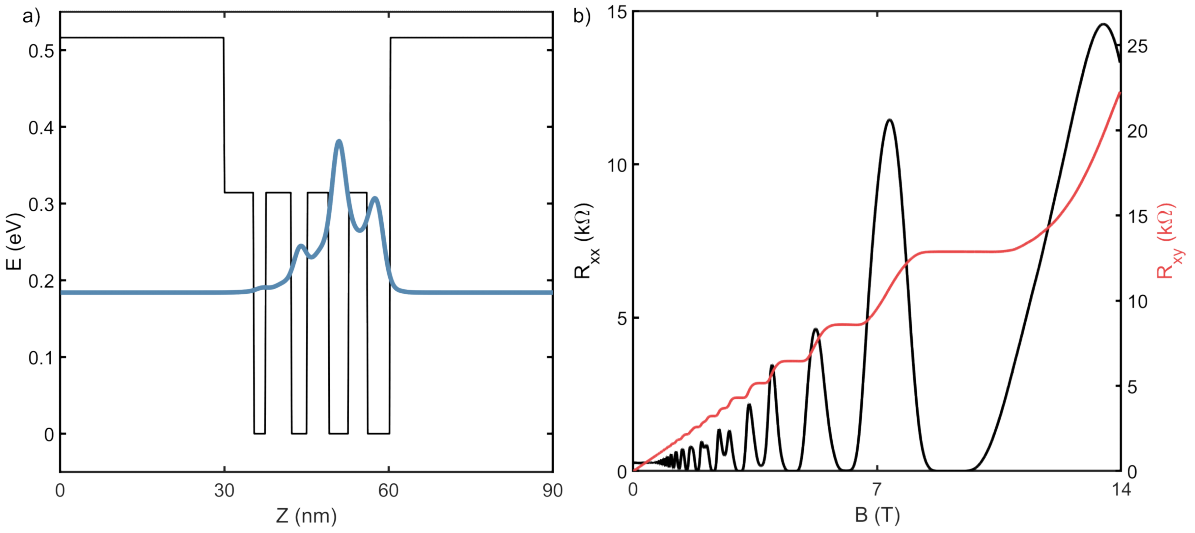


Figure 4.3: a) Band structured of the 3% graded InAs/InGaAs DA QW with the probability density of the 1st electron subband of the quantum well predicted by $k \cdot p$. b) Magnetotransport of the graded InAs/InGaAs DA QW, showing the interger quantum Hall effect with vansishing magnetoresistance.

vanishing magnetoresistance, indicative of a high qualtiy 2DEG without any parallel conduction. The onset of SdH osculations occurs at B = 0.22 T. The integer quantum Hall effect also proves that the DA QW is not a multiple QW. In multiple QWs the IQE gains additional quantization by the number of multiple QWs [72], the lack of additional quantization in the DA samples indicates the sample is not a multiple QW. The magnetotransport of the random alloy QW and the nongraded DA QWs is shown in Chapter 3.

The mobility at different carrier densities was measured by varying the top gate electrode. The mobility of the 3% graded is plotted in Fig. 4.4a. The mobilities of the other samples are plotted for comparison. The mobility of the graded sample is observed to increase as carrier density increases until it reaches a maximum and then begins to decrease due to intersubband scattering once the second subband becomes occupied. The peak mobility of the graded DA QW is 524,000 cm^2/Vs at a carrier density of 4.13×10^{11} cm^{-2}. The lower mobility of this sample compared to the nongraded DA QW

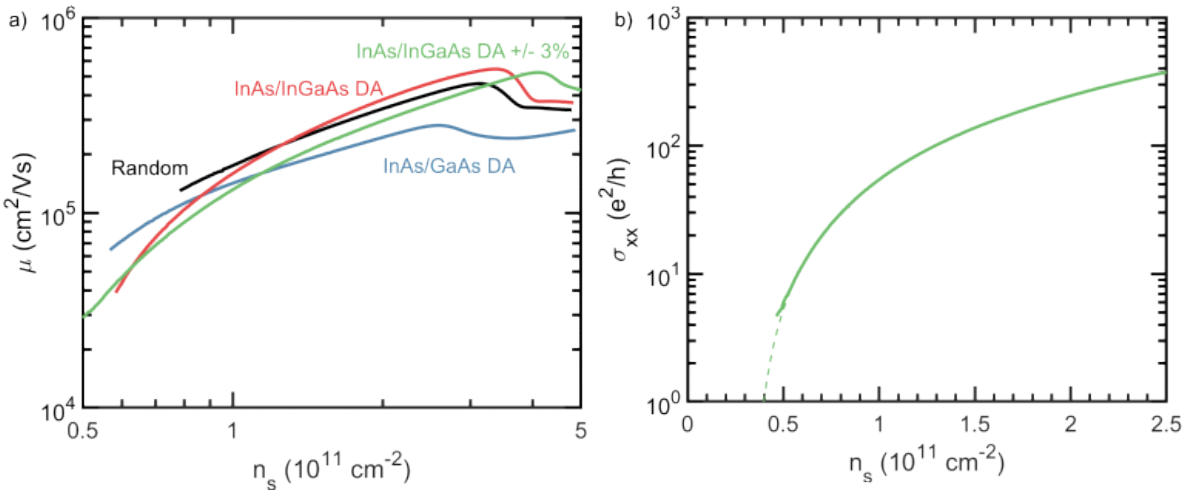


Figure 4.4: a) Mobility as a function of carrier denisty for the 3% graded InAs/InGaAs DA QW, the mobilities of the other samples in this study are plotted for comparison b) Conductivity of the quantum well, showing the metal-insulator transition at low carrier densities.

in these heterostructures is likely due to increased interfacial roughness scattering due to the closer proximity of the peak in the probability density to interfaces, which should increase the effects of interfacial roughness scattering. At low carrier densities the metal-insulator transition is also observed. This transition is observed by the rapid decrease in conductivity of the sample at low carrier density (Fig. 4.4b). The percolation density is extracted from the power law fit to the conductivity, and the percolation density of 3.39×10^{10} cm^{-2} is extracted. This percolation density is similar to that of the InAs/GaAs DA, and is consistent with digital alloying increasing the percolation density.

The effective mass of the 3% graded InAs/InGaAs DA is extracted from fitting the thermal damping of the SdH oscillations to equation 2.27 (Fig. 4.5a-c). The effective mass is determined to be 0.032 ± 0.003 m$_0$. The effective mass is comparable to the effective mass of the rest of the samples. The effective mass can be used to estimate the subband splitting from the peak in the mobility, and this subband splitting is estimated to be 30.9 meV. The subband splitting from $k \cdot p$ is expected to be 32.8 meV. The typical subband splitting for the random and nongraded InAs/InGaAs DA is found to

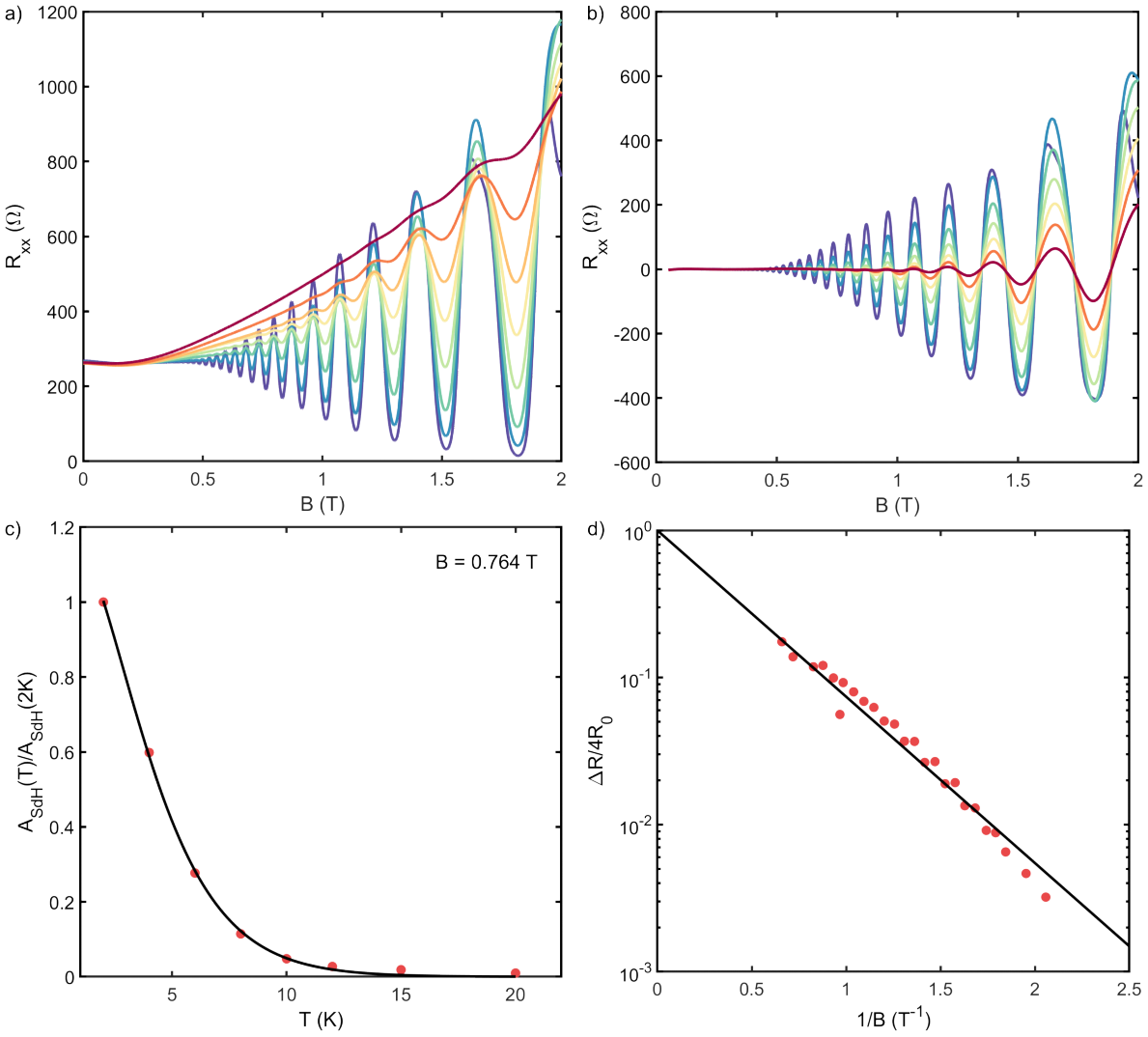


Figure 4.5: a) Temperature dependent magnetoresistance of the % graded DA QW from T = 2 K to T = 20 K. b) Background subtracted temperature dependent magnetoresistance. c) Fitting of the temperature dependence of the magnetoreistance oscillation amplitude for the B = 0.764 T oscillation. d) Dingle plot of the oscillations to extract the quantum lifetime.

be $\approx$ 24 meV. The larger subband splitting for the graded DA is consistent with $k \cdot p$ theory, and may be due to a different confinement potential in the quantum well from the compositional grading.

With this effective mass being known, the amplitude of the resistance oscillations can be normalized to extract the quantum lifetime using equation 2.28. The Dingle plot to extract the quantum lifetime of the graded DA QW is shown in Fig. 4.5d. The quantum lifetime is 0.22 ps, with a τ_t/τ_q of 43.3. The quantum lifetime of the graded DA sample is smaller than the nongraded DA samples, and it is similar to the random alloy quantum well. The increase of the quantum lifetime in DA QW appears to only be in nongraded QW, and the increased interfacial roughness scattering from grading a DA QW appears reduce the quantum lifetime.

4.4 Gate control of spin splitting in a quantum well

Due to the high mobility of the material system, a beating pattern in the magnetoresistance can be observed at low magnetic fields (Fig. 4.6a). In the Fourier transform of the oscillations plotted in 1/B, two peaks in the Fourier transform at similar frequencies can be observed in Fig. 4.6b. Beating patterns in the magnetoresistance can be be due to SdH oscillations of zero magnetic field spin splitting, magnetointersubband scattering (MIS) [110, 111], and magnetophonon resonances (MPR) [112, 113]. MIS generates a frequency in the magnetoresistance that corresponds the difference in frequency (Δf) between the oscillations of two bands. If there is a band with a carrier density such that Δf between the two bands is comparable to the frequency between one of the bands, a beating pattern can be generated due to MIS. The beating patterns generated by MIS and MPR are relatively insensitive to the measurement temperature. It is expected the beating patterns generated by spin-orbit coupling to have a strong temperature dependence,

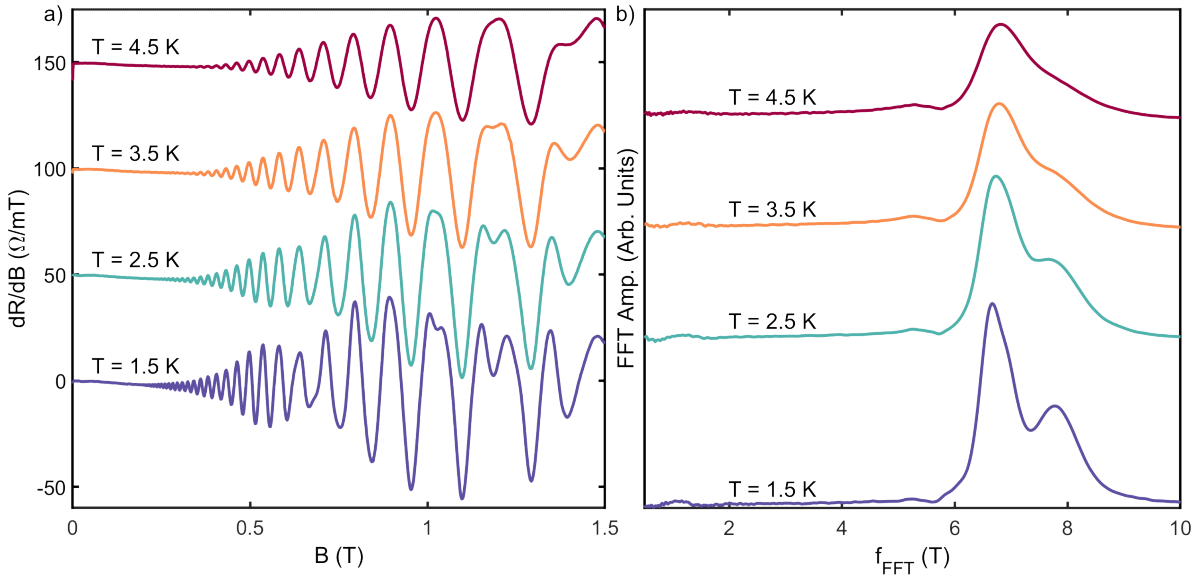


Figure 4.6: a) Temperature dependent dR/dB of the InAs/GaAs DA QW. Meaurements courtesy of I. Villar-Rodreguez. b) FFT of the dR/dB oscillations. At low temperatures a clear peak splitting due to spin orbit-coupling can be observed, at higher temperatures the oscillations thermailze and the peak splitting disappears.

since the beating patterns should possess the same temperature dependence as SdH oscillations. To rule out MIS and MPR the origin of the beating pattern, the temperature dependence of the beating pattern was measured (Fig. 4.6). From the temperature dependence, the beating pattern rapidly disappears with temperature, indicating the origin of this beating pattern is SdH oscillations.

The beating pattern in the low field magnetotransport data is attributed to zero-field splitting of the Fermi surface due to spin-orbit coupling. In the case of linear Rashba and Dresselhaus spin-orbit coupling, the splitting energy is parameterized by: $\Delta_{so} = 2\alpha k_f$, where α is the spin-orbit coupling coefficent and k_f is the Fermi wavevector. Both Rashba and Dresselhaus spin-orbit coupling cause the Fermi surface to split into two spin-split Fermi surfaces. These spin split Fermi-surfaces do not possess the same surface area and thus are occupied by different carrier densities. The different carrier densities of the Fermi surface cause the beating patterns observed in magnetotransport. The dependence of the

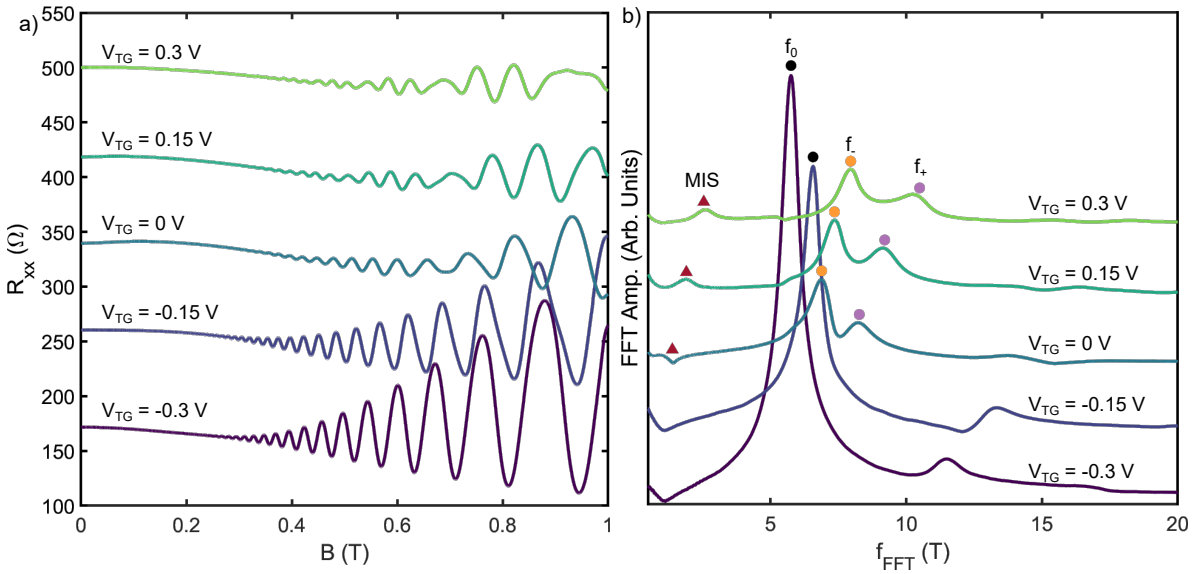


Figure 4.7: a) Gate voltage dependence of the InAs/GaAs DA QW magnetoresistance. A beatting pattern is obsreved at larger gate voltages. b) FFT of the magnetoresistance, showing the peak in the FFT spectra spin split into two peaks at larger gate voltages. A low frequencey MIS peak can be observed once the spin splitting occurs, corresponding to the frequency difference between the spin split peaks.

beating pattern with the applied gate voltage is shown in Fig. 4.7, where the gate voltage dependence of the InAs/GaAs DA QW magnetoresistance and the Fourier analysis of the magnetoresistance is shown. It can be observed that at lower gate voltages, a single SdH oscillation is observed, corresponding to a single peak in the Fourier transform spectra (f_0). As the gate voltage increases, the frequency of the oscillation increases, consistent with the carrier density of the quantum well increasing. Eventually, at larger gate voltages a beating pattern can be observed in the magnetoresistance due to zero-field spin spliting, and the single peak in the Fourier transform is observed to split into two peaks (f_- & f_+). The origin of the onset of spin splitting at larger gate voltages is due to the Rashba effect. At larger gate voltages, the Rashba spin-orbit coupling increases and eventually the spin splitting becomes large enough to be observed as a beating pattern in the magneto resistance and a split peak in the Fourier transform. A low frequency peak now appears, the low frequency difference peak is a MIS peak due to the intersubband

scattering between the spin-split peaks. As the gate voltage increases, the spin split peaks shift to higher frequencies, and the frequency difference between the two spin-split peaks increases.

The change in frequencies and the splitting of the frequencies at different gate voltages for all of the different samples is shown in Fig. 4.8. In all of the samples, a single frequency is initially observed that increases with gate voltage. As the gate voltage increases, the Rashba spin-orbit coupling increases, and eventual the single frequency spin splits and an additional low frequency peak appears due to the difference in frequency between the two spin split bands. The low frequency peak is confirmed to be from MIS, the frequency of the MIS peak is in good agreement with the difference in frequency of the two spin split peak. In all of these samples, gate control over the spin splitting is demonstrated, indicative that the Rashba spin-orbit coupling is the dominant spin-orbit coupling mechanism in these quantum wells.

4.5 Influence of digital alloying on the spin-orbit coupling

The linear spin-orbit coupling parameter can be extracted from the frequencies of the spin splitting. For a spin split band, the frequency can be converted into a carrier density with the following formula $n^{\pm} = ef_{\pm}/h$, where e is the elementary charge and h is the Planck constant. With these frequencies, the linear spin-orbit coupling parameter can now be determined [14]:

$$\alpha = \frac{(n^+ - n^-)\hbar^2}{m^*}\sqrt{\frac{\pi}{2(n^+ + n^-) - 2(n^+ - n^-)}} \tag{4.1}$$

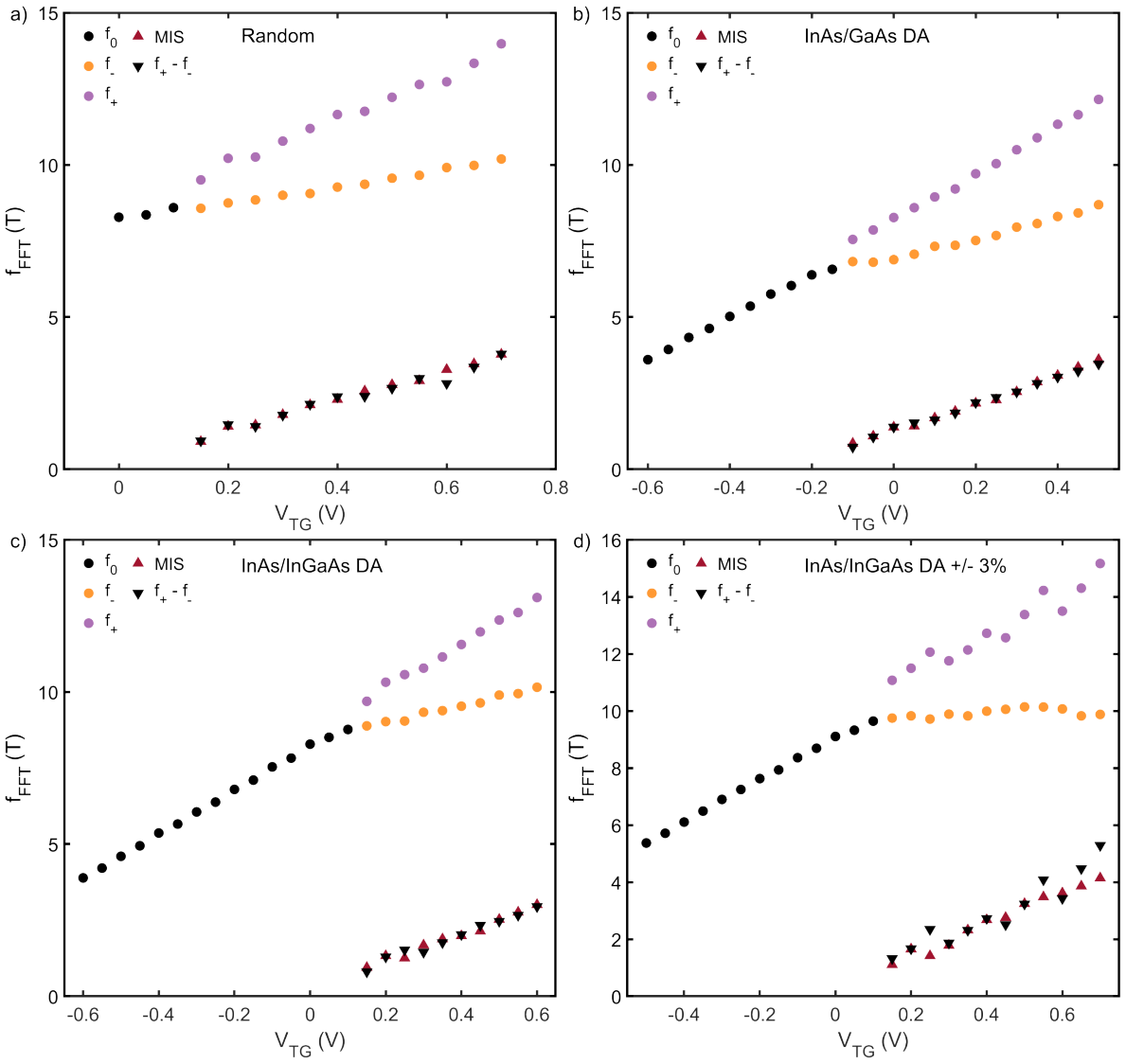


Figure 4.8: Fourier transform spectra frequencies of the a) random alloy QW, b) InAs/GaAs DA QW, c) InAs/InGaAs DA QW, and d) 3% graded InAs/InGaAs DA QW. At lower gate voltages a single frequency (f_0) is observed. At higher gate voltages, this frequency increases. Eventually f_0 spin splits into two frequencies (f_- & f_+). A low frequency peak appears (f_{MIS}) and corresponds to the difference in frequencies between the two spin split peaks (f_+ - f_-).

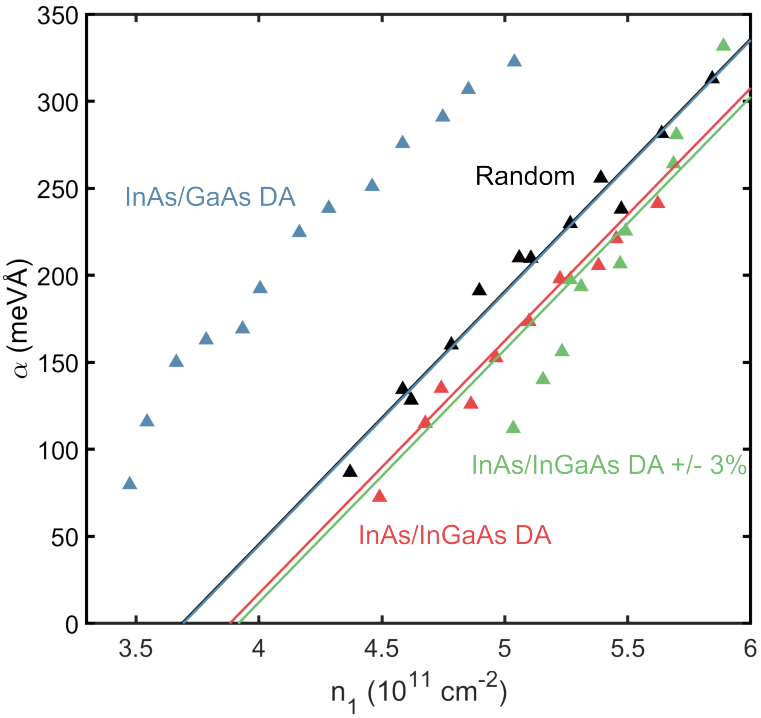


Figure 4.9: SOC parameter at different carrier densities for the different samples. The black line is a linear fit of the SOC parameter to the random alloy QW, with the colored lines offset from the linear fit to the random alloy QW by the predicted interface Rashba SOC contribution.

The SOC parameter at different carrier densities, with the total carrier density determined from SdH oscillations, is shown in Fig. 4.9. The SOC parameter increases with increases to the gate voltage and thus the carrier density. The gate tunability of the SOC parameter is consistent with a change in the SOC parameter due to electric field dependent contribution from Rashba SOC. At lower carrier densities, the random alloy QW SOC parameter is similar what has been previously reported in InGaAs QW [61,62]. The InAs/GaAs DA QW has higher SOC parameter than the random alloy QW, while both of the InAs/InGaAs DA QW samples have a lower SOC parameter than the random alloy QW at most carrier densities. At very high carrier densities, the SOC parameter of the 3% graded InAs/InGaAs DA QW exceeds the random alloy QW.

The Rashba SOC parameter (α_R) can be separated into an electric field component

(α_{R_E}) and an interface component (α_{R_i}).

$$\alpha_R = \alpha_{R_E} + \alpha_{R_i} \tag{4.2}$$

The α_{R_i} can be calculated with $k \cdot p$ theory [14, 15], using the equation 1.8. The α_{R_i} exhibits dependence on the electric field within the samples due to the increased asymmetry of the wavefunction induced by larger electric fields. Both of the nongraded DA QW have similar slopes to the change of the SOC parameter with carrier density as the random alloy QW, and their dependence appears to be offset from the dependence of the SOC parameter with carrier density of the random alloy QW. The InAs/InGaAs DA QW has a 20 meVÅ smaller SOC parameter, while the InAs/GaAs DA QW has a 138 meVÅ larger SOC parameter. The similar slopes are indicative that the change in the Rashba SOC due to the electric field from the gate is the same, but the nongraded DA QW have a different zero electric field α_{R_i}. However, the 3% graded InAs/InGaAs DA QW appears to have much steeper slope, and the SOC parameter appears to change more rapidly with changes in carrier density. The steeper slope is likely due to the α_{R_i} having a stronger electric field dependence from the greater asymmetry in the wavefunction due to compositional grading.

The linear fit to the random alloy QW SOC parameter was offset by the calculated difference in α_{R_i} between the DA QW and the random alloy QW, shown in Fig. 4.9. The α_{R_i} was calculated using equation 1.8. There is good agreement between the measured SOC parameter of the nongraded InAs/InGaAs DA QW and the fit to the random alloy QW SOC parameter offset by the zero electric field α_{R_i}, which is indicative that the difference is due to the interface contribution to Rashba effect. The compositional grading in the 3% graded InAs/InGaAs DA QW induces a larger change in the predicted α_{R_i}, and the larger decrease in observed in the SOC parameter of this sample at lower

carrier densities qualitatively agrees with this prediction. The overall decrease in the total SOC of the graded and nongraded InAs/InGaAs DA QW can be explained as being due the direction of the change in Rashba SOC induced from the digital alloying being opposite to the direction of the Rashba SOC induced from the gate electrode. As a result, there is a net decrease in the total SOC of the InAs/InGaAs DA QW. If the quantum well heterostructure were to be inverted, with the bottom interface with the barrier being InGaAs and the top interface with the barrier being InAs, it is expected that the directions of the interface and electric field effects to align, and a overall enhancement of the total spin-orbit coupling to be observed. However, this experiment has yet to be performed. These results show that the changes in the spin-orbit coupling can be qualitatively explained by the interface contribution to the Rashba effect. However, both the direction and the larger magnitude of the change in SOC in the InAs/GaAs DA QW cannot be explained with $k \cdot p$ theory, and this change likely requires further theoretical investigation to understand.

4.6 Summary

In summary, digital alloying was demonstrated to significantly modify the SOC of the quantum wells in InGaAs quantum wells. Gate control of the SOC in the quantum wells was observed for the random alloy and the digital alloy quantum wells. Changes up to 138 meVÅ of the SOC parameter were observed, with the largest changes in the InAs/GaAs DA QW. Nongraded DA QW were observed to have similar changes in SOC parameter with gate voltage, but are offset from each other. The changes in the nongraded DA samples can be qualitatively understood as being due to changes in the Rashba parameter induced from differences at the interfaces. The compositionally graded DA QW demonstrated stronger gate tunability of the SOC in the quantum well, which is likely

due to the increased asymmetry of the quantum well from the compositional grading. Further theoretical investigation is required to quantitatively explain the changes in the SOC. These results establish digital alloying as an effective method of modifying the SOC of quantum wells.

4.7 Acknowledgements

The growth of the quantum wells was supported by University of California Multiple Campus Award No. 00023195. Transport experiments were supported by the Department of Energy under award No. DE-SC0019274. The use of the Nanotech UCSB Nanofabrication Facility is acknowledged.

Chapter 5

Fermi-level pinning in InSb surfaces

5.1 Fermi-level pinning in semiconductor surfaces

The breaking of translational symmetry at a surface or interface of a crystal allows evanescent waves to exist within the gap of a semiconductor, generating surface states [114]. Semiconductor surface states have a strong influence on the properties of semiconductor devices. At sufficiently high surface state densities, these surface states can pin the Fermi-level of a semiconductor surface near the charge neutrality level, regardless of the semiconductor's bulk Fermi-level position and inhibit the control of the Schottky barrier height of the metal-semiconductor interface [115]. The Fermi-level pinning due to surface states is shown schematically in Fig. 5.1. Additionally, semiconductor surface states can serve as a source of surface recombination, which can negatively impact device performance [116].

InSb is a III-V zincblende semiconductor with a small ($\sim$0.2 eV) band gap and a high ($\sim 80,000$ $cm^2V^{-1}s^{-1}$) room temperature electron mobility [117]. The small band gap of InSb has enabled the use of InSb for infrared detection [118, 119]. InSb has been explored as a material for high-speed and low power transistors due to its high electron

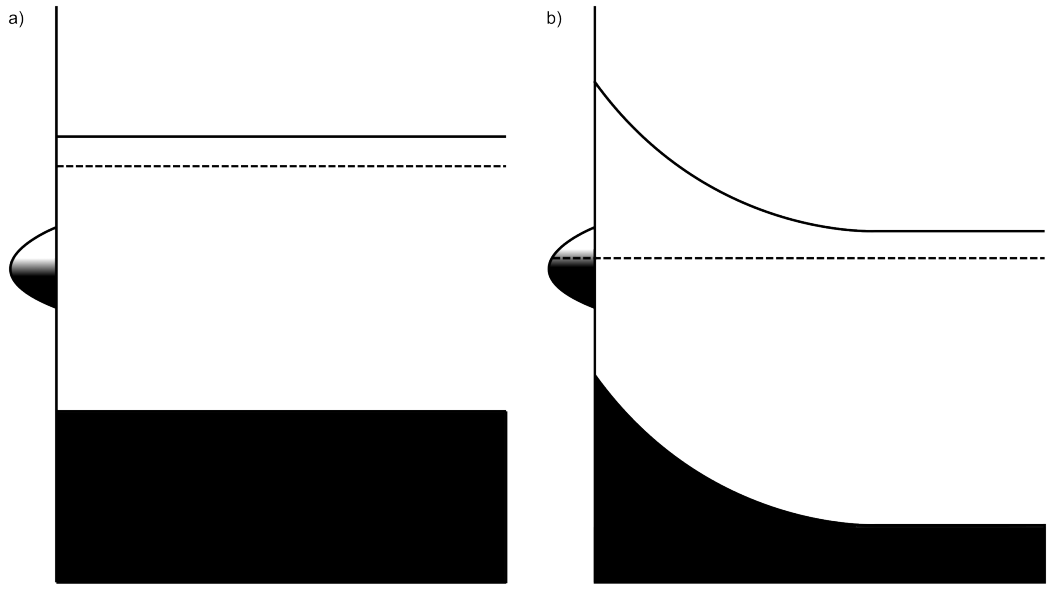


Figure 5.1: a) Schematic nonequilibrium condition of a n-type semiconductor with a surface that posses a surface state distribution with a charge neutrality level in the middle of the band gap. b) Equilibrium condition of the surface band bending, with the surface Fermi-level pinned near the charge neutrality point.

mobility [120–122]. Recently, InSb has attracted interest as a candidate material for terahertz electronics [123,124], and as a building block for topological quantum computers due to its strong spin-orbit coupling [125,126]. In the application of topological quantum compuing, the Fermi-level pinning of InSb is an especially important parameter. In the proposals for implementing InSb in topological quantum computing, InSb is interfaced with superconductors to form hybrid semiconductor/superconductor heterostructures. The Fermi-level pinning is predicted to influence the degree of hybridization between the two materials and thus the properties of these heterostructures [127]. In addition, the Fermi-level pinning position is expected to influence the Rashba spin-orbit coupling of these devices. To better engineer InSb based devices, understanding the surface electronic properties of InSb is essential. In particular, the electronic properties of the (001), (110), and (111) surfaces of InSb are of particular importance, these surfaces are the most commonly utilized surfaces for current and future InSb devices.

While many of the clean InSb surfaces have been imaged with STM [128–140], there have been only a few studies on the surface electronic structure of InSb with STS [135,140, 141]. Most STS studies of InSb have been on the cleaved (110) (1x1) surface [135, 141], which have demonstrated the cleaved surface can be unpinned and devoid of surface states within the semiconductor band gap. In this work, the electronic structure of InSb (001), (110), and (111)B wafers prepared by molecular beam epitaxy and atomic hydrogen cleaned is studied by low temperature STM/S. The findings yield further insights into the nature of InSb surfaces.

5.2 Experiment

5.2.1 Sample preparation

Unintentionally doped InSb (001), (110), and (111)B wafers (Wafer Technology Ltd.) were used as the substrates for this study. The InSb wafers had an unintentional n-type doping of $\sim 1 \times 10^{14}$ cm^{-3}. After loading into the vacuum chamber, the native oxide of the InSb wafers was removed with *in-situ* atomic hydrogen cleaning. To hydrogen clean the samples, the samples were heated to 380 °C, as measured by a thermocouple near the sample, and exposed to a chamber pressure of 5×10^{-6} Torr of atomic hydrogen, as measured by an ion gauge on the chamber. The atomic hydrogen was generated by flowing hydrogen gas through a leak valve and into a thermal cracker (Dr. Eberl MBE-Komponenten GmbH), which was operated at a temperature of 1700°C. The temperature window for correct hydrogen cleaning was found to be narrow for InSb substrates. With a pressure of 5×10^{-6} Torr of atomic hydrogen, the temperature window for correct hydrogen cleaning was found to be approximately 20 °C. If the samples were cleaned at hotter temperatures, excess In would form and metal droplets on the InSb begins to be

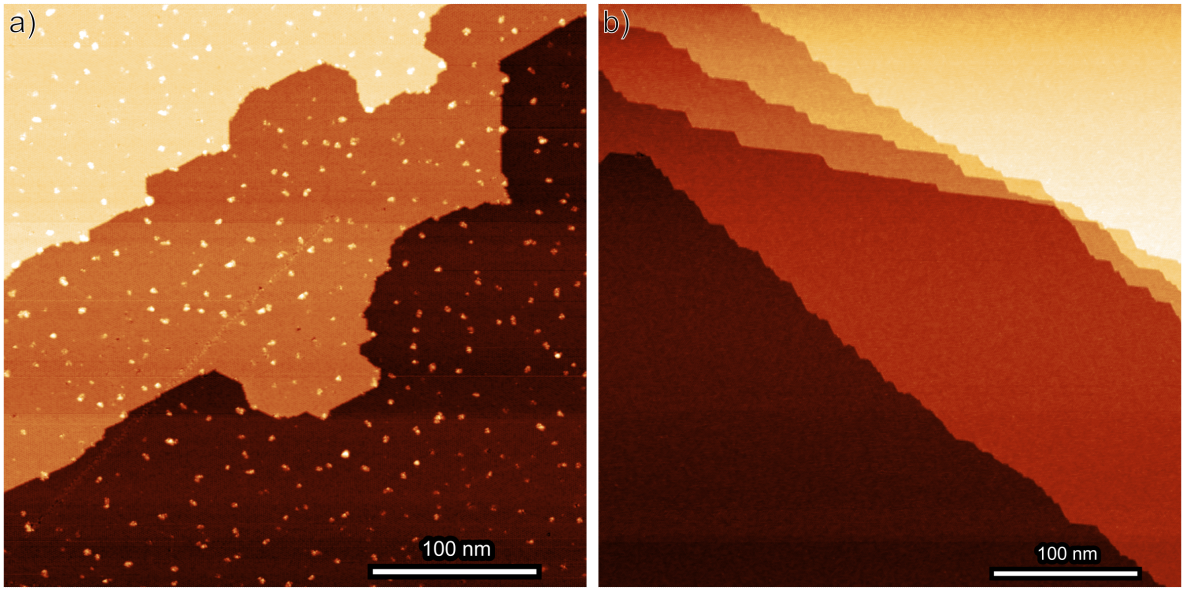


Figure 5.2: a) STM image of InSb (111)B cleaned at low temperatures, brights spots due to residual surface oxide are visible (I_T = 5 pA, V_B = 3 V). b) STM image of a 10 nm thick InSb epilayer on a InSb (111)B substrate, step bunching is visible (I_T = 5 pA, V_B = 3 V).

observed. If the sample is cleaned at cooler temperatures, the surface oxide is not fully removed, and patches of oxide on the surface can be observed in STM, as seen as the bright spots on the monolayer terraces in the STM image of the InSb (111)B surface after hydrogen cleaning in Fig. 5.2a. It is found that upon increasing the pressure of atomic hydrogen to 5×10^{-5} Torr, the temperature required for removal of the surface oxide could decrease to below 300 °C. Higher pressure hydrogen cleaning appears to widen the temperature window for hydrgoen cleanning and enable lower temperature hydrogen cleaning. The hydrogen cleaning step resulted in the c(8x2), (1x1), and (3x3) surface reconstructions for the (001), (110), and (111)B surfaces, respectively.

To obtain different surface reconstructions, the samples were transferred *in-situ* into a molecular beam epitaxy chamber with a base pressure $< 1 \times 10^{-10}$ Torr, where a 20 - 100 nm thick unintentionally doped InSb layer was grown at 360 - 400 °C. Defects such as step edge pinning was observed in the growth of homoepitaxial InSb thin films on the

(111)B surface, shown in Fig 5.2b. Defects such as step bunching, hillocks, and rotational twinning are common during the growth of (111)B III-V surfaces [43,142,143]. To prevent excessive defect formation in the thin film, the thickness of the thin film on the InSb (111) B was limited to 20 nm. The final surface reconstruction was determined by annealing the surface at different Sb overpressures and monitoring the surface reconstruction with reflection high energy electron diffraction.

5.2.2 STM/S measurements

After surface preparation, the samples were rapidly cooled and then transferred *in-situ* into a STM. *In-situ* scanning tunneling microscopy was performed with an Omicron Low Temperature STM at 4.6 K or 77 K with a base pressure $< 4 \times 10^{-11}$ Torr. Electrochemically etched tungsten tips or mechanically cut PtIr tips were used for the STM experiments. The native oxide on the tungsten tips was removed with electron beam heating. All tips were characterized on gold prior to the STM experiments. Scanning tunneling spectroscopy was performed at constant tip height. The dI/dV was measured with a lock-in amplifier, with an AC modulation frequency of $\sim$ 1 kHz and modulation voltage of 5-10 mV. To ensure the spectra presented in this study are representative of the surface electronic properties, the spectra of each surface presented in this study are the average of at least 50 different individual spectra taken at different spatial positions on the surface.

Ensuring the STM tip is free of contamints is essential for accurate measurements of the local density of states of the sample surface from a STS spectra. The I-V curve of a STS spectra on gold should be linear, with the dI/dV being featureless. During STM/S measurements the tip can be contaminated with InSb or an insulating surface contaminant such as an oxide. If this happens, then the measured dI/dV will demon-

strate features from the contaminant from the tip, typically resulting in features such as anomalously large energy gaps or unusual peaks in the STS spectra. These effects can be screen by checking the STM tip with gold. If the STM tip is contaminated, it is recommended that the tip is dipped into gold to displace or bury the contaminate or the tip is field emission cleaned. The details of field emission cleaning are give in Appendix E. It was found that scanning with large positive biases between the tip and the sample helps prevent the STM tip from picking up InSb or Sb on the tip. All of the STS spectra shown in this study use a positive bias of either 1.5 - 2 V and a current of $\sim$ 1 nA to settle the tip prior to acquiring the STS spectra.

5.3 (001) Surface

A filled states STM topographic image of the (001) centered (8x2) surface is shown in Fig. 5.3(a). This centered (8x2) surface, or c(8x2) surface reconstruction, is an In rich surface of the InSb (001) surface [144]. Visible in the STM image are Sb dimers. Columns composed of two Sb dimers are present. The c(8x2) surface is composed of pairs of Sb dimers separated by rows of In atoms. The surface reconstruction unit cell is outlined in blue. A ball and stick model [131] of the c(8x2) surface reconstruction is shown in Fig. 5.3(b) with the unit cell outlined in blue. The STM images of the c(8x2) surface are consistent with prior studies of the c(8x2) surface [129–134]. Additionally, round defects are present in the STM image. These defects are domain boundaries in the surface reconstruction. The domain boundaries are formed when different domains of Sb dimer stacking intersect. These domain boundaries are observed at low temperatures and are discussed at length elsewhere [130].

Fig. 5.3(c) shows a empty states STM topographic image of the (001) asymmetric (1x3) surface, or a(1x3) surface. The a(1x3) is a Sb-rich InSb(001) surface reconstruction

[144]. The surface has a "wormlike" morphology with bright dots on top of the "worms". The "wormlike" chains are disordered rows of Sb atoms. The bright dots on top of the chains are likely excess Sb clusters on the surface. This observed surface morphology is similar to other reports on the InSb a(1x3) surface [129, 132]. It was proposed that the a(1x3) surface reconstruction is (2x4) surface reconstruction composed of different polymorphs of the (2x4) surface reconstruction [144]. However, an atomic model of the a(1x3) surface has yet to be directly confirmed by STM.

The dI/dV spectra, or STS spectra, of the InSb (001) c(8x2) and a(1x3) surfaces is shown in Fig. 5.3(d). Two a(1x3) surface where prepared with low and high Sb. The low Sb a(1x3) surface was prepared by supplying enough Sb to change the surface reconstruction from the c(8x2) to the a(1x3). The high Sb a(1x3) surface was prepared by supplying additional Sb beyond what was supplied to obtain the a(1x3) surface. The spectra are vertically offset for clarity. The spectra of the c(8x2) surface reconstruction is shown in blue. This spectra is devoid of subgap states and the valence band edge is 36 ± 25 meV below the Fermi-level (0V). The conduction band edge is 213 ± 25 meV above the Fermi-level. The band gap energy is determined by subtracting the valence band edge energy from the conduction band edge energy. The measured band gap is 249 ± 35 meV for the c(8x2) surface, which is in good agreement with the expected low temperature band gap of 240 meV [146]. The good agreement between the measured band gaps and the expected band gaps is indicative of no significant tip induced band bending, and thus the voltage in the STS spectra can be directly interpreted as the energy, eV. All STS spectra presented in this report have measured band gaps of InSb that are in good agreement with the low temperature band gap of InSb. The spectra of the low Sb a(1x3) surface is shown in green, the valence band edge is 74 ± 25 meV below the Fermi-level and the conduction band edge is 197 ± 25 meV above the Fermi-level. A subgap state at 126 ± 25 meV is present in the a(1x3) low Sb spectra, this state is potentially from

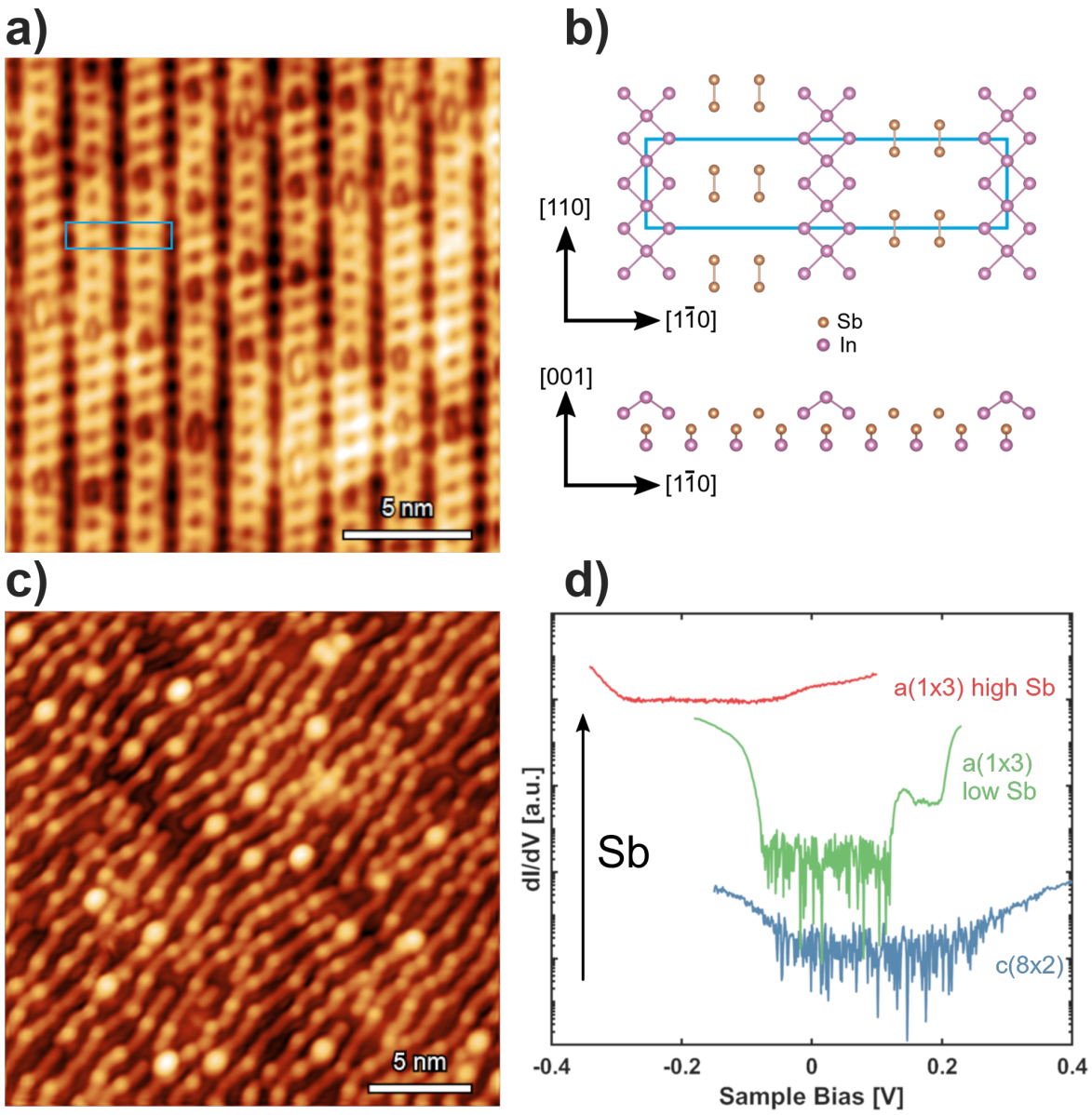


Figure 5.3: STM/S of the InSb (001) surface. (a) Filled state STM image of the In rich c(8x2) surface reconstruction (V = -0.7 V, I = 1 nA). Surface reconstruction unit cell is outlined with a blue box. The bright spots in the image are Sb dimers, and the round defects are domain boundaries in the surface reconstruction. (b) top and side view of the atomic model of the c(8x2) surface reconstruction. Atomic model based on the model as described in Ref. [131]. The surface reconstruction unit cell of the atomic model is outlined in blue. (c) Empty state STM image of the Sb rich a(1x3) surface reconstruction (V = 1.0 V, I = 200 pA). The lines are chains of Sb atoms and the larger dots on the sample are likely excess Sb. (d) STS spectra of In rich c(8x2) surface, a(1x3) surface with low Sb, and a(1x3) surface with high Sb. Spectra plotted on a semi-log scale and vertically offset. Reproduced with permission from [145].

the excess Sb on the surface. Surface Sb islands are reported to posses states within the band gap of III-V semiconductors [147]. The spectra of the high Sb a(1x3) surface is shown in red, the valence band edge is 290 ± 25 meV below the Fermi-level and the conduction band edge is 63 ± 25 meV below the Fermi-level, indicating the surface is in electron accumulation. There are no surface states within the band gap of the high Sb-rich a(1x3) surface. However, relatively large conductance is observed throughout the gap of a(1x3) high Sb spectra. This high conductance is likely due to the electron accumulation layer induced at this surface. The induced conductance within the gap of a semiconductor due to an accumulation layer is discussion at length in elsewhere [148]. Through adding additional Sb on the (001) surface of InSb the Fermi-level shifts towards the conduction band by 254 ± 35 meV, relative to the valence band edge. Hence, Sb can be used to tune the surface Fermi-level position from close to the valence band to the conduction band.

5.4 (110) Surface

Fig. 5.4(a) shows an empty state STM image of the (110) (1x1) surface. Visible in the image are the In atoms present on the surface. The In atoms form a rectangular lattice characteristic of the (1x1) surface reconstruction. The surface unit cell is outlined in blue. Fig. 5.4(b) is the atomic model of the InSb (1x1) [135], which is a surface comprised of a rectangular lattice of Sb and In atoms and natively has a 1:1 ratio of Sb:In. Point defects are also present in the STM image of the (1x1) surface. The observed (1x1) STM images are consistent with prior studies of the (1x1) surface [135]. The STS spectra of the (1x1) surface is shown in 5.4(c). The valence band edge is 22 ± 25 meV below the Fermi-level and the conduction band edge 249 ± 25 meV above the Fermi-level. Other STS studies of cleaved InSb (110) (1x1) reveal an unpinned surface [135, 141]. The observed pinning

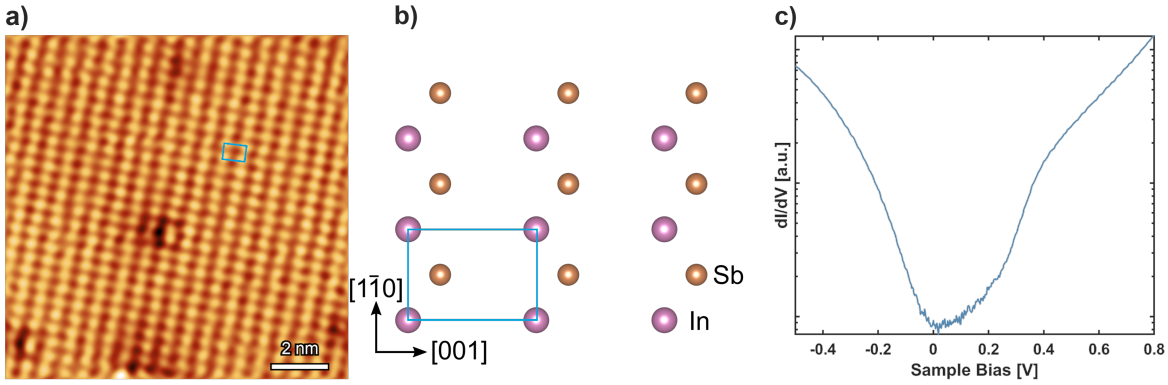


Figure 5.4: STM/S of the InSb(110) (1x1) surface. (a) Atomic resolution empty state image of the (1x1) surface reconstructions (V = 1.5 V, I = 1 nA). The In atoms of the surface reconstruction are imaged. The surface reconstruction unit cell is outlined in blue. (b) Atomic model of the (1x1) surface reconstruction, the surface unit cell is outlined in blue. (c) STS spectra of the (1x1) surface reconstruction. Reproduced with permission from [145].

near the valence band maximum of the (1x1) surface is likely due to a larger number of step edges and point defects being present in the (110) (1x1) surface prepared by atomic hydrogen cleaning. Similar defect induced Fermi-level pinning of the (110) (1x1) surface has been observed before in GaAs [149]. There is a shoulder of states present in the band gap. These states are potentially due to dopant induced conductance, which results in states observed throughout the bandgap of the material due to accumulation within the valence band states, or states due to point defects on the surface. A deeper discussion of the dopant induced conductance states can be found elsewhere [148].

5.5 (111)B Surface

An empty states STM image of the InSb (111)B (2x2) surface is shown in Fig. 5.5(a). A higher resolution scan of the surface is shown in Fig. 5.5(b). Visible in the STM image are the surface trimers and additional spots. The surface reconstruction unit cell is outlined in blue. The (111)B (2x2) surface is a Sb rich surface of InSb(111)B [150]. An

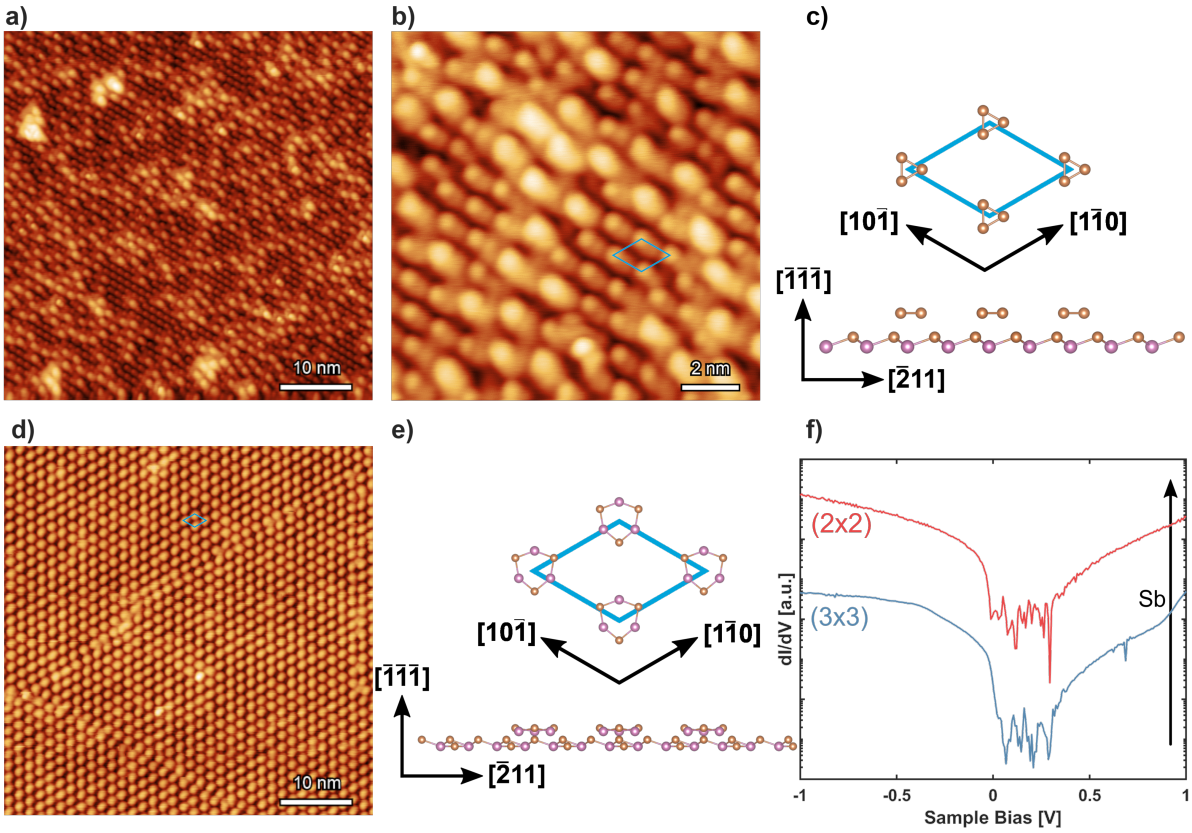


Figure 5.5: (a) Empty state STM image of the InSb(111)B (2x2) surface reconstruction (V = 1.0 V, I = 70 pA). (b) Higher resolution STM image of the (2x2) surface reconstruction, with the surface reconstruction unit cell outlined in blue (V = 1.0 V, I = 70 pA). Sb trimers and larger Sb clusters are visible. (c) Atomic model of the (2x2) surface reconstruction, which is comprised of Sb trimers. Atomic model based on the model as described in [136]. The unit cell is outlined in blue. (d) Empty state STM image of the InSb(111)B (3x3) surface reconstruction (V = 1.0 V, I = 400 pA). Hexamers are visible in this STM image and the surface reconstruction unit cell is outlined in blue. (e) Atomic model of the (3x3) surface [137], the surface is comprised of hexamers, which contain a ring of alternating In and Sb atoms. The unit cell is outlined in blue. (f) STS spectra of the (2x2) and (3x3) surface, spectra are vertically offset. Reproduced with permission from [145].

atomic model of the (2x2) surface [136] is shown in 5.5(c). The surface is composed of Sb trimers which comprise form the main visible features in the STM image. The STM images are consistent with prior STM studies of the InSb(111)B (2x2) surface [136]. The larger spots visible in the image are likely clusters of excesss Sb on the surface. Fig. 5.5(d) shows an empty state STM image of the InSb (111)B (3x3) surface reconstruction. Hexamers are visible in the STM image. The surface reconstruction unit cell is outlined in blue. There are multiply polytypes of the (3x3) surface reconstruction hexamers, with varying In:Sb ratios and shapes [137]. Based on the surface morphology, the particular hexamer polytype observed after hydrogen cleaning is determined to be a buckled ring of alternating Sb and In atoms. This surface nominally has an equal In:Sb ratio. The atomic model of the surface reconstruction [137] is shown in Fig. 5.5(e), with the unit cell outlined in blue. The STS spectra of the (3x3) and (2x2) surface reconstructions is shown in 5.5(f). The spectra are vertically offset for visual clarity, with the red spectra corresponding to the (2x2) suface and the blue spectra corresponding to the (3x3) surface. Both spectra show clearly resolvable band edges and a bandgap devoid of subgap states. The valence band edge of the (2x2) 4 ± 25 meV above the Fermi-level, and the valence band edge of the (3x3) surface is 64 ± 25 meV above the Fermi-level. The conduction band edge of the (2x2) is 275 ± 48 meV above the Fermi-level, and (3x3) surface conduction band edge is 285 ± 25 meV above the Fermi-level. The (3x3) surface is in slight hole accumulation. There is a small 60 ± 35 meV upwards shift of the Fermi-level towards the conduction band upon Sb deposition, relative to the valence band edge.

The InSb(111)B (3x1) surface reconstruction is an In rich surface which has been observed in reflection high energy electron diffraction during thin film growth of InSb(111)B [150]. An empty and filled state image of the same region on (3x1) surface is shown is Fig. 5.6(a) and (b), respectively. From the empty state image two distinct regions are present: a region of the previously observered (3x3) surface reconstruction and a region

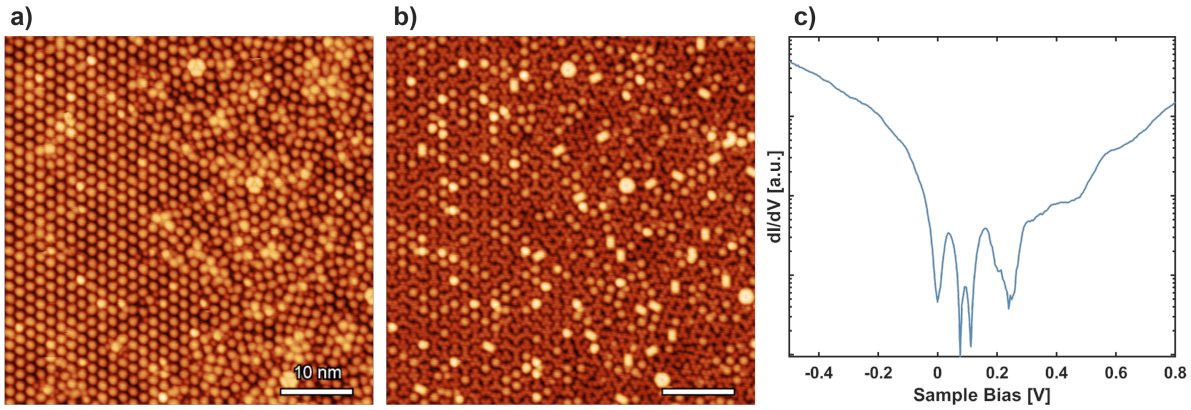


Figure 5.6: (a) Empty state STM image of the InSb(111)B (3x1) surface reconstruction (V = 1.0 V, I = 74 pA). Hexamers are visible on the surface. A region of ordered Hexamers forming a (3x3) reconstruction and a region of disordered hexamers are present. (b) Filled state STM image of the same region, individual Sb atoms of the hexamers are visible (V = -1.0 V, I = 70 pA). (c) STS spectra of the (3x1) surface in an disordered region. Reproduced with permission from [145].

of disordered hexamers. It is apparent that this (3x1) surface is a mixed reconstruction surface composed of ordered and disordered hexamers. Sb atoms of the hexamers are visible in the filled state image of the same region. In this image the three Sb atoms of the (3x3) hexamer are visible and ordered. In the disordered region, the Sb atoms of the hexamer are rotated and often missing Sb atoms. To conclude, the (3x1) surface is a disordered surface comprised of hexamers which are rotated and often contain missing Sb atoms. This (3x1) surface is also a metastable surface, which will eventually convert to the (3x3) surface after annealing. The observed (3x1) surface in this study is very different than a prior study of the (111)B (3x1) surface, which reveals an ordered (3x1) surface reconstruction [138]. This difference is attributed to a difference in surface preparation. The ordered (3x1) surface was prepared by cycles of Ar sputtering and electron beam heating of the sample, and the observed ordered (3x1) is potentially stabilized by the different thermal processing induced from electron beam heating. The STS spectra of the disordered region is shown in Fig. 5.6(c). In this spectra, multiple subgap states

are observed, with the peak energies located at 47 ± 25, 112 ± 25, and 139 ± 25 mV. These surface states likely originate from the dangling bonds created from the missing atoms in the hexamers. The valence band and conduction band edges are located at 15 ± 25 and 246 ± 25 mV above the Fermi-level. For the (3x1) surface, the surface Fermi-level is pinned at the valence band edge.

The valence band edge energies (E_v), conduction band energies (E_c), and band gaps (E_g) of all of the measured surfaces are sumarized in Table 5.1. The band bending profiles of the various surfaces is shown in Fig. 5.7, and the band bending profiles were computed using the method described by *Tan et al.* [3]. The Fermi-level of the In rich and the equal In:Sb surfaces is pinned near the valence band maximum and upwards band bending occurs at the surface. This observed Fermi-level pinning is consistent with previous reports of a charge neutrality level near the valence band and acceptor like surface states [151–154]. Upon deposition of Sb on the (001) and (111)B surface Fermi-level shifts upwards towards the conduction band. In the (001) a(1x3) high Sb surface, downward band bending occurs, and the surface is in electron accumulation. We propose the origin of the upwards shift of the surface Fermi-level upon Sb deposition is electron doping of the surface from Sb clusters, which are present on the Sb rich surfaces. Sb clusters can be semimetallic [155], and can potentially serve as an electron donor on the surface. In comparison to the (001) surface, excess Sb on the (111)B surface does not appear to shift the surface Fermi-level as significantly. The smaller measured Fermi-level shift it potentially due to a higher surface state density on the (111)B surface.

5.6 Summary

The electronic structure of clean InSb (001), (110), and (111)B surfaces was studied with STM/S. We find that the Sb shifts the surface Fermi-level towards the conduction

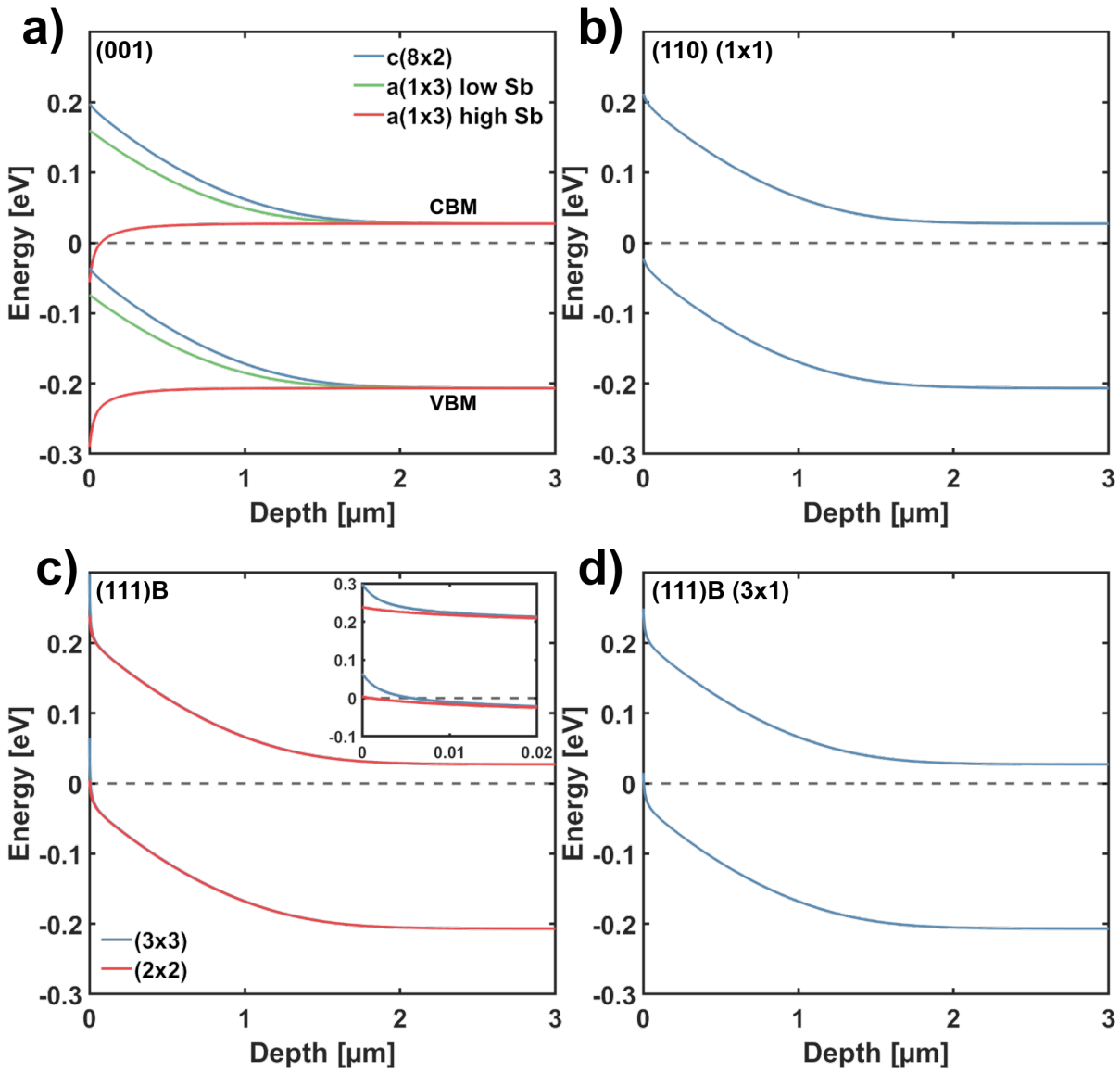


Figure 5.7: Calculated surface band bending profiles of the various InSb surfaces. (a) The profiles for the (001) surfaces. (b) The profile of the (110) (1x1) surface. (c) The profile of the (111)B (2x2) and (3x3) surface, inset is the surface band bending region within 20 nm of the surface. (d) The band bending profile of the (111)B (3x1) surface. Reproduced with permission from [145].

Table 5.1: Valence band edge energy (E_v), conduction band edge energy (E_c), and band gap energy (E_g) of the various InSb surfaces. All band edge energies are with respect to the Fermi-level. Band gap energy is defined as: $E_g = E_c - E_v$.

Surface	E_v (meV)	E_c (meV)	E_g (meV)
(001) c(8x2)	-36 ± 25	213 ± 25	249 ± 35
(001) a(1x3)[1]	-74 ± 25	197 ± 25	271 ± 35
(001) a(1x3)[2]	-290 ± 25	-63 ± 25	227 ± 35
(110) (1x1)	-22 ± 25	249 ± 25	271 ± 35
(111)B (2x2)	4 ± 25	275 ± 48	271 ± 54
(111)B (3x3)	64 ± 25	285 ± 25	221 ± 35
(111)B (3x1)	15 ± 25	256 ± 25	231 ± 35

band on the (001) surface, and Sb exposure to the surface can shift the surface from depletion to electron accumulation. In contrast to the (001) surface, excess Sb on the (111)B surface does not as effectively shift the surface Fermi-level, potentially due to a higher acceptor surface state density. The surface Fermi-level of the In rich and equal In:Sb (001), (110), and (111)B surfaces remains close to the valence band maximum, which is consistent with a charge neutrality level near the valence band maximum. The (111)B (3x1) surface is determined to be a metastable, disordered (3x3) surface with many vacancies. Multiple surface states were present within the band gap of the (3x1) surface. These surface states are attributed to the disorder and the vacancies present in the surface. These findings yield further insights into the Fermi-level pinning of various InSb surfaces and demonstration of Fermi-level tuning of (001) and (111)B surfaces devices via Sb terminated surfaces, thereby enabling further tunability of InSb based devices.

5.7 Acknowledgements

This work was supported by Microsoft Station Q and University of California Multiple Campus Award No. 00023195. Valuable and fruitful discussion with G. W. Winkler, M. Thomas, R. M. Lutchyn, and S. Nadj-Perje are ackowledged.

Chapter 6

Strain solitions in an epitaxial bismuth thin film

6.1 Epitaxial bismuth thin films

Bismuth a trigonal crystal ($R\bar{3}m$) comprised of buckled van der Waals like layers with the normal of the van der Waals like layers oriented in the $< 0001 >$ direction (Fig. 6.1A & B). The c-axis lattice constant is 11.86 Å, and the a-axis lattice constant is 4.547 Å [156]. Bulk bismuth is a semimetal with strong spin-orbit coupling, and has shown evidence of higher order topology [157]. A single van der Waals layer of bismuth is called a bilayer (BL) of bismuth. Bismuthene is a single bilayer of bismuth. As the thickness of a bismuth thin film is reduce, it can underogo a semimetal to semiconductor transition [158]. Bismuthene is predicted to be a QSH insulator. The large spin-orbit coupling of bismuthene is predicted to result in a relatively large topological gap of 200-800 meV [159–162]. This large inverted gap has made Bismuthene a promising material candidate for room temperature QSH devices. The size of the inverted gap is expected to vary significantly with strain, and it is predicted that both tensile strain and compressive

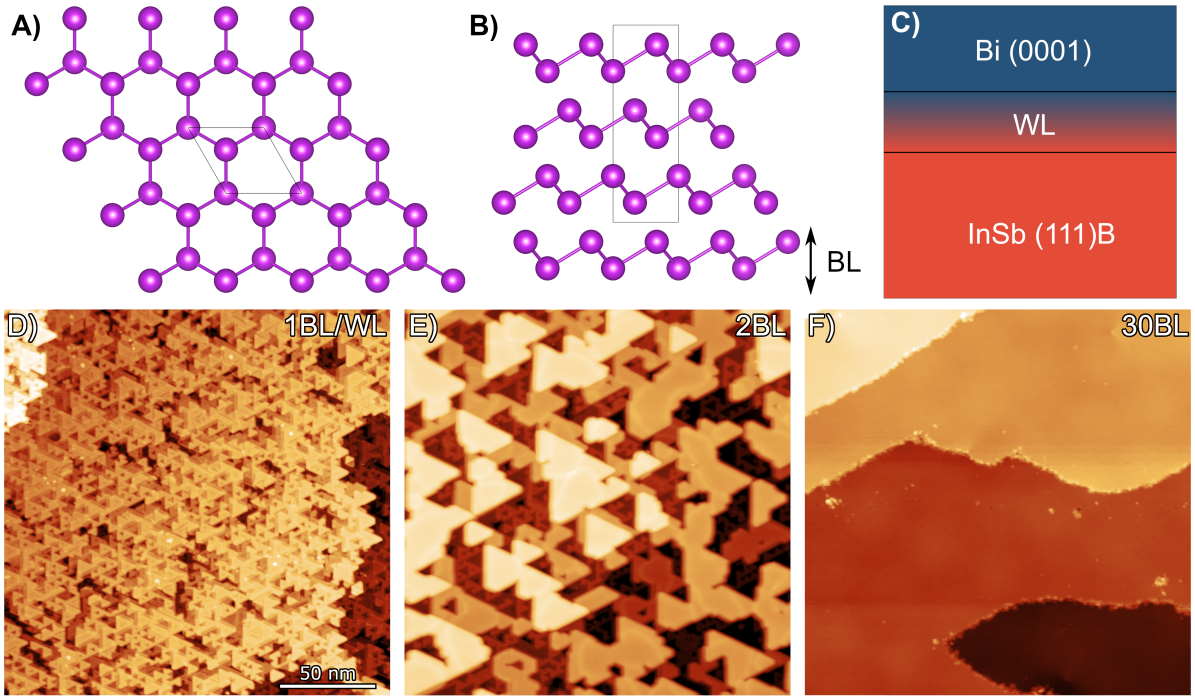


Figure 6.1: A) Top view of an individual bilayer (BL) of bismuth, unit cell of bismuth is outlined. B) Side view of a bismuth BL, with the unit cell outlined. C) Layer schematic, consisting of an InSb (111)B substrate, a wetting layer (WL), and the bismuth (0001) thin film. 200 nm x 200 nm STM height images of: D) the bismuth WL on the InSb surface after deposition of 1 BL of bismuth (I_T = 5 pA, V_B = 3 V, vertical range = 7.5 Å), E) a 2 BL thick film, with bismuth islands growing on the wetting layer (I_T = 5 pA, V_B = 3 V, vertical range = 16 Å), and F) a 30 BL thick film, showing a complete film with 1 BL terraces present (I_T = 5 pA, V_B = 3 V, vertical range = 15 Å). Reproduced under a creative commons license from [164].

strain can enhance the size of the gap [161, 163].

Two-dimensional topological insulators, or quantum spin hall (QSH) insulators, are bulk insulators that possess Dirac-like gapless helical edge states, which carry two spin-polarized currents propagating in opposite directions and has quantized conductance of e^2/h per edge state. The QSH state is induced via band inversion, which typically is generated due to strong spin orbit coupling while preserving time reversal symmetry. These spin polarized helical edge states of QSH insulators have been proposed as potentially useful for both spintronics and quantum computation. The hallmark of the

QSH state is the robust quantized conductance, which is observed via electron transport measurements. Only a select number of materials have demonstrated this property, namely HgTe quantum wells [165], InAs/GaSb bilayers [166], and WTe_2 [167]. The relatively small inverted gap (3 - 50 meV) of the materials has resulted in the QSH effect only being observed at low temperatures. The QSH effect was observed up to 15 K in HgTe, while in WTe_2 it was observed up to 100 K. However, the WTe_2 measurement was observed in exfoliated flakes, which is currently an unscalable process. The typical inverted gap size of the aforementioned materials ranges from a few to tens of meV. The inability to observe the QSH effect at room temperature presents a major challenge for the realization of practical devices based on this effect.

To date, conclusive evidence the QSH state in bismuthene via electron transport remains lacking. Attempts at Bismuthene growth has been predominately on SiC [159], Ag [168], Bi_2Te_3 [169, 170], Si [171], or Ge [172] substrates. Bismuthene growth on SiC subrates remains a challenge since bismuth can nucleate on various sites on the SiC, resulting in grains of bismuthene having the same orientation but different registries growing on the surface. This results in bismuthene thin films which have very high densities of domain boundaries. The domains size of the bismuthene is approximately 10 nm. The high domain density likely leads to significant scattering and thus have poor electron transport behavior [173]. Islands of bismuthene have been grown on substrates such as Ag or Bi_2Te_3. However, these substrates are electrically conductive and as a consequence are unsuitable for electron transport measurements to observe the QSH effect. Attempts at the growth of bismuthene Si and Ge substrates has resulted in thin films of pseudo-cubic allotropes bismuth and not the trigonal bismuthene [172, 174, 175]. Once the bismuth thin films are thicker than approximately 6-10 bilayers of bismuth, this pseudo-cubic like bismuth transforms into the trigonal bismuth. It is proposed that ultrathin pseudo-cubic allotrope is stable on Si and Ge due to weak substrate-

film interactions resulting in free standing bismuth nucleating non-epitaxially and the pseudo-cubic phase being energetically more stable in the few layer regime [174]. So far, the wafer scale growth of single crystalline bismuthene on semiconductor substrates remains elusive and therefore conclusive transport evidence of the QSH state has yet to be performed. The challenge of growing bismuthene motivates the growth of bismuth on different substrates such as III-V substrates.

6.2 Strain solitons

Strain solitons are topological defects in van der Waals materials that act as quasi-dislocations to relieve lattice or rotational mismatch [176] instead of relaxation by dislocation formation observed in non-layered materials. The strain solitons are local regions of the crystal where the atoms have rearranged to relieve elastic strain and the local symmetry is broken. Novel electronic properties such as local band gap modification [177], charge carrier confinement [178], flatbands [179–181], and topological edge modes [182, 183] have been both predicted and observed to occur within the strain solitons. Strain solitons have been experimentally observed in mechanically strained bulk crystals [178], exfoliated graphene layers [176, 179, 182–185], hBN multilayers [186], and twisted transition metal dichalcogenides [177, 187]. However, a wafer scale approach for the generation of strain solitons has yet to be demonstrated. The lack of a wafer scale method to generate strain solitons poses a significant challenge for the utilization of the novel properties of strain solitons in industrial devices. It is therefore desirable for a wafer scale approach for the formation of strain solitons, such as epitaxial growth, as a method to both investigate the properties of strain solitons and as a scalable approach to create functional devices based on strain solitons.

6.3 Experiment

Bi thin films where grown by MBE on unintentionally doped InSb (111)B (Wafer Technology Ltd.) substrates. The substrate surface was cleaned with atomic hydrogen cleaning, see the previous chapter for additional details on the surface preparation, which resulted in the (3×3) surface reconstruction. Thin films were nucleated at 14 °C followed by low temperature annealing at 80-120 °C for several hours to improve the film morphology. All thickness reported in this study are nominal thickness based on the calibration of the growth rate from Rutherford backscattering spectrometry.

In-vacuo STM measurements were performed with an Omicron LT STM at 78 K. Mechanically cut PtIr tips prepared with field emission on Au foil were used for the STM measurements.

6.4 Strain soliton formation in bismuth thin films

In this study, strain solitons in bismuth are generated with heteroepitaxial growth of bismuth on InSb (111)B. Thickness reported are the nominal thickness from the calibrated growth rate. From the bulk lattice constants and the symmetry matching, the InSb (111)B substrate is expected to apply a 0.8% biaxial tensile strain to the bismuth thin film. The layer schematic of the material system is shown in Fig. 6.1C, where the layer structure comprises of the InSb (111)B substrate, a bismuth wetting layer, and the bismuth thin film. The first bilayer (BL) of bismuth deposited on InSb forms a wetting layer comprised of atoms arranged in a Sierpiński triangle like pattern [188] (Fig. 6.1D). Upon subsequent deposition of additional bismuth, islands of (0001) bismuth grow epitaxially on the wetting layer (Fig. 6.1E). While ultrathin bismuth thin films have been observed to grow in the black phosphorous crystal structure [175], the quasi-hexagonal

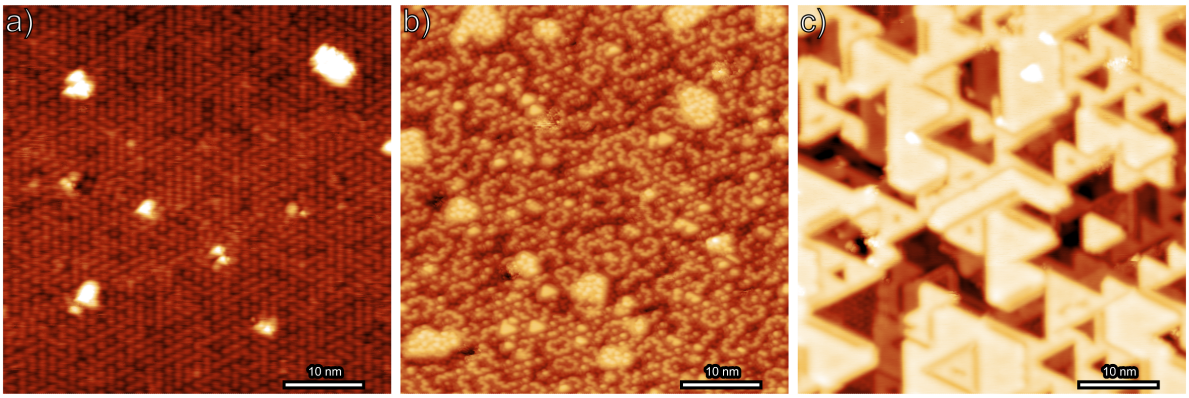


Figure 6.2: 50×50 nm STM images of a) InSb (111)B (3×3) surface reconstruction ($I_T = 5$ pA, $V_B = 3$ V). Bright spots in the image are excess Sb chunks on the surface. b) 0.2 BL of Bi on the InSb (111)B surface ($I_T = 5$ pA, $V_B = 3$ V). c) 1 BL of Bi on the InSb (111)B surface STM image of the Sierpiński triangle wetting layer ($I_T = 5$ pA, $V_B = -1$ V).

bismuth phase is observed to grow in this study for all thicknesses, which likely forms due to the interactions with the substrate. The bismuth islands appear to be oriented in the same direction, which is consistent with the absence of rotational twinning. After additional deposition of bismuth, the islands of bismuth coalesce into a complete, epitaxial single crystal thin film (Fig. 6.1F).

To further understand the formation of the Sierpiński triangle wetting layer, the growth of subbilayer bismuth thin films was studied. In Fig. 6.2, an empty states STM image of the InSb (111)B (3×3) surface reconstruction is shown, with the hexamers of the reconstruction visible and brighter spots due to excess Sb clusters visible. After deposition of 0.2 BL of bismuth on the surface, the bismuth appears to react with the hexamers, and the reaction product appears to the cause the hexamers to start interacting with each other, forming disordered loops and chains. Upon deposition of a 1 BL of bismuth, the bismuth appears to fully react with the surface, creating the wetting layer comprised of Sierpiński triangle triangles. From these measurements, it is clear that the wetting layer forms by reacting with the surface of InSb (111)B and does not form on

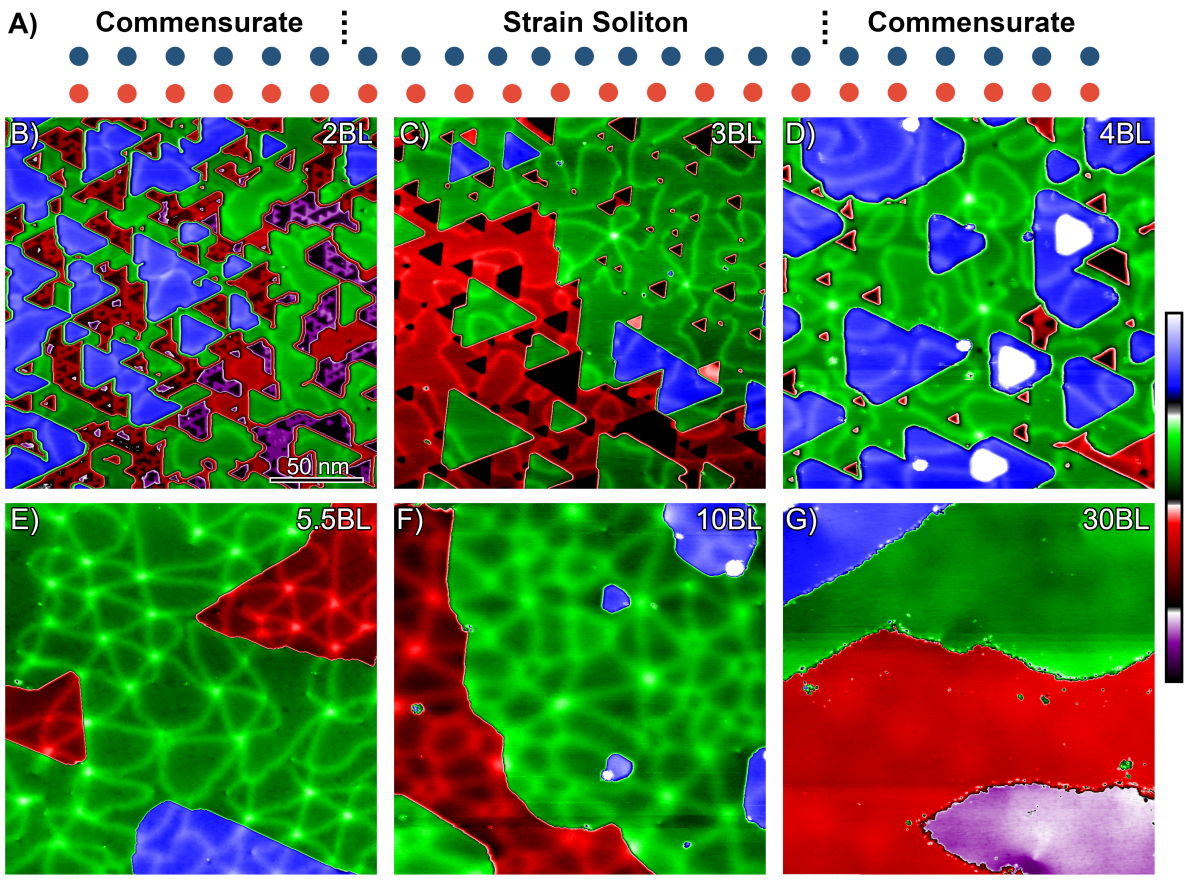


Figure 6.3: A) Schematic of a strain soliton, acting as the domain wall between commensurate regions of the crystal in the thin film (top layer) on the substrate (bottom layer). 200 x 200 nm STM height images of B) 2BL thick film, C) 3 BL thick film, D) 4 BL thick film, E) 5.5 BL thick film, F) 10 BL thick film, and G) 30 BL thick film (I_T = 5 pA, V_B = 3 V). Vertical scale range is 16 Å. Reproduced under a creative commons license from [164].

top of the surface reconstruction.

Strain soliton formation (also termed ripplocations) in the bismuth thin films is due to relaxation of the epitaxial tensile strain from the InSb substrate. The strain solitons are local regions of incommensurate bismuth that are relaxed, these solitons separate commensurate (strained) regions of bismuth (Fig. 6.3A). The relaxation of the bismuth is visible in the STM height images of the bismuth thin films as local regions of brighter contrast, the brighter contrast is predominately an out of plane buckling of the thin film

due to the soliton relaxation, with little electronic state contribution to the contrast. In the 2 BL thick film (Fig. 6.3B), soliton lines can be observed to start and terminate at the edges of the bismuth islands. As the bismuth thin film becomes thicker the soliton morphology can be observed to evolve from predominantly soliton loops in the 3 BL thick film (Fig. 6.3C), to loops and nodes (Fig. 6.3D), and finally to a soliton network (Fig. 6.3E & F). The strain solitons propagate through the different bilayer steps of the bismuth thin film, indicating the strain solitons form at the interface between the bismuth thin film and the wetting layer and propagate throughout the thin film. Upon deposition of the 30 BL of bismuth, no evidence of strain solitons can be observed by STM and the film appears to have completely relaxed (Fig. 6.3G).

6.5 Bending of strain solitons

Analogous to characterization of dislocations, strain solitons can be characterized with the direction of their displacement vector and the direction of propagation [176]. Tensile strain solitons have a displacement vector perpendicular to the direction of propagation, while shear strain solitons have a displacement vector parallel to the direction of propagation. Tensile and shear solitons have different directions of propagation in the crystal. In materials comprised of honeycomb lattices, tensile strain solitons propagate along the zigzag or $< 10\bar{1}0 >$ direction of the crystal while shear solitons propagate along the armchair or $< 11\bar{2}0 >$ direction of the crystal. Under a biaxial tensile strain, it is expected that a regularly spaced network of tensile strain solitons [189, 190]. However, irregularly spaced nodes in the soliton networks are observed in the bismuth. Additionally, the bending of the strain solitons is also visible in the STM images for all thickness in which strain solitons are visible. As a result of this bending, the strain solitons are of tensile, shear, and mixed type in the bismuth thin film.

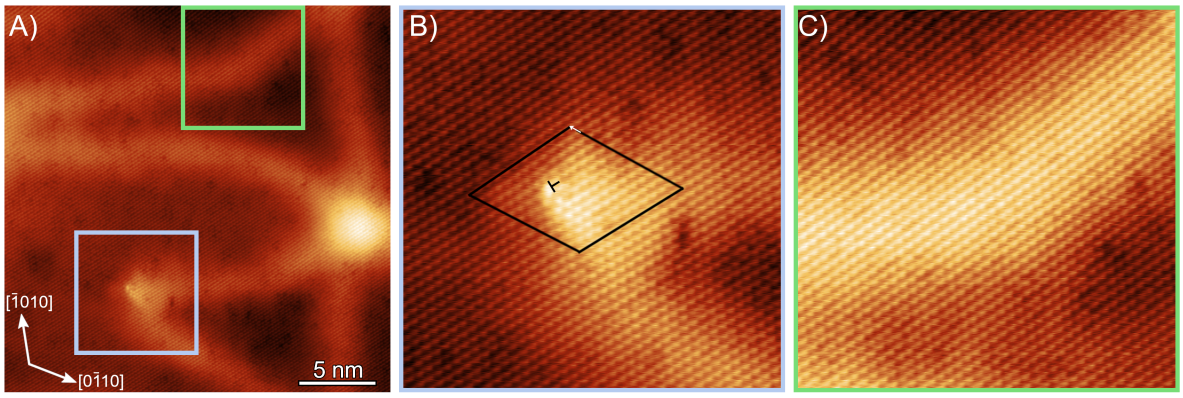


Figure 6.4: A) Atomic resolution height image of 5.5 BL thick film (I_T = 200 pA, V_B = 0.25 V, vertical range = 2.45 Å). B) STM height image of a large angle soliton bend, with an edge dislocation present (I_T = 200 pA, V_B = 0.25 V, vertical range = 1.33 Å). From, the burgers circuit the burgers vector is a[01$\bar{1}$0]. C) STM height image of a small angle (30°) bend, no edge dislocations are present at this bend (I_T = 200 pA, V_B = 0.25 V, vertical range = 1.12 Å). Reproduced under a creative commons license from [164].

To gain further insight into the bending mechanism of the strain solitons, we examine an atomic resolution STM height image of a 5.5 BL thick film where both a large angle bend and a small angle bend in the strain solitons is observed (Fig. 6.4A). Fig. 6.4B and 6.4C are enlargement of the large angle and small angle bends to resolve the atoms, respectively. The large angle bend has a soliton bend angle of 150° with the strain soliton converting from a tensile strain soliton to a shear strain soliton, and a point of brighter contrast can be observed at the bend. This point of brighter contrast is an edge dislocation core. The out of plane edge dislocation has an extra half plane in-plane of the bismuth thin film. From the Burgers circuit, the Burgers vector is a[01$\bar{1}$0], with a being the in plane lattice constant of the bismuth crystal. At the small angle bend of 30°, the strain soliton also converts from a tensile strain soliton to a shear strain soliton. However, at this small angle bend there is no edge dislocation present. The edge dislocations are observed at bends of greater than 30°. This correlation between the large angle bending of solitons and edge dislocations is due to a locally anisotropic strain field favoring the

bending of a strain soliton and the nucleation of an edge dislocation to minimize energy, similar to what has been observed before in uniaxially strain $MoSe_2$ [178].

The bending and edge dislocation formation is indicative that there is inhomogeneous strain relaxation. The inhomogeneous strain is likely induced in the thin films, instead of the expected homogenous, biaxial tensile strain from heteroepitaxial growth. We attribute the local inhomogeneous strain due to interactions between the bismuth and the Sierpiński structure of the wetting layer, observed in Fig. 6.1D, formed from the deposition of the first bilayer of bismuth. Additionally, the change in strain soliton morphology from isolated loops to a soliton network, with the strain solitons becoming predominantly tensile strain solitons as the film thickness increases, is likely due to local interactions with the wetting layer dominate in the thinner films and induce a locally inhomogeneous strain which results in the strain soliton morphology to favor bending and loop formation. However, as the film thickness increases these interactions influence is lessened and the biaxial strain from the substrate favors the formation of a strain soliton network of tensile strain solitons. This process implies that the edge dislocations present within the film will interact and annihilate as the strain solitons convert from bent strains solitons to tensile strain solitons as the film thickness increases.

6.6 Strain mapping of strain solitons

Having now studied the bending of the strain solitons, the strain state of the strain solitons in the bismuth thin film is investigated with strain maps from atomic resolution STM images. Fig. 6.5A shows an atomic resolution height image of a 5.5 BL thick film, where a soliton node is observed along with a tensile strain soliton and a shear strain soliton. Fig. 6.5B is an enlargement of the image around the nodes where the atoms of the bismuth thin film are clearly visible. In the atomic resolution image, only the atoms

in the top layer of the bismuth bilayer are imaged, generating the observed hexagonal lattice of atoms. The in-plane strain from the atomic resolution image is determined from the atomic displacements measured with the Lawler-Fujita algorithm [47], which is a method of determining atomic displacements similar to geometric phase analysis [46]. The Bragg peaks used for the analysis are circled in the Fourier transform of the atomic resolution image shown in Fig. 6.5C. The in-plane strain maps of the strain solitons and node are shown in Fig. 6.5D-F. The x and y directions are defined from the image axes,

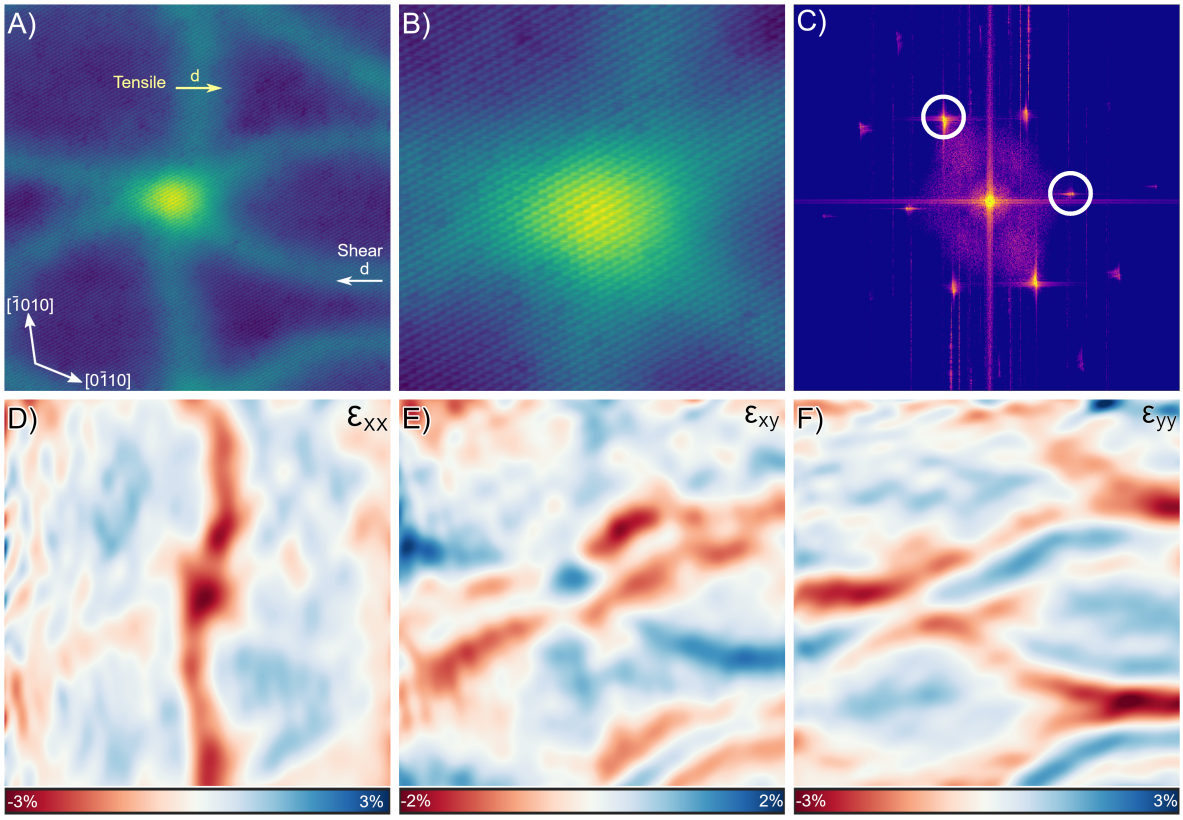


Figure 6.5: A) 43.8 x 43.8 nm atomic resolution height image of a soliton node in a 5.5 BL thick film, both a tensile and a shear strain soliton are present with their corresponding displacement vectors indicated. (I_T = 200 pA, V_B = 0.25 V, vertical range = 2.33 Å). B) Enlargement of the region near the node, atoms are visible. C) FFT of the atomic resolution image, the Bragg peaks used for the strain analysis are circled. Strain maps of the image: D) ϵ_{xx}, E) ϵ_{xy}, and F) ϵ_{yy} with the x and y axes are defined as the image axes. Reproduced under a creative commons license from [164].

which aligns the x direction closely to the $[\bar{1}\bar{1}20]$. From the maps it can be observed that a relaxation of 2.9% ϵ_{xx} tensile strain and 1.3% ϵ_{xy} shear strain is concentrated at the node. Additionally, the tensile strain soliton has the expected relaxation in the direction perpendicular to the direction of propagation, with a maximum relaxation of 1.6% ϵ_{xx}. Finally, it can be observed that within a shear strain soliton there is 1.4% shear strain present and negligible normal strain present. However, it can also be noted that there is tensile strain relaxation in the direction parallel to the direction of propagation, ϵ_{yy}, present in the vicinity of the shear soliton. These results confirm the assignment of strain soliton type based on the direction of soliton propagation. The observed tensile relaxation is consistently larger than 0.8%, which is the expected tensile strain induced from the InSb substrate. This larger than expected relaxation is likely due to the reduction of lattice constant of bismuth in the ultrathin limit [191, 192], resulting in larger strains being induced in the thin film when it is strained to InSb for ultrathin films. The relaxation of 1.6% tensile strain is similar to the tensile strain of 1.5% required for the formation of strain solitons in uniaxially strained MoSe2 [178], the results suggest that relatively large tensile strains may be required before relaxation by strain solitons can occur.

6.7 Scanning tunneling spectroscopy of strain solitons

dI/dV spectroscopy of the 5.5 BL thick bismuth thin film on the strain soliton node is shown Fig. 6.6. The location where the spectra were taken are indicated by the dots in Fig. 6.6A. Significant changes to the dI/dV spectra occur when the measurement is performed on the strain soliton node. Similar to what was observed in the 1D topological

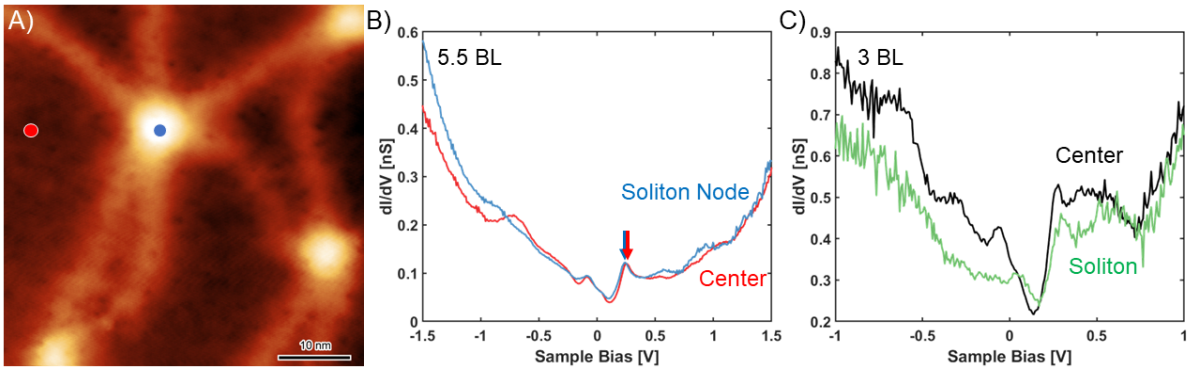


Figure 6.6: A) STM height images of 5.5 BL thick bismuth film ($V_T = 0.2$ V, $I_B = 500$ pA, vertical range = 2.04 Å) and B) STS in middle of region between strain solitons and on the strain soliton node. C) STS of a 3 BL thick bismuth film on the center of a terrace and on a strain soliton. Reproduced under a creative commons license from [164].

edge states in bulk bismuth crystals [193], a small shift in the peak near 0.2 V towards 0V is observed in the strain soliton node. Additionally, a large peak shift occurs near -0.75 V towards more negative voltages is also observed in the strain soliton node. In the STS spectroscopy of a 3 BL thick bismuth thin film on a single strain soliton, a positive shift in energy of the peaks associated with the surface states is observed (Fig. 6.6C). Further investigations with higher resolution are required to understand the changes in the electronic states confined in the strain solitons. These results demonstrate that strain solitons can be used to generate localized electronic states at the wafer scale within bismuth thin films, which is potentially enabling for scalable future bismuth-based devices that require edge state conduction.

6.8 Summary

In summary, the formation of strain solitons in a van der Waals-like material with heteroepitaxial growth is demonstrated. The epitaxial strain enables the formation of strain solitons. The bending of strain solitons is observed, with large angle bends accompanied

by edge dislocations. A change in strain soliton morphology from loops to a network is observed as the film thickness increases. Normal and shear strain is concentrated in the nodes of the strain solitons. These results indicate that the wetting layer induces an inhomogeneous strain state in the bismuth thin film. Changes in the local electronic states are observed in the strain solitons. Our results demonstrate the importance of interface interactions on the morphology of the strain solitons and enables the formation of strain solitons on a wafer-scale, which is an essential step for scalable and functional devices based on strain solitons. Finally, III-V substrates are a potentially promising platform for the growth of ultrathin bismuth thin films. However, more closely lattice matched (111)B substrates such as InAlSb virtual substrates are required to grow epitaxial bismuth thin films without relaxation by strain soliton formation, but the growth of these virtual substrates has yet to be performed.

6.9 Acknowledgements

This work was supported by University of California Multiple Campus Award No. 00023195. We acknowledge the use of shared facilities of the NSF Materials Research Science and Engineering Center (MRSEC) at the University of California Santa Barbara (Grant No. DMR 2308708).

Chapter 7

Summary and future work

7.1 Summary

The investigation of the growth and the properties of thin films with strong spin-orbit coupling grown by molecular beam epitaxy was demonstrated. The properties of the thin films were investigated with electron transport and scanning tunneling microscopy.

7.1.1 InGaAs quantum wells

In InGaAs quantum wells, improving the mobility was accomplished through a combination of MBE growth and low temperature electron transport. The limiting scattering mechanisms was investigated through mobility modeling. Alloy disorder scattering was found to be the mobility limiting mechanism. Digital alloyed quantum wells were investigated as a potential approach towards reducing alloy disorder scattering within the quantum well. The mobility of the quantum wells was further enhanced by digital alloying. With digital alloying, it is found that high quality quantum wells can be grown and the alloy disorder in the quantum wells was reduced by digital alloying. A record breaking low temperature mobility of 545,000 cm^2/Vs was obtained by reducing alloy

disorder scattering through digital alloying. However, it was also found that the mobility of the quantum wells can be significantly reduced by digital alloying if one of the sub-layers of the digital alloy has significant roughness. Design considerations of the digital alloy quantum well for improving the mobility are given.

The spin-orbit coupling of the quantum wells was studied with low field magnetotransport. The spin-orbit coupling was quantified through the analysis of beating patterns due to zero-field spin splitting. Gate control over the spin-orbit coupling was demonstrated in the InGaAs quantum wells. Digital alloying was demonstrated to induce significant changes in the spin-orbit coupling of the quantum well. Digital alloys without compositional grading are found to exhibit similar gate control to the spin-orbit coupling as the random alloy quantum well, but have an offset in the spin-orbit coupling due to the asymmetric interfaces with the barrier layers. Compositional grading by digital alloying was found to increase the gate tunability of the spin-orbit coupling. This work establishes digital alloying as a powerful tool for controlling the spin-orbit coupling in ternary III-V quantum wells.

To understand the effect of digital alloying on the spin-orbit coupling in further detail, it is recommended that digital alloys with inversion of the interfaces are grown and orientation dependent measurements of the spin-orbit coupling are performed. The orientation dependent measurements enable the separation of the Dresselhaus and the Rashba contributions to the spin-orbit coupling, which will enable deeper theoretical investigation of the modifications of the spin-orbit coupling due to digital alloying. When the interfaces are inverted, a flip between increasing and decreasing the total spin-orbit coupling should be observed. This observation would confirm that the interface Rashba spin-orbit coupling effect is the origin of the modifications to the spin-orbit coupling in digital alloys.

The large enhancement of the spin-orbit coupling in the InAs/GaAs digital alloy

cannot be explained with simple $k \cdot p$ theory of the heterostructure. A potential explanation of this enhancement is that the heterostructure does not consistent of planar GaAs layers and instead is comprised of GaAs islands dispersed throughout an InAs matrix. To investigate this potential mechanism, submonolayer superlattices of InAs/GaAs and InAs/InGaAs are suggested to be grown be grown, which should form a digital alloy comprised of submonolayer islands throughout the material.

InGaAs/InAs/InGaAs quantum well trilayers are currently being investigated as one of the most promising platforms for hosting Majorana zero modes. Efforts should be made to incorporate digital alloying into the InGaAs layers of the quantum well to both increase mobility and to increase the spin-orbit coupling of this material system. The mobility is likely enhanced by grading the InGaAs layers such that the probability density of the quantum well is skewed towards the bottom interface and away from the top interface, where scattering from surface states is believed to limit the mobility. Compositional grading could be used to both shift the probably density towards the bottom interface and to potentially increase the spin-orbit coupling of the quantum well with the increased asymmetry. Care needs to be taken of the electric fields within the heterostructure in order to ensure the spin-orbit coupling is enhanced by the digital alloying instead of the total spin-orbit coupling reduced due to the digital alloying. By digital alloying, more conclusive evidence of Majorana zero modes may be possible.

7.1.2 Fermi-level pinning of InSb

Fermi-level pinning of InSb (001), (110), and (111)B surfaces was studied with scanning tunneling microscopy and spectroscopy. In rich surfaces were observed to pin near the valence band maximum. Excess Sb on the surface is found to shift the Fermi-level of the surface towards the conduction band. The measurements are consistent with a

charge neutrality level near the valence band maximum. Electron accumulation on the (001) surface was demonstrated by controlling the Sb content on the surface. The (111)B surface was found to be more strongly pinned than the (001) surface. Further studies of the (111)A Fermi-level pinning are recommended.

The surface preparation dependent Fermi-level pinning of InSb can be potentially exploited in the case of an epitaxial metal or semimetal deposited on InSb such as α-Sn. It is recommended that the surface preparation and surface orientation of the InSb layer be carefully considered and studied to obtain the desired properties of an epitaxial metallic or semimetallic heterostructures on InSb.

7.1.3 Bismuth ultrathin films

The growth of bismuth ultrathin films on InSb (111)B by MBE was investigated with scanning tunneling microscopy. Ultrathin films of bismuth are observed to growth without rotational twinning. The bismuth thin films were found to partially relax immediately on the InSb substrate by strain soliton formation. The strain state of the strain soliton is characterized from atomic resolution images, and unusual behavior of the strain solitons such as strain soliton bending is attributed to the inhomogeneous strain was observed in the strains solitons. These results indicate the importance of the interface interactions on the morphology of bismuth thin films. This is the first report of strain soliton formation by heteroepitaxial growth, which is enabling for the scalable generation of strain solitons. This work indicates III-V substrates are promising platform for the growth of ultrathin bismuth on semiconducting substrates.

Electronic state localization is observed within the strain solitons. However, the nature of these states is currently unknown. Evidence of topological hinge states have been observed to be confined within strain soliton nodes. Measurements at lower temperatures,

such a liquid helium temperatures, with higher resolution are suggested to investigate the nature of these states. In addition, studying the influence of the direction of propagation of the strain soliton on the electronic states within the solitons will be helpful for determining the nature of the electronic states present within the strain solitons.

Future work should focus on studying and engineering the wetting layer to influence the strain soliton behavior. If an ordered wetting layer can be formed, an ordered network of strain solitons could be generated. Ordered soliton networks could potentially generate new electronic states within the bismuth. The morphology of the wetting layer is likely influenced by strong In-Bi interactions. Modifying the quantity of In on the surface could potentially influence the wetting layer morphology. One approach towards modifying the interface is to add additional Sb to the surface and study the morphology of the wetting layer on the InSb (111)B (2×2) surface reconstruction, which is comprised of Sb trimers. Additionally, InSb (111)A substrates could be investigated, where the (2×2) surface reconstruction is a result of In trimers. Finally, one potential approach towards an ordered strain soliton network within the bismuth thin film is to grow a few layer thick Sb layer on the InSb (111)A surface. Sb layers were recently demonstrated to be grown on the InSb (111)A surface with a Moiré pattern [194], and these Sb layers could serve as an interlayer to promote the formation of an ordered strain soliton network and potential Moiré interactions between the Bi and the Sb.

To grow ultrathin bismuth on a semiconducting substrate without strain solitons, a more closely lattice match substrate to bismuth is required. The growth on III-V (111)B surfaces is promising, since the bismuth thin films can be stabilized in the ultrathin limit without twinning in the thin films. InAlSb virtual substrates grown on GaSb (111)B or InSb (111)B is a potential system that can be lattice matched to the bismuth lattice constant. By varing the In:Al content of the InAlSb, the tensile strain of -4.6 - 0.8% could be induced into the bismuth thin film. The bismuth is expected to be lattice matched

to $In_{0.81}Al_{0.19}Sb$. However, an InAlSb virtual substrate with less In may be required for lattice matching due to the bismuth lattice constant potentially reducing in ultrathin films. To perform transport experiments, which are required to observe the quantum spin Hall effect, the InAlSb virtual substrate could be grown on GaSb (111)B substrates. GaSb unintentionally doped substrates can freeze out a low temperatures, eliminating potential parallel conduction from the substrate, and InAlSb (001) virtual substrates have been demonstrated to freeze out at low temperatures as well. STM measurements could be performed with doped InAlSb virtual substrates on doped GaSb wafers.

InAlSb virtual substrates on a (111)B substrate has yet to be reported, and this platform will need to be developed before the growth of bismuth on the InAlSb virtual substrate can begin. Growth on (111)B oriented substrates frequently possess step bunching and twinning, and step bunching can often be prevented in very narrow growth windows [143]. A thorough investigation of the growth window for optimal InAlSb (111)B growth will be required. In addition, the rotational twinning is common during the growth of epilayers on (111)B oriented substrates, and may be prevented through the use of 2° miscut substrates. Miscut substrates promote step flow growh and prevent island growth, and island growth is known to cause rotational twinning during the growth on (111)B oriented substrates [143]. If the density of threading dislocations in the virtual substrates is too high for the growth of high quality bismuth thin films, strained InAlSb/InGaSb superlattices could be implemented to filter the threading dislocations in the metamorphic InAlSb virtual substrate. With this approach, high quality bismuth thin films should be able to be grown on electrically insulating substrates, and it can be determined whether or not bismuth is a quantum spin Hall insulator.

Appendix A

Mobility modeling

The InGaAs quantum well with InAlAs barriers envelope wave function ($\psi(z)$) over the InGaAs thickness L is approximated by:

$$\psi(z) = (\frac{2}{L})^{1/2} sin(\frac{\pi z}{L}) \tag{A.1}$$

for $0 \leq z \leq L$ and 0 for all other z. Only the lowest occupied subband is treated. The mobility is defined as: $\mu = e\tau/m^*$, where e is the elementary charge, τ is the scattering time, and m^* is the effective mass.

From the treatment by Stern and Howard [85] using the Born approximation, the scattering time for a scattering mechanism (i) at a given Fermi wavevector (k_f) is defined as:

$$\frac{\hbar}{\tau_i} = \frac{1}{2\pi\varepsilon_f} \int_0^{2k_f} dq \frac{q^2}{\sqrt{4k_f^2 - q^2}} \frac{\langle |U_i(q)|^2 \rangle}{\epsilon(q)^2} \tag{A.2}$$

where q is the scattering vector, ε_f is the Fermi energy computed using a nonparabolic effective mass, $\hbar$ is the reduced Planck constant, $\langle |U_i(q)|^2 \rangle$ is the averaged scattering potential associated with the particular scattering mechanism, and $\epsilon(q)$ is the dielectric

function from the random phase approximation. The dielectric function is defined as:

$$\epsilon(q) = 1 + \frac{q_{TF}}{q}[1 - G(q)]F_C(q) \tag{A.3}$$

where q_{TF} is the Thomas-Fermi screening wavenumber $q_{TF} = m^* e^2/4\pi\epsilon_L\hbar^2$ with the dielectric constant ϵ_L, $G(q)$ is the generalized form of the local field correction [195], and $F_C(q)$ is the form factor of the Coulomb interaction of the finite width of the quantum well, defined as:

$$F_C(q) = \int_{-\infty}^{+\infty} dz|\psi(z)|^2 \int_{-\infty}^{+\infty} dz'|\psi(z')|^2 exp(-q|z - z'|) \tag{A.4}$$

The scattering potential for interface roughness is [87] of the form:

$$\langle|U_{IR}(q)|^2\rangle = \pi F_{IR}^2 \Delta^2 \Lambda^2 exp(-(q\Lambda)^2/4) \tag{A.5}$$

where Δ is the interfacial roughness, Λ is the correlation length, and F_{IR} is a function that is modified following the treatment by [88] to include the shift of the ground state by a electric field E:

$$F_{IR} = -(\frac{\hbar^2\pi^2}{m^* L^3} + 96(\frac{2}{3\pi})^6 \frac{e^2 m^* L^3 E^2}{\hbar^2}) \tag{A.6}$$

Alloy disorder within the $In_{1-x}Ga_xAs$ quantum well with an alloy disorder potential of dV leads to a scattering potential [89] of:

$$\langle|U_{AD}(q)|^2\rangle = x(1-x)dV^2 \frac{\sqrt{3}\pi a^3}{16} \frac{3L}{2} \tag{A.7}$$

Two-dimensional remote ionized impurities with an charged impurity density of n_j

lead to a scattering potential of the form [86]:

$$\langle |U_{2D}(q)|^2 \rangle = (\frac{2\pi e^2}{\epsilon_L}\frac{1}{q})^2 n_j F_{2D}(q, z_j)^2 \tag{A.8}$$

$F_{2D}(q, z_j)$ is the form factor accounting for the distance between the charged impurity layer and the quantum well:

$$F_{2D}(q, z_j) = \int_{-\infty}^{+\infty} dz |\psi(z)|^2 exp(-q|z - z_j|) \tag{A.9}$$

The scattering potential of homogeneously distributed charged background impurities [86] is:

$$\langle |U_{BI}(q)|^2 \rangle = (\frac{2\pi e^2}{\epsilon_L}\frac{1}{q})^2 N_B L F_{BI}(q) \tag{A.10}$$

where N_B is the background impurity density and $F_BI(q)$ is the form factor for background impurities, defined as:

$$F_{BI}(q) = \frac{1}{L}\int_{-\infty}^{+\infty} dz_j F_{2D}(q, z_j)^2 \tag{A.11}$$

The total scattering time was determined from the individual scattering times and applying Matthiessen's rule:

$$1/\tau = 1/\tau_{IR} + 1/\tau_{AD} + 1/\tau_{2D} + 1/\tau_{BI} \tag{A.12}$$

While analytical expressions for calculating some of the individual scattering times exist, these expression require significant assumptions to be made about the material system. The scattering times in this work were calculated by numerical integration of the various expressions in MATLAB.

Appendix B

MATLAB code of mobility modeling

The following is the MATLAB code used to calculate the mobility of a square quantum well. Some lines of code are split for readability in this document.

```
%% Initialization

clear
close all
fclose('all');
clc

%% Fundamental Constants

q = 1.602e-19;          % Elementary Charge C
h = 6.62607015e-34;     % Planck's Constant J/s
hbar = 1.054571e-34;    % Reduced Planck's Constant Js
Rq = h./q.^2;           % Quantum of Resistance
kB = 1.380649e-23;      % Boltzmann Constant J/K
m0 = 9.1093837015e-31;  % Electron rest mass Kg
ep0 = 8.851878e-12;     % Vacuum permttivity F/m

%% Variable Declarations

% Global variables
global a                    % Lattice constant m 5.98e-10 6.0583
global TBarrier             % Top Barrier Thickness m
global L                    % Quantum well width m
```

```
global el                    % Dielectric constant
global me                    % Effective mass kg 0.03 0.0324
global x                     % Alloy composition
global z2D                   % 2D sheet impurity spacing
global ni2D                  % 2D sheet impurity density m^-2
global p                     % Electric Field polynomial valus, scaled down

%% Material Constants

a = 5.98e-10;                % Lattice constant m 5.98e-10 6.0583
TBarrier = 120e-9;           % Top Barrier Thickness m
L = 30e-9;                   % Quantum well width m
el = 14.723*ep0;              %  relative dielectric constant
x = 0.19;                    % Alloy composition
z2D = TBarrier + L;          % 2D sheet impurity spacing
ni2D = (2e12)*(1e4);         % 2D sheet impurity density m^-2

dV = 0.44*q;                  % Alloy disorder scattering potential J
nw3D = (1.5e15)*(1e6);         % 3D impurity density in well m^-3 ()

nb3D = (5e15)*(1e6);         % 3D impurity density in barrier m^-3

delta = 6e-10;              % Height m
lambda = 13e-9;              % Correlation length m

me = 0.0347*m0;               % Effective mass kg 0.03 0.0324
alpha = 1.955;                % Kane non-parabalicity constant


%% Modeling Mobility Plotting

nvec = logspace(10,12,100)*(1e4);
% Sheet carrier density to integrate over m^-2
fAD = 3/(2*L);                           % Alloy disorder Form factor
ab = (4*pi*el*hbar^2)./(me.*q.^2);       % Effective Bohr radius
astar = (el*hbar^2)./(me.*q.^2);         % 2nd Effective Bohr radius

tic

for i = 1:length(nvec)
nf = nvec(i);                 % Sheet carrier density in the loop
kf = sqrt(2*pi*nf);           % Fermi wavevector m^-1
```

```
vf = hbar*kf/me;              % Fermi velocisty m/s
Ef = q*(sqrt(1+4*alpha*((hbar*kf).^2)./(q*2*me))-1)/(2*alpha);
% Kane Fermi energy J
E = 0;                        % Electric field at this carrier density V/m
rs = sqrt(1/(pi*nf*astar.^2));  % RPA Parameter
q0 = 2/(astar*rs^(2/3));        % Normalizated wavevector for the RPA

funAD = @(j) (x.*(1-x).*(dV^2).*((sqrt(3).*pi.*a.^3)./16).*fAD).*(j.^2)
./(sqrt(4.*kf.^2-j.^2).*((1+((formC2(j,L).*2)/(j*ab))
.*(1-G_LFC(j/q0,rs)).*(1))).^2);
tauAD(i) = integral(funAD,0*kf,2*kf,'ArrayValued',true)/(2*pi*Ef*hbar);
muAD(i) = (1e4)*q./(tauAD(i)*me);     % cm^2/Vs
fun2D = @(j) (((q^2)./(2*(el)*j)).^2).*ni2D.*(form2D(j,z2D,L).^2)
.*(j.^2)./(sqrt(4.*kf.^2-j.^2).*((1+((formC2(j,L).*2)/(j*ab))
.*(1-G_LFC(j/q0,rs)).*(1))).^2);
tau2D(i) = integral(fun2D,0*kf,2*kf,'ArrayValued',true)/(2*pi*Ef*hbar);
mu2D(i) = (1e4)*q./(tau2D(i)*me);     % cm^2/Vs
fun3D = @(j) (((q^2)/(2*(el)*j)).^2).*nb3D.*(form3D(j,L,TBarrier))
.*(j.^2)./(sqrt(4.*kf.^2-j.^2).*((1+((formC2(j,L).*2)/(j*ab))
.*(1-G_LFC(j/q0,rs)).*(1))).^2);
tau3D(i) = 2.*integral(fun3D,0*kf,2*kf,'ArrayValued',true)/(2*pi*Ef*hbar);
mu3D(i) = (1e4)*q./(tau3D(i)*me);  % cm^2/Vs
funBI = @(j) (((q^2)/(2*(el)*j)).^2)
.*nw3D.*L.*(formB(j,L)).*(j.^2)./(sqrt(4.*kf.^2-j.^2)
.*((1+((formC2(j,L).*2)/(j*ab)).*(1-G_LFC(j/q0,rs)).*(1))).^2);
tauBI(i) = integral(funBI,0*kf,2*kf,'ArrayValued',true)/(2*pi*Ef*hbar);
muBI(i) = (1e4)*q./(tauBI(i)*me);     % cm^2/Vs
funIR = @(j) pi.*((((hbar.^2)*(pi.^2)/(me*(L.^3)))+96*((2/(3*pi)).^6)
.*((q.^2)*me*(L^3)*(E^2)./(hbar^2))).^2).*((delta*lambda).^2)
.*(exp(-0.25.*(j*lambda).^2)).*(j.^2)
./(sqrt(4.*kf.^2-j.^2).*((1+((formC2(j,L).*2)/(j*ab))
.*(1-G_LFC(j/q0,rs)).*(1))).^2);
tauIR(i) = integral(funIR,0*kf,2*kf,'ArrayValued',true)/(2*pi*Ef*hbar);
muIR(i) = (1e4)*q./(tauIR(i)*me);      % cm^2/Vs

end

%+96*((2/(3*pi)).^6).*((q.^2)*me*(L^3)*(E^2)./(hbar^2));

tauT = tauAD + tau2D + tauBI + tauIR; %  + tau3D
muT = (1e4)*q./(tauT*me);
```

```
toc
```

The above code calls on several functions:

```
function out = G_LFC(in1,in2)

if in2 <= 1
    C12 = 1.135*in2.^(.248);
    C22 = 1.687*in2.^(.494);
elseif in2 > 1 && in2 <= 100
    C12 = 1.120*in2.^(.216);
    C22 = 1.640*in2.^(.530);
elseif in2 > 100
    C12 = 1.127*in2.^(.215);
    C22 = 1.314*in2.^(.667);
end

out = ((in2).^(2/3)).*(1.402*in1)./sqrt(2.644*C12.^2+(in1.*C22).^2);

end

function out = form2D(in1,in2,in3)
% in1 is q, in2 is zi, in3 is L
fun = @(x) (abs(wavef(x,in3)).^2).*exp(-in1.*abs(x-in2));
%     out = integral(fun,-Inf,Inf);
%       out = integral(fun,-1e-5,1e-5);
if in2 > in3
    out = 8*(pi^2).*(0.5*exp(-in1.*(in2-in3)).*(1-exp(-in1.*in3)))
    ./(in3.*in1.*(4*pi^2+(in3.^2).*(in1.^2)));
end
if in2 < 0
    out = 8*(pi^2).*(0.5*exp(-in1.*(in2)).*(1-exp(-in1.*in3)))
    ./(in3.*in1.*(4*pi^2+(in3.^2).*(in1.^2)));
end
if in2 >= 0 && in2 <= in3
    out = 8*(pi^2).*(1 - 0.5*exp(-in1.*(in2)) - 0.5*exp(-in1.*(in2-in3))
    + ((in1.*in3).^2).*(sin(pi.*in2./in3).^2)./(2*pi.^2))
    ./(in3.*in1.*(4*pi^2+(in3.^2).*(in1.^2)));
end
end

function out = form3D(in1,in2,in3)
```

```
% for top barrier
% in1 is q, in2 is L, in3 is barrier length
% fun = @(x,y) (abs(wavef(x,in2)).^2).*exp(-in1.*abs(x-y));
%     out = integral2(fun,-Inf,Inf,in2,(in3+in2));
switch nargin
    case 3
        fun = @(x) form2D(in1,x,in2).^2;
        out = integral(fun,in2,(in3+in2),'ArrayValued',true);
%         out = ((8*(pi^2).*(0.5.*(1-exp(-in1.*in2)))
./(in2.*in1.*(4*pi^2+(in2.^2)
.*(in1.^2)))).^2)*(exp(-2.*in1.*(in2-in3))./(2*in1));
    otherwise
        out = ((8*(pi^2).*(0.5.*(1-exp(-in1.*in2)))
        ./(in2.*in1.*(4*pi^2+(in2.^2).*(in1.^2)))).^2)./(2*in1);
end
end

function out = formB(in1,in2)
% in1 is q, in2 is L
    fun = @(x) form2D(in1,x,in2).^2;

    out = ((4*pi^2/((4*pi^2+(in1*in2)^2)))^2)
    *((4/(in1*in2)^2)*(1-7/(4*in1*in2)
    -(exp(-2*in1*in2)/(4*in1*in2))+(2/(in1*in2)+0.5)*(exp(-in1*in2)))
    +((1-exp(-in1*in2))/(in1*in2))^2+4*((3*(in1*in2)^2/(32*pi^2))
    +1/(2*pi^2)-(1-exp(-in1*in2))
    /((in1*in2)*(4*pi^2+(in1*in2)^2))))/(in1*in2);


end

function out = formC2(in1,in2)
out = (3*in2*in1+(8*(pi^2)/(in2*in1))-
(32*pi^4)*(1-exp(-in2*in1))/(((in1*in2)^2)
*(4*pi^2+(in2*in1)^2)))/(4*pi^2+(in2^2)*(in1^2));
end

function out = formD(in1,in2)
% in1 is q, in2 is L
%     fun = @(x,y) ((abs(wavef(x,in2)).^2).*exp(-in1.*abs(x-y))).^2;
%     out = integral2(fun,-Inf,Inf,-Inf,Inf);

    fun = @(x) form2D(in1,x,in2).^2;
```

```
%     out = integral(fun,-Inf,Inf,'ArrayValued',true);
    out = integral(fun,-1e-5,1e-5,'ArrayValued',true);
end

function out = wavef(in1,in2)
% in1 is z, in2 is L
for i = 1:length(in1)
if in1(i) <= in2 && in1(i) >= 0
    out(i) = sqrt(2/in2).*sin(pi.*in1(i)./in2);
else
    out(i) = 0;
end
end
```

Appendix C

MATLAB code of quantum well band structure calculation

The following is the MATLAB code used for $k \cdot p$ theory of a bulk III-V semiconductor. The details of the $k \cdot p$ theory are given in [2]. Several lines of codes are split for visual clarity in this document.

```
% Notes:
% This function returns 8 band kp band structure near gamma of
% III-V zincblende semiconductors using the parameters described
% by Vurgaftman et al. "Bands and Photons in III-V
% semiconductor Quantum structures"
% (Oxford University Press, 2021)
% This is a bulk calculation that includes for strain effects, does line
% cuts from gamma

%% Initialization

clear
close all
fclose('all');
clc

%% Fundamental Constants
```

```
q = 1.602e-19;          % Elementary Charge C
hbar = 1.054571e-34;    % Reduced Planck's Constant Js
kB = 1.380649e-23;      % Boltzmann Constant J/K
m0 = 9.1093837015e-31;  % Electron rest mass Kg
% epp = (1e20)*(hbar^2)/(q*2*m0); %
epp = 3.8132391;        % hbar^2/2m0 in units of eV/A^2

%% Specifying input parameters

T = 0;              % Temperature in K
X = 0.81;           % Alloy fraction
name = 'InGaAs';    % Material name
names = 'InAlAs';   % Substrate material name
Xs = 0.75;          % Substrate material alloy fraction

% Get Material Parameters
[alat, eg, vbo, delta, ep, fkane, eff_mass, deform_pot, cel]
= mkpparam(name,T,X);

% Get substrate lattice constant
alatsub = mkpparam(names,T,Xs);

% K vectors to calculate over
nk = 500;                           % number of k points
akk = 2*pi/(alatsub);               % Calculating the basic k vector
kxvec = linspace(0,0.1*akk,nk);
kzvec = linspace(0,0.1*akk,nk);

%% Computing kp parameters

% Calculating relavent parameters for kp calculations
ec = eg + vbo;                  % Conduction band energy eV
ev = vbo;                       % Valence band energy eV
ame = eff_mass(1);              % electron effective mass
gam1 = eff_mass(2);             % luttinger parameters
gam2 = eff_mass(3);
gam3 = eff_mass(4);
ac = deform_pot(1);             % ac deformation potential eV
av = deform_pot(2);             % av deformation potential eV
bv = deform_pot(3);             % bv deformation potential eV
c11 = cel(1);                   % c11 elastic constant GPa
c12 = cel(2);                   % c12 elastic constant GPa
```

```
epsx = alatsub/alat -1;          % in plane strain
epsz = -2*epsx*c12/c11;          % out of plane strain

% converting values for hamiltonian
pcv = sqrt(epp*ep);
mpar = epp*(gam1 - 2.*gam2);
lpar = epp*(gam1 + 4.*gam2 - ep/eg) - mpar;
npar = epp*(6.*gam3 - ep/eg);
opf = -epp*(1./ame-ep*(eg+2.*delta/3.)/(eg*(eg+delta)));
el = av + 2.*bv;
em = av - bv;

%% Solving Hamiltonian

h = zeros(8,8);
Ekx = zeros(8,length(kxvec));
% Solving the Hamiltonian along kz = 0, various kx
for i = 1:length(kxvec)
    akz = 0;
    akzsq = akz.^2;
    aky = 0;
    akysq = aky.^2;
    akx = kxvec(i);
    akxsq = akx.^2;
    akgsq = akxsq + akysq + akzsq;
    ane = zeros(1,11);

    ane(1) = ec - opf*akgsq + ac*(2*epsx + epsz);
    ane(2) = ev - delta/3;
    ane(3) = delta/3;
    ane(4) = lpar;
    ane(5) = mpar;
    ane(6) = npar;
    ane(7) = pcv;
    ane(8) = el*epsx;
    ane(9) = el*epsz;
    ane(10) = em*(epsx + epsz);
    ane(11) = em*2*epsx;

    % h4 is a 4x4 matrix
    h4 = [ane(1), (0.+1.i)*ane(7)*akx,
        (0.+1.i)*ane(7)*aky, (0.+1.i)*ane(7)*akz;
```

```
        (0.-1.i)*ane(7)*akx,
        ane(2)-ane(4)*akx^2-ane(5)*akgsq+ane(8)+ane(10),
        -ane(6)*akx*aky,-ane(6)*akx*akz;
        (0.-1.i)*ane(7)*aky, -ane(6)*akx*aky,
        ane(2)-ane(4)*aky^2-ane(5)*akgsq+ane(8)+ane(10), -ane(6)*aky*akz;
        (0.-1.i)*ane(7)*akz, -ane(6)*akx*akz,
        -ane(6)*aky*akz, ane(2)-ane(4)*akzsq-ane(5)*akgsq+ane(9)+ane(11)];
    h = [h4, zeros(4,4);
        zeros(4,4), h4];
    hso = [0, 0, 0, 0, 0, 0, 0, 0;
        0, 0, (0.-1.i)*ane(3), 0, 0, 0, 0, (1)*ane(3);
        0, (0.+1.i)*ane(3), 0, 0, 0, 0, 0, (0.-1.i)*ane(3);
        0, 0, 0, 0, 0, -ane(3), (0.+1.i)*ane(3), 0
        0, 0, 0, 0, 0, 0, 0, 0;
        0, 0, 0,-ane(3), 0, 0, (0.+1.i)*ane(3), 0;
        0, 0, 0, (0.-1.i)*ane(3), 0, (0.-1.i)*ane(3), 0, 0;
        0, ane(3), (0.+1.i)*ane(3), 0, 0, 0, 0, 0];
    h = h + hso;
    Ekx(:,i) = eig(h);

end

h = zeros(8,8);
Ekz = zeros(8,length(kzvec));
% Solving the Hamiltonian along kx = 0, various kz
for i = 1:length(kzvec)
    akz = kzvec(i);
    akzsq = akz.^2;
    akzsq = akz.^2;
    aky = 0;
    akysq = aky.^2;
    akx = 0;
    akxsq = akx.^2;
    akgsq = akxsq + akysq + akzsq;
    ane = zeros(1,11);

    ane(1) = ec - opf*akgsq + ac*(2*epsx + epsz);
    ane(2) = ev - delta/3;
    ane(3) = delta/3;
    ane(4) = lpar;
    ane(5) = mpar;
    ane(6) = npar;
```

```
    ane(7) = pcv;
    ane(8) = el*epsx;
    ane(9) = el*epsz;
    ane(10) = em*(epsx + epsz);
    ane(11) = em*2*epsx;

    h4 = [ane(1), (0.+1.i)*ane(7)*akx,
        (0.+1.i)*ane(7)*aky, (0.+1.i)*ane(7)*akz;
        (0.-1.i)*ane(7)*akx, ane(2)-ane(4)*akx^2-ane(5)
        *akgsq+ane(8)+ane(10),
        -ane(6)*akx*aky,-ane(6)*akx*akz;
        (0.-1.i)*ane(7)*aky, -ane(6)*akx*aky,
        ane(2)-ane(4)*aky^2-ane(5)*akgsq+ane(8)+ane(10), -ane(6)*aky*akz;
        (0.-1.i)*ane(7)*akz, -ane(6)*akx*akz,
        -ane(6)*aky*akz, ane(2)-ane(4)*akzsq-ane(5)*akgsq+ane(9)+ane(11)];
    h = [h4, zeros(4,4);
        zeros(4,4), h4];
    hso = [0, 0, 0, 0, 0, 0, 0, 0;
        0, 0, (0.+1.i)*ane(3), 0, 0, 0, 0, (1)*ane(3);
        0, (0.-1.i)*ane(3), 0, 0, 0, 0, 0, (0.+1.i)*ane(3);
        0, 0, 0, 0, 0, -ane(3), (0.-1.i)*ane(3), 0
        0, 0, 0, 0, 0, 0, 0, 0;
        0, 0, 0,-ane(3), 0, 0, (0.-1.i)*ane(3), 0;
        0, 0, 0, (0.+1.i)*ane(3), 0, (0.+1.i)*ane(3), 0, 0;
        0, ane(3), (0.-1.i)*ane(3), 0, 0, 0, 0, 0];
    h = h + hso;
    Ekz(:,i) = eig(h);



end

%% Fitting the nonparabalicity of the effective mass

EK_Kane = @(p,x) (sqrt(1 + 4*p(2)*(epp*x.^2)/p(1)) - 1)/(2*p(2)) + p(3);
p0 = [ame,1,Ekx(7,1)];
p = lsqcurvefit(EK_Kane,p0,kxvec,Ekx(7,:));
mstar = p(1);
alpha = p(2);
E_off = p(3);
```

The following is the MATLAB code used for $k \cdot p$ theory of a III-V heterostrucuture.

```
% Notes:
% This function returns 8 band kp band structure near gamma of III-V
% zincblende semiconductors heterostructures using the parameters
% described by Vurgaftman et al.
% "Bands and Photons in III-V semiconductor Quantum structures"
% (Oxford University Press, 2021)
% This is a SL/QW calculation that includes for strain effects, does line
% cuts from gamma using the recipricol space method

%% Initialization

clear
close all
fclose('all');
clc

%% Fundamental Constants

q = 1.602e-19;          % Elementary Charge C
hbar = 1.054571e-34;    % Reduced Planck's Constant Js
kB = 1.380649e-23;      % Boltzmann Constant J/K
m0 = 9.1093837015e-31;  % Electron rest mass Kg
% epp = (1e20)*(hbar^2)/(q*2*m0); %
epp = 3.8132391;        % hbar^2/2m0 in units of eV/A^2
e0 = 8.854188e-12;      % Vacuum permittivity F/m

%% Specifying input parameters

% Temperature in K
T = 0;
% Substrate material name
names = 'InAlAs';
% Substrate material alloy fraction
Xs = 0.75;
% Get substrate lattice constant
alatsub = mkpparam(names,T,Xs);

% Define material vector
% Layer Materials
name = ["InAlAs","InGaAs","InAlAs"];
% Layer thickness in A
d = [300, 300, 300];
```

```
% Layer composition alloy fraction
X = [0.75,0.81,0.75];

% Reciprocal lattice points to calculate
dsl = sum(d);                          % Total      layer thickness in A
ng = round(0.35*dsl/alatsub);          % Number of reciprocal lattice points
if ng < 2
    ng = 2;
end
% ng = 18;

% K vectors to calculate over
nkx = 100;                              % number of k points
akk = 2*pi/(alatsub);                  % Calculating the basic k vector
kxvec = linspace(0,0.05*akk,nkx);
% kxvec = 0;
nkz = 20;                              % number of k points
kzvec = linspace(0,1*pi/dsl,nkz);

%% Setting up the parameters for creating the hamiltonian

% Creating the empty hamiltonian matrix
nbb = 8;
nb = (2*ng+1)*nbb;

% Usefule parameters for k dot p
ds = cumsum(d) - d/2;              % Center point of each layer
nl = length(d);
ec = zeros(1,nl);
ev = zeros(1,nl);
delta = zeros(1,nl);
ep = zeros(1,nl);
ame = zeros(1,nl);
gam1 = zeros(1,nl);
gam2 = zeros(1,nl);
gam3 = zeros(1,nl);
ac = zeros(1,nl);
av = zeros(1,nl);
bv = zeros(1,nl);
c11 = zeros(1,nl);
c12 = zeros(1,nl);
epsx = zeros(1,nl);
```

```
epsz = zeros(1,nl);

% Get Material Parameters
for j = 1:length(d)
    [a1, a2, a3, a4, a5, a6, a7, a8, a9] = mkpparam(name(j),T,X(j));
    ec(j) = a2 + a3;
    ev(j) = a3;
    delta(j) = a4;
    ep(j) = a5;
    ame(j) = a7(1);
    gam1(j) = a7(2);
    gam2(j) = a7(3);
    gam3(j) = a7(4);
    ac(j) = a8(1);
    av(j) = a8(2);
    bv(j) = a8(3);
    c11(j) = a9(1);
    c12(j) = a9(2);
    epsx(j) = alatsub/a1 - 1;
    epsz(j) = -2*epsx(j)*c12(j)/c11(j);
end
eg = ec-ev;

% Reciprocal lattice vectors
gm = linspace(-ng,ng,2*ng+1)*2*pi/dsl;

% converting values for hamiltonian
pcv = sqrt(epp*ep);
mpar = epp*(gam1 - 2.*gam2);
lpar = epp*(gam1 + 4.*gam2 - ep./eg) - mpar;
npar = epp*(6.*gam3 - ep./eg);
opf = -epp*(1./ame-ep.*(eg+2.*delta/3.)./(eg.*(eg+delta)));
el = av + 2.*bv;
em = av - bv;

%% Generating and solving the hamiltonian

wx = zeros(nb,length(kxvec));
vx = zeros(nb,nb,length(kxvec));
for k = 1:length(kxvec)

    h = zeros(nb,nb);
```

```
for x = 1:length(gm)
    for y = 1:length(gm)
        gmd = gm(y) - gm(x);
        akz = 0;
        akzs = akz + 0.5*(gm(x) + gm(y));
        akzsq = (akz + gm(x))*(akz + gm(y));
        aky = 0;
        akysq = aky.^2;
        akx = kxvec(k);
        akxsq = akx.^2;
        akgsq = akxsq + akysq + akzsq;
        ane = zeros(1,11);

        for z = 1:length(d)
            ene = zeros(1,11);
            ene(1) = ec(z) - opf(z)*akgsq
            + ac(z).*(2*epsx(z) + epsz(z));
            ene(2) = ev(z) - delta(z)/3;
            ene(3) = delta(z)/3;
            ene(4) = lpar(z);
            ene(5) = mpar(z);
            ene(6) = npar(z);
            ene(7) = pcv(z);
            ene(8) = el(z).*epsx(z);
            ene(9) = el(z).*epsz(z);
            ene(10) = em(z)*(epsx(z) + epsz(z));
            ene(11) = em(z).*2.*epsx(z);
            if x == y
                aa = d(z).*ene./dsl;
            else
                aa = 2.0*sin(0.5*gmd*d(z)).*ene./(gmd.*dsl);
            end
            ane = ane + aa*exp(-1i*gmd*ds(z));
        end

        % h4 is 4x4
        h4 = [ane(1), (0.+1.i)*ane(7)*akx,
            (0.+1.i)*ane(7)*aky, (0.+1.i)*ane(7)*akzs;
        (0.-1.i)*ane(7)*akx,
            ane(2)-ane(4)*akx^2-ane(5)*akgsq+ane(8)+ane(10),
            -ane(6)*akx*aky,-ane(6)*akx*akzs;
        (0.-1.i)*ane(7)*aky, -ane(6)*akx*aky,
```

```
                ane(2)-ane(4)*aky^2-ane(5)*akgsq+ane(8)+ane(10),
                -ane(6)*aky*akzs;
            (0.-1.i)*ane(7)*akzs, -ane(6)*akx*akzs,
                -ane(6)*aky*akzs,
                ane(2)-ane(4)*akzsq-ane(5)*akgsq+ane(9)+ane(11)];
            h8 = [h4, zeros(4,4);
                zeros(4,4), h4];
            hso = [0, 0, 0, 0, 0, 0, 0, 0;
                0, 0, (0.+1.i)*ane(3), 0, 0, 0, 0, (1)*ane(3);
                0, (0.-1.i)*ane(3), 0, 0, 0, 0, 0, (0.+1.i)*ane(3);
                0, 0, 0, 0, 0, -ane(3), (0.-1.i)*ane(3), 0
                0, 0, 0, 0, 0, 0, 0, 0;
                0, 0, 0,-ane(3), 0, 0, (0.-1.i)*ane(3), 0;
                0, 0, 0, (0.+1.i)*ane(3), 0, (0.+1.i)*ane(3), 0, 0;
                0, ane(3), (0.-1.i)*ane(3), 0, 0, 0, 0, 0];
            h((8*(x-1)+1):8*(x),(8*(y-1)+1):8*(y)) = h8 + hso;

        end
    end

    [vk,wkm] = eig(h);
    wk = diag(wkm);

    wx(:,k) = wk;
    vx(:,:,k) = vk;

end

wz = zeros(nb,length(kzvec));
vz = zeros(nb,nb,length(kzvec));
for k = 1:length(kzvec)

    h = zeros(nb,nb);
    for x = 1:length(gm)
        for y = 1:length(gm)
            gmd = gm(y) - gm(x);
            akz = kzvec(k);
            akzs = akz + 0.5*(gm(x) + gm(y));
            akzsq = (akz + gm(x))*(akz + gm(y));
            aky = 0;
            akysq = aky.^2;
            akx = 0;
```

```
akxsq = akx.^2;
akgsq = akxsq + akysq + akzsq;
ane = zeros(1,11);

for z = 1:length(d)
    ene = zeros(1,11);
    ene(1) = ec(z) - opf(z)*akgsq +
    ac(z).*(2*epsx(z) + epsz(z));
    ene(2) = ev(z) - delta(z)/3;
    ene(3) = delta(z)/3;
    ene(4) = lpar(z);
    ene(5) = mpar(z);
    ene(6) = npar(z);
    ene(7) = pcv(z);
    ene(8) = el(z).*epsx(z);
    ene(9) = el(z).*epsz(z);
    ene(10) = em(z)*(epsx(z) + epsz(z));
    ene(11) = em(z).*2.*epsx(z);
    if x == y
        aa = d(z).*ene./dsl;
    else
        aa = 2.0*sin(0.5*gmd*d(z)).*ene./(gmd.*dsl);
    end
    ane = ane + aa*exp(-1i*gmd*ds(z));
end

h4 = [ane(1), (0.+1.i)*ane(7)*akx, (0.+1.i)*ane(7)*aky,
    (0.+1.i)*ane(7)*akzs;
(0.-1.i)*ane(7)*akx,
    ane(2)-ane(4)*akx^2-ane(5)*akgsq+ane(8)+ane(10),
    -ane(6)*akx*aky,-ane(6)*akx*akzs;
(0.-1.i)*ane(7)*aky, -ane(6)*akx*aky,
    ane(2)-ane(4)*aky^2-ane(5)*akgsq+ane(8)+ane(10),
    -ane(6)*aky*akzs;
(0.-1.i)*ane(7)*akzs, -ane(6)*akx*akzs,
    -ane(6)*aky*akzs,
    ane(2)-ane(4)*akzsq-ane(5)*akgsq+ane(9)+ane(11)];
h8 = [h4, zeros(4,4);
    zeros(4,4), h4];
hso = [0, 0, 0, 0, 0, 0, 0, 0;
    0, 0, (0.-1.i)*ane(3), 0, 0, 0, 0, (1)*ane(3);
    0, (0.+1.i)*ane(3), 0, 0, 0, 0, 0, (0.-1.i)*ane(3);
```

```
                0, 0, 0, 0, 0, -ane(3), (0.+1.i)*ane(3), 0
                0, 0, 0, 0, 0, 0, 0, 0;
                0, 0, 0,-ane(3), 0, 0, (0.+1.i)*ane(3), 0;
                0, 0, 0, (0.-1.i)*ane(3), 0, (0.-1.i)*ane(3), 0, 0;
                0, ane(3), (0.+1.i)*ane(3), 0, 0, 0, 0, 0];
            h((8*(x-1)+1):8*(x),(8*(y-1)+1):8*(y)) = h8 + hso;

        end
    end

    [vk,wkm] = eig(h);
    wk = diag(wkm);

    wz(:,k) = wk;
    vz(:,:,k) = vk;

end

%% Fitting the nonparabalicity of the effective mass

EK_Kane = @(p,x) (sqrt(1 + 4*p(2)*(epp*x.^2)/p(1)) - 1)/(2*p(2)) + p(3);
p0 = [ame(2),1,ec(2)];
p = lsqcurvefit(EK_Kane,p0,kxvec,wx((12*ng+8),:));
mstar = p(1);
alpha = p(2);
E_off = p(3);

%% Generating wave functions a k = 0

% Creating parameters for the wavefunction
np = 500;
dp = dsl/np/2;
dist = linspace(dp,dsl-dp,np);
dend = cumsum(d);
dstart = dend - d;
ec_dist = zeros(1,np);
ev_dist = zeros(1,np);

% Make Ec, Ev vs position plots
for j = 1:length(dist)
    d_temp = dist(j);
    for k = 1:length(d)
```

```
        if d_temp > dstart(k) && d_temp <= dend(k)
            ec_dist(j) = ec(k);
            ev_dist(j) = ev(k);
        end
    end
end

% Set Bands to plot wave functions of,
% currently set to the 1st 4 conduction band subbands
wf_sb_ind = [(12*ng+8),(12*ng+10),(12*ng+12),(12*ng+13)];

% Matrices for wavefunction coefficients
wf_sb_s1 = zeros(nb/8,length(wf_sb_ind));
wf_sb_s2 = zeros(nb/8,length(wf_sb_ind));
wf_sb_px1 = zeros(nb/8,length(wf_sb_ind));
wf_sb_px2 = zeros(nb/8,length(wf_sb_ind));
wf_sb_py1 = zeros(nb/8,length(wf_sb_ind));
wf_sb_py2 = zeros(nb/8,length(wf_sb_ind));
wf_sb_pz1 = zeros(nb/8,length(wf_sb_ind));
wf_sb_pz2 = zeros(nb/8,length(wf_sb_ind));

% Wavefunction of different subbands
wv_sb = zeros(np,length(wf_sb_ind));
wv_sb_s = zeros(np,length(wf_sb_ind));
wv_sb_px = zeros(np,length(wf_sb_ind));
wv_sb_py = zeros(np,length(wf_sb_ind));
wv_sb_pz = zeros(np,length(wf_sb_ind));


% Find fourier coeffiencts for the different orbitals
% and generate the wavefunctions
for j = 1:length(wf_sb_ind)
    wf_sb_E(j) = wx(wf_sb_ind(j),1);
    for k = 1:(2*ng+1)
        wf_sb_s1(k,j) = vx(8*(k-1) + 1,wf_sb_ind(j),1);
        wf_sb_s2(k,j) = vx(8*(k-1) + 5,wf_sb_ind(j),1);
        wf_sb_px1(k,j) = vx(8*(k-1) + 2,wf_sb_ind(j),1);
        wf_sb_px2(k,j) = vx(8*(k-1) + 6,wf_sb_ind(j),1);
        wf_sb_py1(k,j) = vx(8*(k-1) + 3,wf_sb_ind(j),1);
        wf_sb_py2(k,j) = vx(8*(k-1) + 7,wf_sb_ind(j),1);
        wf_sb_pz1(k,j) = vx(8*(k-1) + 4,wf_sb_ind(j),1);
        wf_sb_pz2(k,j) = vx(8*(k-1) + 8,wf_sb_ind(j),1);
```

```
        wv_sb_s(:,j) = wv_sb_s(:,j)
        + wf_sb_s1(k,j).*exp(1i*gm(k)*dist)'
        + wf_sb_s2(k,j).*exp(1i*gm(k)*dist)';
        wv_sb_px(:,j) = wv_sb_px(:,j)
        + wf_sb_px1(k,j).*exp(1i*gm(k)*dist)'
        + wf_sb_px2(k,j).*exp(1i*gm(k)*dist)';
        wv_sb_py(:,j) = wv_sb_py(:,j)
        + wf_sb_py1(k,j).*exp(1i*gm(k)*dist)'
        + wf_sb_py2(k,j).*exp(1i*gm(k)*dist)';
        wv_sb_pz(:,j) = wv_sb_pz(:,j)
        + wf_sb_pz1(k,j).*exp(1i*gm(k)*dist)'
        + wf_sb_pz2(k,j).*exp(1i*gm(k)*dist)';
    end
    wv_sb(:,j) = wv_sb_s(:,j) + wv_sb_px(:,j)
    + wv_sb_py(:,j) + wv_sb_pz(:,j);
end

%% Computing the peak carrier denisty

Esub = wf_sb_E(2) - wf_sb_E(1);
ksub = sqrt((Esub.*(1+alpha.*Esub).*mstar)./(epp));            % A^-1
n2D = ((ksub*1e8).^2)/(2*pi);                                  % cm^-2
```

These both of this code relies on the following function to obtain material parameters.

```
% Notes:
% 1 This function returns the material parameters of III-V zincblende
% semiconductors using the parameters described by Vurgaftman et al.
% "Bands and Photons n III-V semiconductor Quantum structures"
% (Oxford University Press, 2021)
% Focus is on returning parameters relavent for k dot p computations
% For more general calculations such as dielectric properties are WIP
% 2 Computes parameters for binaries and ternaries, no functionality for
% quaternaries (WIP), only gives deformation potentials and strain
% potentials for biaxial strain (epitaxial strain)4
% Works best at T = 0

% Currently supported Materials:
% Binaries: GaAs, AlAs, InAs, InP, GaSb, AlSb, InSb
% Ternaries: AlGaAs, InAlAs, InGaAs, AlGaSb, AlInSb, GaInSb, InAsSb,
% AlAsSb
```

```
% Inputs:
% 1 Material Name(String)
% 2 Temperature (K)
% 3 X alloy fraction for 1st material in the alloy e.g. Al in AlGaAs

% Outputs:
% 1 Lattice constant (A)
% 2 Band gap (eV)
% 3 Valence band offset (eV) w.r.t InSb VBO
% 4 Delta/SO splitting (eV)
% 5 Kane Energy (eV)
% 6 F Remote band correction
% 7 Electron effective mass (1/me), luttinger parameters
% 8 Deformation Potentials (eV)
% 9 Elastic Constants (GPa)

%% Actual Function

function [alat, eg, vbo, delta, ep, fkane, eff_mass, deform_pot, cel]
= mkpparam(name,T,X)
if strcmp(name,'GaAs')
    alat = 5.65325 + (3.88e-5)*(T-300);
    eg = 1.519 - ((5.41e-4)*T.^2)./(T + 204);
    vbo = -0.8;
    delta = 0.341;
    ep = 25.6;
    fkane = -1;
    el_mass = 1/(1 + 2*fkane +ep*(eg+2*delta/3)/(eg*(eg+delta)));
    eff_mass = [el_mass, 6.98, 2.06, 2.93];
    deform_pot = [-7.17, 1.16, -2];
    cel = [122.1, 56.6];

elseif strcmp(name,'AlAs')
    alat = 5.66139 + (2.90e-5)*(T-300);
    eg = 3.099 - ((8.85e-4)*T.^2)./(T + 530);
    vbo = -1.33;
    delta = 0.28;
    ep = 21.1;
    fkane = -0.48;
    el_mass = 1/(1 + 2*fkane +ep*(eg+2*delta/3)/(eg*(eg+delta)));
    eff_mass = [el_mass, 3.76, 0.82, 1.42];
```

```
    deform_pot = [-5.64, 2.47, -2.3];
    cel = [125, 53.4];

elseif strcmp(name,'InAs')
    alat = 6.0583 + (2.70e-5)*(T-300);
    eg = 0.417 - ((3.07e-4)*T.^2)./(T + 191);
    vbo = -0.62;
    delta = 0.367;
    ep = 19.5;
    fkane = -1;
    el_mass = 1/(1 + 2*fkane +ep*(eg+2*delta/3)/(eg*(eg+delta)));
    eff_mass = [el_mass, 19.7, 8.4, 9.3];
    deform_pot = [-5.08, 1, -1.8];
    cel = [83.29, 45.26];

elseif strcmp(name,'InP')
    alat = 5.8687 + (2.79e-5)*(T-300);
    eg = 1.4236 - ((3.63e-4)*T.^2)./(T + 162);
    vbo = -0.94;
    delta = 0.108;
    ep = 19.8;
    fkane = -1;
    el_mass = 1/(1 + 2*fkane +ep*(eg+2*delta/3)/(eg*(eg+delta)));
    eff_mass = [el_mass, 5.08, 1.6, 2.1];
    deform_pot = [-6, 0.6, -2];
    cel = [101.1, 56.1];

elseif strcmp(name,'GaSb')
    alat = 6.0959 + (4.72e-5)*(T-300);
    eg = 0.812 - ((4.17e-4)*T.^2)./(T + 140);
    vbo = -0.03;
    delta = 0.76;
    ep = 25.8;
    fkane = -1;
    el_mass = 1/(1 + 2*fkane +ep*(eg+2*delta/3)/(eg*(eg+delta)));
    eff_mass = [el_mass, 13.4, 4.7, 6];
    deform_pot = [-7.5, 0.8, -2.];
    cel = [88.42, 40.26];

elseif strcmp(name,'AlSb')
    alat = 6.1355 + (2.60e-5)*(T-300);
    eg = 2.386 - ((4.20e-4)*T.^2)./(T + 140);
```

```
    vbo = -0.41;
    delta = 0.676;
    ep = 18.7;
    fkane = -0.56;
    el_mass = 1/(1 + 2*fkane +ep*(eg+2*delta/3)/(eg*(eg+delta)));
    eff_mass = [el_mass, 5.18, 1.19, 1.97];
    deform_pot = [-4.5, 1.4, -1.35];
    cel = [87.69, 43.41];

elseif strcmp(name,'InSb')
    alat = 6.4794 + (3.48e-5)*(T-300);
    eg = 0.235 - ((3.20e-4)*T.^2)./(T + 170);
    vbo = -0.;
    delta = 0.81;
    ep = 23.3;
    fkane = -0.23;
    el_mass = 1/(1 + 2*fkane +ep*(eg+2*delta/3)/(eg*(eg+delta)));
    eff_mass = [el_mass, 34.8, 15.5, 16.5];
    deform_pot = [-6.94, 0.36, -2.];
    cel = [68.47, 37.35];

elseif strcmp(name,'AlGaAs')
    alat = (X).*(5.66139 + (2.90e-5)*(T-300))
    + (1-X).*(5.65325 + (3.88e-5)*(T-300));
    eg = (X)*(3.099 - ((8.85e-4)*T.^2)./(T + 530))+ (1-X)*(1.519
    - ((5.41e-4)*T.^2)./(T + 204)) - X*(1-X)*(-0.127+1.310*X);
    vbo = (X)*(-1.33) + (1-X)*(-0.8);
    delta = (X)*(0.28) + (1-X)*0.341;
    ep = (X)*(21.1) + (1-X)*25.6 - X*(1-X)*3.2;
    fkane = (X)*(-0.48) + (1-X)*(-1);
    el1 = 0.15;
    el2 = 0.0675;
    el_mass = X*(el1) + (1-X)*el2;
    gam1 = [3.76, 0.82, 1.42];
    gam2 = [6.98, 2.06, 2.93];
    hh1 = 1/(gam1(1) - 2*gam1(2));
    hh2 = 1/(gam2(1) - 2*gam2(2));
    hh_mass = (X)*hh1 + (1-X)*hh2;
    lh1 = 1/(gam1(1) + 2*gam1(2));
    lh2 = 1/(gam2(1) + 2*gam2(2));
    lh_mass = el_mass*((1/el1)*(X)*lh1 + (1/el2)*(1-X)*lh2);
    gg1 = X*(gam1(3) - gam1(2));
```

```
    gg2 = (1-X)*(gam2(3) - gam2(2));
    eff_mass = [el_mass,0.5/hh_mass + 0.5/lh_mass,
    0.25/lh_mass - 0.25/hh_mass,0.25/lh_mass - 0.25/hh_mass + gg1 + gg2];
    deform_pot = (X)*[-5.64, 2.47, -2.3] + (1-X)*[-7.17, 1.16, -2];
    cel = (X)*[125, 53.4] + (1-X)*[122.1, 56.6];

elseif strcmp(name,'InGaAs')
    alat = (X).*(6.0583 + (2.7e-5)*(T-300))
    + (1-X).*(5.65325 + (3.88e-5)*(T-300));
    eg = (X)*(0.417 - ((3.07e-4)*T.^2)./(T + 191))
    + (1-X)*(1.519 - ((5.41e-4)*T.^2)./(T + 204)) - X*(1-X)*(0.477);
    vbo = (X)*(-0.62) + (1-X)*(-0.8) - X*(1-X)*(-0.61);
    delta = (X)*(0.367) + (1-X)*0.341 - X*(1-X)*(0.15);
    ep = (X)*(19.5) + (1-X)*25.6 - X*(1-X)*-4.2;
    fkane = (X)*(-1) + (1-X)*(-1);
    el1 = 0.026;
    el2 = 0.0675;
    el_mass = X*(el1) + (1-X)*el2 - X*(1-X)*0.005;
    gam1 = [19.7, 8.4, 9.3];
    gam2 = [6.98, 2.06, 2.93];
    hh1 = 1/(gam1(1) - 2*gam1(2));
    hh2 = 1/(gam2(1) - 2*gam2(2));
    hh_mass = (X)*hh1 + (1-X)*hh2 - X*(1-X)*(-0.145);
    lh1 = 1/(gam1(1) + 2*gam1(2));
    lh2 = 1/(gam2(1) + 2*gam2(2));
    lh_mass = el_mass*((1/el1)*(X)*lh1 + (1/el2)*(1-X)*lh2);
    gg1 = X*(gam1(3) - gam1(2));
    gg2 = (1-X)*(gam2(3) - gam2(2));
    eff_mass = [el_mass,0.5/hh_mass + 0.5/lh_mass,
    0.25/lh_mass - 0.25/hh_mass,0.25/lh_mass - 0.25/hh_mass + gg1 + gg2];
    deform_pot = (X)*[-5.08, 1, -1.8]
    + (1-X)*[-7.17, 1.16, -2] - X*(1-X)*[2.61 0 0];
    cel = (X)*[83.29, 45.26] + (1-X)*[122.1, 56.6];

elseif strcmp(name,'InAlAs')
    alat = (X).*(6.0583 + (2.7e-5)*(T-300))
    + (1-X).*(5.66139 + (2.90e-5)*(T-300));
    eg = (X)*(0.417 - ((3.07e-4)*T.^2)./(T + 191))
    + (1-X)*(3.099 - ((8.85e-4)*T.^2)./(T + 530)) - X*(1-X)*(0.7);
    vbo = (X)*(-0.62) + (1-X)*(-1.33) - X*(1-X)*(-0.824);
    delta = (X)*(0.367) + (1-X)*(0.28) - X*(1-X)*(0.15);
    ep = (X)*(19.5) + (1-X)*(21.1) + X*(1-X)*-10.2;
```

```
    fkane = (X)*(-1) + (1-X)*(-0.48);
    el1 = 0.026;
    el2 = 0.15;
    el_mass = X*(el1) + (1-X)*el2 - X*(1-X)*0.049;
    gam1 = [19.7, 8.4, 9.3];
    gam2 = [3.76, 0.82, 1.42];
    hh1 = 1/(gam1(1) - 2*gam1(2));
    hh2 = 1/(gam2(1) - 2*gam2(2));
    hh_mass = (X)*hh1 + (1-X)*hh2;
    lh1 = 1/(gam1(1) + 2*gam1(2));
    lh2 = 1/(gam2(1) + 2*gam2(2));
    lh_mass = el_mass*((1/el1)*(X)*lh1 + (1/el2)*(1-X)*lh2);
    gg1 = X*(gam1(3) - gam1(2));
    gg2 = (1-X)*(gam2(3) - gam2(2));
    eff_mass = [el_mass,0.5/hh_mass + 0.5/lh_mass,
    0.25/lh_mass - 0.25/hh_mass,0.25/lh_mass - 0.25/hh_mass + gg1 + gg2];
    deform_pot = (X)*[-5.08, 1, -1.8]
    + (1-X)*[-5.64, 2.47, -2.3] - X*(1-X)*[-1.4 0 0];
    cel = (X)*[83.29, 45.26] + (1-X)*[125, 53.4];

elseif strcmp(name,'AlGaSb')
    alat = (X).*(6.1355 + (2.60e-5)*(T-300))
    + (1-X).*(6.0959 + (4.72e-5)*(T-300));
    eg = (X)*(2.386 - ((4.20e-4)*T.^2)./(T + 140))
    + (1-X)*(0.812 - ((4.17e-4)*T.^2)./(T + 140)) - X*(1-X)*(-0.044+1.22*X);
    vbo = (X)*(-0.41) + (1-X)*(-0.03);
    delta = (X)*(0.676) + (1-X)*0.76 - X*(1-X)*0.3;
    ep = (X)*(18.7) + (1-X)*25.8;
    fkane = (X)*(-0.56) + (1-X)*(-1);
    el1 = 0.14;
    el2 = 0.039;
    el_mass = X*(el1) + (1-X)*el2 - X*(1-X)*0.083;
    gam1 = [5.18, 1.19, 1.97];
    gam2 = [13.4, 4.7, 6];
    hh1 = 1/(gam1(1) - 2*gam1(2));
    hh2 = 1/(gam2(1) - 2*gam2(2));
    hh_mass = (X)*hh1 + (1-X)*hh2;
    lh1 = 1/(gam1(1) + 2*gam1(2));
    lh2 = 1/(gam2(1) + 2*gam2(2));
    lh_mass = el_mass*((1/el1)*(X)*lh1 + (1/el2)*(1-X)*lh2);
    gg1 = X*(gam1(3) - gam1(2));
    gg2 = (1-X)*(gam2(3) - gam2(2));
```

```
    eff_mass = [el_mass,0.5/hh_mass + 0.5/lh_mass,
    0.25/lh_mass - 0.25/hh_mass,0.25/lh_mass - 0.25/hh_mass + gg1 + gg2];
    deform_pot = (X)*[-4.5, 1.4, -1.35] + (1-X)*[-7.5, 0.8, -2.];
    cel = (X)*[87.69, 43.41] + (1-X)*[88.42, 40.26];

elseif strcmp(name,'AlInSb')
    alat = (X).*(6.1355 + (2.60e-5)*(T-300))
    + (1-X).*(6.4794 + (3.48e-5)*(T-300));
    eg = (X)*(2.386 - ((4.20e-4)*T.^2)./(T + 140))
    + (1-X)*(0.235 - ((3.20e-4)*T.^2)./(T + 170)) - X*(1-X)*(0.43);
    vbo = (X)*(-0.41) + (1-X)*(-0.);
    delta = (X)*(0.676) + (1-X)*0.81 - X*(1-X)*0.25;
    ep = (X)*(18.7) + (1-X)*23.3;
    fkane = (X)*(-0.56) + (1-X)*(-0.23);
    el1 = 0.14;
    el2 = 0.0135;
    el_mass = X*(el1) + (1-X)*el2 - X*(1-X)*0.05;
    gam1 = [5.18, 1.19, 1.97];
    gam2 = [34.8, 15.5, 16.5];
    hh1 = 1/(gam1(1) - 2*gam1(2));
    hh2 = 1/(gam2(1) - 2*gam2(2));
    hh_mass = (X)*hh1 + (1-X)*hh2;
    lh1 = 1/(gam1(1) + 2*gam1(2));
    lh2 = 1/(gam2(1) + 2*gam2(2));
    lh_mass = el_mass*((1/el1)*(X)*lh1 + (1/el2)*(1-X)*lh2);
    gg1 = X*(gam1(3) - gam1(2));
    gg2 = (1-X)*(gam2(3) - gam2(2));
    eff_mass = [el_mass,0.5/hh_mass + 0.5/lh_mass,
    0.25/lh_mass - 0.25/hh_mass,0.25/lh_mass - 0.25/hh_mass + gg1 + gg2];
    deform_pot = (X)*[-4.5, 1.4, -1.35] + (1-X)*[-6.94, 0.36, -2.];
    cel = (X)*[87.69, 43.41] + (1-X)*[68.47, 37.35];

elseif strcmp(name,'GaInSb')
    alat = X*(6.0959 + (4.72e-5)*(T-300))
    + (1-X).*(6.4794 + (3.48e-5)*(T-300));
    eg = X*(0.812 - ((4.17e-4)*T.^2)./(T + 140))
    + (1-X)*(0.235 - ((3.20e-4)*T.^2)./(T + 170)) - X*(1-X)*(0.415);
    vbo = X*(-0.03) + (1-X)*(0);
    delta = X*0.76 + (1-X)*(0.81) - X*(1-X)*0.1;
    ep = X*25.8 + (1-X)*(23.3) - X*(1-X)*7.8;
    fkane = X*(-1) + (1-X)*(-0.23);
    el1 = 0.039;
```

```
    el2 = 0.0135;
    el_mass = X*(el1) + (1-X)*el2 - X*(1-X)*0.01;
    gam1 = [13.4, 4.7, 6];
    gam2 = [34.8, 15.5, 16.5];
    hh1 = 1/(gam1(1) - 2*gam1(2));
    hh2 = 1/(gam2(1) - 2*gam2(2));
    hh_mass = (X)*hh1 + (1-X)*hh2;
    lh1 = 1/(gam1(1) + 2*gam1(2));
    lh2 = 1/(gam2(1) + 2*gam2(2));
    lh_mass = el_mass*((1/el1)*(X)*lh1 + (1/el2)*(1-X)*lh2);
    gg1 = X*(gam1(3) - gam1(2));
    gg2 = (1-X)*(gam2(3) - gam2(2));
    eff_mass = [el_mass,0.5/hh_mass + 0.5/lh_mass,
    0.25/lh_mass - 0.25/hh_mass,0.25/lh_mass - 0.25/hh_mass + gg1 + gg2];
    deform_pot = X*[-7.5, 0.8, -2.] + (1-X)*[-6.94, 0.36, -2.];
    cel = X*[88.42, 40.26] + (1-X)*[68.47, 37.35];

    % Might be wrong?
elseif strcmp(name,'InGaSb')
    alat = X.*(6.4794 + (3.48e-5)*(T-300))
    + (1-X)*(6.0959 + (4.72e-5)*(T-300));
    eg = X*(0.235 - ((3.20e-4)*T.^2)./(T + 170))
    + (1-X)*(0.812 - ((4.17e-4)*T.^2)./(T + 140)) - X*(1-X)*(0.415);
    vbo = X*(0) + (1-X)*(-0.03);
    delta = X*(0.81) + (1-X)*0.76 - X*(1-X)*0.1;
    ep = X*(23.3) + (1-X)*25.8 - X*(1-X)*7.8;
    fkane = X*(-0.23) + (1-X)*(-1);
    el1 = 0.0135;
    el2 = 0.039;
    el_mass = X*(el1) + (1-X)*el2 - X*(1-X)*0.01;
    gam1 = [34.8, 15.5, 16.5];
    gam2 = [13.4, 4.7, 6];
    hh1 = 1/(gam1(1) - 2*gam1(2));
    hh2 = 1/(gam2(1) - 2*gam2(2));
    hh_mass = (X)*hh1 + (1-X)*hh2;
    lh1 = 1/(gam1(1) + 2*gam1(2));
    lh2 = 1/(gam2(1) + 2*gam2(2));
    lh_mass = el_mass*((1/el1)*(X)*lh1 + (1/el2)*(1-X)*lh2);
    gg1 = X*(gam1(3) - gam1(2));
    gg2 = (1-X)*(gam2(3) - gam2(2));
    eff_mass = [el_mass,0.5/hh_mass + 0.5/lh_mass,
    0.25/lh_mass - 0.25/hh_mass,0.25/lh_mass - 0.25/hh_mass + gg1 + gg2];
```

```
    deform_pot = X*[-6.94, 0.36, -2.] + (1-X)*[-7.5, 0.8, -2.];
    cel = X*[68.47, 37.35] + (1-X)*[88.42, 40.26];

elseif strcmp(name,'InAsSb')
    alat = (X).*(6.0583 + (2.70e-5)*(T-300))
    + (1-X).*(6.4794 + (3.48e-5)*(T-300));
    eg = (X)*(0.417 - ((3.07e-4)*T.^2)./(T + 191))
    + (1-X)*(0.235 - ((3.20e-4)*T.^2)./(T + 170)) - X*(1-X)*(0.84);
    vbo = (X)*(-0.62) + (1-X)*(-0.) - X*(1-X)*-0.02;
    delta = (X)*(0.367) + (1-X)*0.81 - X*(1-X)*1.2;
    ep = (X)*(19.5) + (1-X)*23.3;
    fkane = (X)*(-1) + (1-X)*(-0.23);
    el1 = 0.026;
    el2 = 0.0135;
    el_mass = 1/(1 + 2*fkane +ep*(eg+2*delta/3)/(eg*(eg+delta)));
    gam1 = [19.7, 8.4, 9.3];
    gam2 = [34.8, 15.5, 16.5];
    hh1 = 1/(gam1(1) - 2*gam1(2));
    hh2 = 1/(gam2(1) - 2*gam2(2));
    hh_mass = (X)*hh1 + (1-X)*hh2;
    lh1 = 1/(gam1(1) + 2*gam1(2));
    lh2 = 1/(gam2(1) + 2*gam2(2));
    lh_mass = el_mass*((1/el1)*(X)*lh1 + (1/el2)*(1-X)*lh2);
    gg1 = X*(gam1(3) - gam1(2));
    gg2 = (1-X)*(gam2(3) - gam2(2));
    eff_mass = [el_mass,0.5/hh_mass + 0.5/lh_mass,
    0.25/lh_mass - 0.25/hh_mass,0.25/lh_mass - 0.25/hh_mass + gg1 + gg2];
    deform_pot = (X)*[-5.08, 1, -1.8] + (1-X)*[-6.94, 0.36, -2.];
    cel = (X)*[83.29, 45.26] + (1-X)*[68.47, 37.35];


elseif strcmp(name,'AlAsSb')
    alat = X*(5.66139 + (2.90e-5)*(T-300))
    + (1-X).*(6.1355 + (2.60e-5)*(T-300));
    eg = X*(3.099 - ((8.85e-4)*T.^2)./(T + 530))
    + (1-X)*(2.386 - ((4.20e-4)*T.^2)./(T + 140)) - X*(1-X)*(1.55);
    vbo = X*(-1.33) + (1-X)*(-0.41) - X*(1-X)*(-3.41 + 3.59*X);
    delta = X*(0.28) + (1-X)*(0.676) - X*(1-X)*(0.15);
    ep = X*(21.1) + (1-X)*(18.7);
    fkane = X*(-0.48) + (1-X)*(-0.56);
    el1 = 0.15;
    el2 = 0.14;
```

```
    el_mass = X*(el1) + (1-X)*el2 - X*(1-X)*0.081;
    gam1 = [3.76, 0.82, 1.42];
    gam2 = [5.18, 1.19, 1.97];
    hh1 = 1/(gam1(1) - 2*gam1(2));
    hh2 = 1/(gam2(1) - 2*gam2(2));
    hh_mass = (X)*hh1 + (1-X)*hh2;
    lh1 = 1/(gam1(1) + 2*gam1(2));
    lh2 = 1/(gam2(1) + 2*gam2(2));
    lh_mass = el_mass*((1/el1)*(X)*lh1 + (1/el2)*(1-X)*lh2);
    gg1 = X*(gam1(3) - gam1(2));
    gg2 = (1-X)*(gam2(3) - gam2(2));
    eff_mass = [el_mass,0.5/hh_mass + 0.5/lh_mass,
    0.25/lh_mass - 0.25/hh_mass,0.25/lh_mass - 0.25/hh_mass + gg1 + gg2];
    deform_pot = X*[-5.64, 2.47, -2.3] + (1-X)*[-4.5, 1.4, -1.35];
    cel = X*[125, 53.4] + (1-X)*[87.69, 43.41];

end

end
```

Appendix D

Ohmic contact to various III-V materials

The procedures to obtain Ohmic contacts to cleaved squares of III-V in the van der Pauw geometry is listed in the table D.1 below. Squares are approximately 5×5 mm. If the contacts were annealed, the contacts were annealed on a hot plate in ambient conditions. The InSn used is the eutectic alloy composition of InSn (Thermo Fisher Scientific). Etching the InSn or In with HCl is recommened before use, otherwise oxygen can incorporate into the soldered contact and inhibit diffusion of the contact metal into the III-V. It has been found that a contact anneal is not always required for InSb 2DEGs. Be careful to not contaminate the pure In solder iron with InSn.

Table D.1: Ohmic contact procedure for various III-V materials for Hall measurements in the van der Pauw geometry.

Material	Metal	Anneal temperature (°C)	Time (min)
nGaAs	InSn	375	30 - 60
pGaAs	In	375	30 - 60
GaAs/AlGaAs 2DEG	InSn	375	60 - 120
Near surface InAs QW on InP	InSn	N/A	N/A
Deep InAs 2DEG on InP	InSn	250	15
Deep InAs 2DEG on GaSb	InSn	220	20
Deep InGaAs 2DEG on InP	InSn	250	15
InSb 2DEG on GaSb	InSn	180	20

Appendix E

Field emission cleaning of a STM tip

Field emission cleaning of a STM tip was found to be an effective technique for eliminating contaminants and reshaping the apex of the tip. By doing so, the effective lifetime of a STM tip can be increased. It was found to be particularily effective in eliminating nonmetallic contaminants at the end of a tip, which is essential for performing STS. In addition, field emission cleaning is typically more consistent than cleaning a tip via electron beam bombardment. However, field emission cleaning can only be perofrmed a finite number of times, each field emision clean will remove material from the end of the tip. Field emission cleaning cannot be performed in an Omicron LT-STM with a QPlus preamplifier in the STM. The high currents and voltages required for field emission cleaning would damage the internal QPlus preamplifier. In the Omicron VT-STM in the Palmstrøm lab, field emission cleaning can be performed. However, modifications to the experimental set up are required to perform field emission cleaning.

The Omicron current preamplifier on the VT STM cannot be used for field emission cleaning and must be removed. Field emission cleaning adapter must be plugged into the STM where the preamplifier typically sits, this adapter shorts the internal I/V converter in the STM to prevent damage to it. The adapter is hooked up to an external current

preamplifer and voltage source. The current preamplifier must be able to measure several μA of current. The analog output of the current preamplifier is connected to an auxiliary input in the Nanonis STM control electronics, to enable feedback control of the piezo to maintain the field emission current. The tunnel voltage can then be applied between the tip and the sample, and then the feedback loop can be engaged to maintian a constant field emission current. Typical field emission cleaning parameters are a voltage of 200 V, with a current of 1 μA for 1 minute. Once field emission cleaning is performed, the adapter can be removed, and the original preamplifier can be connected to the system.

Bibliography

[1] H. Kroemer, Rev. Mod. Phys. **73**, 783 (2001).

[2] I. Vurgaftman, M. P. Lumb, and J. R. Meyer, *Bands and Photons in III-V Semiconductor Quantum Structures*, Oxford University Press, 2020.

[3] I.-H. Tan, G. L. Snider, L. D. Chang, and E. L. Hu, Journal of Applied Physics **68**, 4071 (1990).

[4] M. J. Manfra, Annual Review of Condensed Matter Physics **5**, 347 (2014).

[5] A. Manchon, H. C. Koo, J. Nitta, S. M. Frolov, and R. A. Duine, Nature Materials **14**, 871 (2015).

[6] E. Rashba, Sov. Phys.-Solid State **2**, 1109 (1960).

[7] G. Dresselhaus, Physical Review **100**, 580 (1955).

[8] S. D. Ganichev, V. V. Bel'kov, L. E. Golub, E. L. Ivchenko, P. Schneider, S. Giglberger, J. Eroms, J. De Boeck, G. Borghs, W. Wegscheider, D. Weiss, and W. Prettl, Physical Review Letters **92**, 256601 (2004).

[9] S. Giglberger, L. E. Golub, V. V. Bel'kov, S. N. Danilov, D. Schuh, C. Gerl, F. Rohlfing, J. Stahl, W. Wegscheider, D. Weiss, W. Prettl, and S. D. Ganichev, Physical Review B **75**, 035327 (2007).

[10] C. S. Knox, L. H. Li, M. C. Rosamond, E. H. Linfield, and C. H. Marrows, Physical Review B **98**, 155323 (2018).

[11] M. I. Dyakonov and V. Y. Kachorovskii, Soviet Physics: Semiconductors **20**, 110 (1986).

[12] S. M. Farzaneh, M. Hatefipour, W. F. Schiela, N. Lotfizadeh, P. Yu, B. H. Elfeky, W. M. Strickland, A. Matos-Abiague, and J. Shabani, Physical Review Research **6**, 013039 (2024).

[13] R. Winkler, *Spin-orbit Coupling Effects in Two-Dimensional Electron and Hole Systems*, Springer-Verlag Berlin, Heidelberg, 1 edition, 2003.

[14] G. Engels, J. Lange, T. Schäpers, and H. Lüth, Physical Review B - Condensed Matter and Materials Physics **55**, R1958 (1997).

[15] T. Schäpers, G. Engels, J. Lange, T. Klocke, M. Hollfelder, and H. Lüth, Journal of Applied Physics **83**, 4324 (1998).

[16] E. Bernardes, J. Schliemann, M. Lee, J. C. Egues, and D. Loss, Physical Review Letters **99**, 1 (2007).

[17] S. Datta and B. Das, Applied Physics Letters **56**, 665 (1990).

[18] S. Sugahara and J. Nitta, Proceedings of the IEEE **98**, 2124 (2010).

[19] P. Chuang, S.-C. Ho, L. W. Smith, F. Sfigakis, M. Pepper, C.-H. Chen, J.-C. Fan, J. P. Griffiths, I. Farrer, H. E. Beere, G. A. C. Jones, D. A. Ritchie, and T.-M. Chen, Nature Nanotechnology **10**, 35 (2015).

[20] M. I. Dyakonov and V. I. Perel, Fiz. Tverd. Tela. **13**, 3581 (1971).

[21] C. Nayak, S. H. Simon, A. Stern, M. Freedman, and S. Das Sarma, Rev. Mod. Phys. **80**, 1083 (2008).

[22] R. P. Feynman, International Journal of Theoretical Physics **21**, 467 (1982).

[23] D. Deutsch, Proc. R. Soc. Lond. A **400**, 97 (1985).

[24] P. W. Shor, Algorithms for quantum computation: discrete logarithms and factoring, in *Proceedings 35th Annual Symposium on Foundations of Computer Science*, pages 124–134, 1994.

[25] F. Arute, K. Arya, R. Babbush, D. Bacon, J. C. Bardin, R. Barends, R. Biswas, S. Boixo, F. G. S. L. Brandao, D. A. Buell, B. Burkett, Y. Chen, Z. Chen, B. Chiaro, R. Collins, W. Courtney, A. Dunsworth, E. Farhi, B. Foxen, A. Fowler, C. Gidney, M. Giustina, R. Graff, K. Guerin, S. Habegger, M. P. Harrigan, M. J. Hartmann, A. Ho, M. Hoffmann, T. Huang, T. S. Humble, S. V. Isakov, E. Jeffrey, Z. Jiang, D. Kafri, K. Kechedzhi, J. Kelly, P. V. Klimov, S. Knysh, A. Korotkov, F. Kostritsa, D. Landhuis, M. Lindmark, E. Lucero, D. Lyakh, S. Mandrà, J. R. McClean, M. McEwen, A. Megrant, X. Mi, K. Michielsen, M. Mohseni, J. Mutus, O. Naaman, M. Neeley, C. Neill, M. Y. Niu, E. Ostby, A. Petukhov, J. C. Platt, C. Quintana, E. G. Rieffel, P. Roushan, N. C. Rubin, D. Sank, K. J. Satzinger, V. Smelyanskiy, K. J. Sung, M. D. Trevithick, A. Vainsencher, B. Villalonga, T. White, Z. J. Yao, P. Yeh, A. Zalcman, H. Neven, and J. M. Martinis, Nature **574**, 505 (2019).

[26] P. W. Shor, Documenta Mathematica **1**, 467 (1998).

[27] P. W. Shor, Fault-tolerant quantum computation, in *Proceedings of 37th Conference on Foundations of Computer Science*, pages 56–65, 1996.

[28] A. Kitaev, Physics-Uspekhi **44**, 131 (2001).

[29] A. Kitaev, Annals of Physics **303**, 2 (2003).

[30] L. Fu and C. L. Kane, Physical Review Letters **100**, 096407 (2008).

[31] S. Mi, D. I. Pikulin, M. Wimmer, and C. W. J. Beenakker, Physical Review B **87**, 241405(R) (2013).

[32] Y. Oreg, G. Refael, and F. von Oppen, Physical Review Letters **105**, 177002 (2010).

[33] R. M. Lutchyn, J. D. Sau, and S. Das Sarma, Physical Review Letters **105**, 077001 (2010).

[34] S. Das Sarma and H. Pan, Phys. Rev. B **103**, 195158 (2021).

[35] S. Das Sarma and H. Pan, Phys. Rev. B **108**, 85415 (2023).

[36] S. Das Sarma, J. D. Sau, and T. D. Stanescu, Phys. Rev. B **108**, 85416 (2023).

[37] M. Aghaee, A. Akkala, Z. Alam, R. Ali, A. Alcaraz Ramirez, M. Andrzejczuk, A. E. Antipov, P. Aseev, M. Astafev, B. Bauer, J. Becker, S. Boddapati, F. Boekhout, J. Bommer, T. Bosma, L. Bourdet, S. Boutin, P. Caroff, L. Casparis, M. Cassidy, S. Chatoor, A. W. Christensen, N. Clay, W. S. Cole, F. Corsetti, A. Cui, P. Dalampiras, A. Dokania, G. de Lange, M. de Moor, J. C. Estrada Saldaña, S. Fallahi, Z. H. Fathabad, J. Gamble, G. Gardner, D. Govender, F. Griggio, R. Grigoryan, S. Gronin, J. Gukelberger, E. B. Hansen, S. Heedt, J. Herranz Zamorano, S. Ho, U. L. Holgaard, H. Ingerslev, L. Johansson, J. Jones, R. Kallaher, F. Karimi, T. Karzig, E. King, M. E. Kloster, C. Knapp, D. Kocon, J. Koski, P. Kostamo, P. Krogstrup, M. Kumar, T. Laeven, T. Larsen, K. Li, T. Lindemann, J. Love, R. Lutchyn, M. H. Madsen, M. Manfra, S. Markussen, E. Martinez, R. McNeil, E. Memisevic, T. Morgan, A. Mullally, C. Nayak, J. Nielsen, W. H. P. Nielsen, B. Nijholt, A. Nurmohamed, E. O'Farrell, K. Otani, S. Pauka, K. Petersson, L. Petit, D. I. Pikulin, F. Preiss, M. Quintero-Perez, M. Rajpalke, K. Rasmussen, D. Razmadze, O. Reentila, D. Reilly, R. Rouse, I. Sadovskyy, L. Sainiemi, S. Schreppler, V. Sidorkin, A. Singh, S. Singh, S. Sinha, P. Sohr, T. c. š. Stankevič, L. Stek, H. Suominen, J. Suter, V. Svidenko, S. Teicher, M. Temuerhan, N. Thiyagarajah, R. Tholapi, M. Thomas, E. Toomey, S. Upadhyay, I. Urban, S. Vaitiekėnas, K. Van Hoogdalem, D. Van Woerkom, D. V. Viazmitinov, D. Vogel, S. Waddy, J. Watson, J. Weston, G. W. Winkler, C. K. Yang, S. Yau, D. Yi, E. Yucelen, A. Webster, R. Zeisel, and R. Zhao, Phys. Rev. B **107**, 245423 (2023).

[38] Y. J. Chung, A. Gupta, K. W. Baldwin, K. W. West, M. Shayegan, and L. N. Pfeiffer, Phys. Rev. B **106**, 75134 (2022).

[39] J. E. Ayers, T. Kujofsa, P. Rago, and J. E. Raphael, *Heteroepitaxy of Semiconductors: theory, growth, and characterization*, CRC Press, Boca Raton, second edition, 2016.

[40] C. J. K. Richardson and M. L. Lee, MRS Bulletin **41**, 193 (2016).

[41] J. Tersoff, Applied Physics Letters **62**, 693 (1993).

[42] P. L. Gourley, T. J. Drummond, and B. Doyle, Applied Physics Letters **49**, 1101 (1986).

[43] W. Qian, M. Skowronski, and R. Kaspi, Journal of The Electrochemical Society **144**, 1430 (1997).

[44] G. Binning and H. Rohrer, Surface Science **126**, 236 (1983).

[45] J. Tersoff and D. R. Hamann, Physical Review B **31**, 805 (1985).

[46] M. J. Hÿtch, E. Snoeck, and R. Kilaas, Ultramicroscopy **74**, 131 (1998).

[47] M. J. Lawler, K. Fujita, J. Lee, A. R. Schmidt, Y. Kohsaka, C. K. Kim, H. Eisaki, S. Uchida, J. C. Davis, J. P. Sethna, and E. A. Kim, Nature **466**, 347 (2010).

[48] M. H. Hamidian, I. A. Firmo, K. Fujita, S. Mukhopadhyay, J. W. Orenstein, H. Eisaki, S. Uchida, M. J. Lawler, E. A. Kim, and J. C. Davis, New Journal of Physics **14**, 053017 (2012).

[49] I. Zeljkovic, D. Walkup, B. A. Assaf, K. L. Scipioni, R. Sankar, F. Chou, and V. Madhavan, Nature Nanotechnology **10**, 849 (2015).

[50] D. Walkup, B. A. Assaf, K. L. Scipioni, R. Sankar, F. Chou, G. Chang, H. Lin, I. Zeljkovic, and V. Madhavan, Nature Communications **9**, 1550 (2018).

[51] Z. Ren, H. Li, H. Zhao, S. Sharma, Z. Wang, and I. Zeljkovic, Nature Communications **12**, 10 (2021).

[52] M. Morgenstern, D. Haude, C. Meyer, and R. Wiesendanger, Physical Review B **64**, 205104 (2001).

[53] G. J. De Raad, D. M. Bruls, P. M. Koenraad, and J. H. Wolter, Physical Review B **66**, 195306 (2002).

[54] R. M. Feenstra, Y. Dong, M. P. Semtsiv, and W. T. Masselink, Nanotechnology **18**, 044015 (2007).

[55] L. J. van der PAUW, A METHOD OF MEASURING SPECIFIC RESISTIVITY AND HALL EFFECT OF DISCS OF ARBITRARY SHAPE, in *Semiconductor Devices: Pioneering Papers*, pages 174–182, WORLD SCIENTIFIC, 1991.

[56] P. T. Coleridge, R. Stoner, and R. Fletcher, Physical Review B **39**, 1120 (1989).

[57] P. T. Coleridge, Physical Review B **44**, 3793 (1991).

[58] H. Kosaka, A. A. Kiselev, F. A. Baron, K. W. Kim, and E. Yablonovitch, Electronics Letters **37**, 464 (2001).

[59] K. v. Klitzing, G. Dorda, and M. Pepper, Phys. Rev. Lett. **45**, 494 (1980).

[60] J.-M. Jancu, R. Scholz, E. A. de Andrada e Silva, and G. C. La Rocca, Physical Review B **72**, 193201 (2005).

[61] S. N. Holmes, P. J. Simmonds, H. E. Beere, F. Sfigakis, I. Farrer, D. A. Ritchie, and M. Pepper, Journal of physics: Condensed Matter **20**, 472207 (2008).

[62] C. Chen, I. Farrer, S. N. Holmes, F. Sfigakis, M. P. Fletcher, H. E. Beere, and D. A. Ritchie, Journal of Crystal Growth **425**, 70 (2015).

[63] F. Capotondi, G. Biasiol, D. Ercolani, and L. Sorba, Journal of Crystal Growth **278**, 538 (2005).

[64] M. Kawabe, M. Kondo, N. Matsuura, and K. Yamamoto, Japanese Journal of Applied Physics **22**, L64 (1983).

[65] D. S. Jiang, K. Kelting, T. Isu, H. J. Queisser, and K. Ploog, Journal of Applied Physics **63**, 845 (1988).

[66] J. D. Song, D. C. Heo, I. K. Han, J. M. Kim, Y. T. Lee, and S.-H. Park, Applied Physics Letters **84**, 873 (2004).

[67] S. Z. Ahmed, Y. Tan, J. Zheng, J. C. Campbell, and A. W. Ghosh, Physical Review B **106**, 035301 (2022).

[68] A. K. Rockwell, M. Ren, M. Woodson, A. H. Jones, S. D. March, Y. Tan, Y. Yuan, Y. Sun, R. Hool, S. J. Maddox, M. L. Lee, A. W. Ghosh, J. C. Campbell, and S. R. Bank, Applied Physics Letters **113**, 102106 (2018).

[69] M. G. Peters, B. J. Thibeault, D. B. Young, J. W. Scott, F. H. Peters, A. C. Gossard, and L. A. Coldren, Applied Physics Letters **63**, 3411 (1993).

[70] J. Jaroszyński, T. Andrearczyk, G. Karczewski, J. Wróbel, T. Wojtowicz, E. Papis, E. Kamińska, A. Piotrowska, D. Popović, and T. Dietl, Physical Review Letters **89**, 266802 (2002).

[71] M. Sundaram, S. A. Chalmers, P. F. Hopkins, and A. C. Gossard, Science **254**, 1326 (1991).

[72] H. L. Störmer, J. P. Eisenstein, A. C. Gossard, W. Wiegmann, and K. Baldwin, Physical Review Letters **56**, 85 (1986).

[73] J. H. Baskey, A. J. Rimberg, S. Yang, R. M. Westervelt, P. F. Hopkins, and A. C. Gossard, Applied Physics Letters **61**, 1573 (1992).

[74] T. Hoshino and N. Mori, Japanese Journal of Applied Physics **58**, SCCD10 (2019).

[75] N. Pant, W. Lee, N. Sanders, and E. Kioupakis, Applied Physics Letters **121**, 032105 (2022).

[76] F. Capotondi, G. Biasiol, I. Vobornik, L. Sorba, F. Giazotto, A. Cavallini, and B. Fraboni, Journal of Vacuum Science & Technology B **22**, 702 (2004).

[77] P. J. Simmonds, H. E. Beere, D. A. Ritchie, and S. N. Holmes, Journal of Applied Physics **102**, 083518 (2007).

[78] J. K. Luo, H. Thomas, S. A. Clark, and R. H. Williams, Journal of Applied Physics **74**, 6726 (1993).

[79] J. T. Dong, Y. Gul, A. N. Engel, T. A. J. van Schijndel, C. P. Dempsey, M. Pepper, and C. J. Palmstrøm, Phys. Rev. Mater. **8**, 64601 (2024).

[80] R. Nötzel, D. Eissler, M. Hohenstein, and K. Ploog, Journal of Applied Physics **74**, 431 (1993).

[81] O. Bierwagen, Y. I. Mazur, G. G. Tarasov, W. T. Masselink, and G. J. Salamo, Growth, Optical, and Transport Properties of Self-Assembled InAs/InP Nanostructures BT - Nanoscale Photonics and Optoelectronics: Science and Technology, in *Nanoscale Photonics and Optoelectronics*, edited by Z. M. Wang and A. Neogi, pages 157–218, Springer New York, New York, NY, 2010.

[82] D. M. Wood, A. Zunger, and D. Gershoni, Europhysics Letters **33**, 383 (1996).

[83] A. T. Hatke, M. A. Zudov, J. D. Watson, M. J. Manfra, L. N. Pfeiffer, and K. W. West, Physical Review B **87**, 161307(R) (2013).

[84] S. Das Sarma and F. Stern, Phys. Rev. B **32**, 8442 (1985).

[85] F. Stern and W. E. Howard, Physical Review **163**, 816 (1967).

[86] A. Gold, Physical Review B **35**, 723 (1987).

[87] H. Sakaki, T. Noda, K. Hirakawa, M. Tanaka, and T. Matsusue, Applied Physics Letters **51**, 1934 (1987).

[88] R. K. Jana and D. Jena, Applied Physics Letters **99**, 012104 (2011).

[89] G. Bastard, Applied Physics Letters **43**, 591 (1983).

[90] J. S. Hwang, W. Y. Chou, S. L. Tyan, H. H. Lin, and T. L. Lee, Applied Physics Letters **67**, 2350 (1995).

[91] W. Y. Chou, G. S. Chang, W. C. Hwang, and J. S. Hwang, Journal of Applied Physics **83**, 3690 (1998).

[92] G. S. Chang, W. C. Hwang, Y. C. Wang, Z. P. Yang, and J. S. Hwang, Journal of Applied Physics **86**, 1765 (1999).

[93] J. S. Hwang, G. S. Chang, W. C. Hwang, and W. J. Chen, Journal of Applied Physics **89**, 1771 (2001).

[94] A. Matthiessen and A. C. C. Vogt, Philosophical Transactions of the Royal Society of London **154**, 167 (1864).

[95] T. Achtnich, G. Burri, M. A. Py, and M. Ilegems, Applied Physics Letters **50**, 1730 (1987).

[96] S. F. Yoon, H. M. Li, K. Radhakrishnan, and D. H. Zhang, Journal of Crystal Growth **131**, 1 (1993).

[97] F. D. Schowengerdt, F. J. Grunthaner, and J. K. Liu, MRS Proceedings **144**, 201 (1988).

[98] D. K. Ferry, Physical Review B **17**, 912 (1978).

[99] A. Gold, Physical Review B **44**, 8818 (1991).

[100] A. Gold, Applied Physics Letters **92**, 082111 (2008).

[101] A. Gold, Journal of Applied Physics **108**, 063710 (2010).

[102] S. Das Sarma, M. P. Lilly, E. H. Hwang, L. N. Pfeiffer, K. W. West, and J. L. Reno, Physical Review Letters **94**, 1 (2005).

[103] M. J. Manfra, E. H. Hwang, S. Das Sarma, L. N. Pfeiffer, K. W. West, and A. M. Sergent, Physical Review Letters **99**, 5 (2007).

[104] L. Liu, Y. Gul, S. N. Holmes, C. Chen, I. Farrer, D. A. Ritchie, and M. Pepper, Applied Physics Letters **123**, 183502 (2023).

[105] K. Delfanazari, J. Li, Y. Xiong, P. Ma, R. K. Puddy, T. Yi, I. Farrer, S. Komori, J. W. A. Robinson, L. Serra, D. A. Ritchie, M. J. Kelly, H. J. Joyce, and C. G. Smith, Phys. Rev. Appl. **21**, 14051 (2024).

[106] K. S. Wickramasinghe, W. Mayer, J. Yuan, T. Nguyen, L. Jiao, V. Manucharyan, and J. Shabani, Applied Physics Letters **113**, 262104 (2018).

[107] T. Zhang, T. Lindemann, G. C. Gardner, S. Gronin, T. Wu, and M. J. Manfra, Phys. Rev. Mater. **7**, 56201 (2023).

[108] P. S. Eldridge, J. Hübner, S. Oertel, R. T. Harley, M. Henini, and M. Oestreich, Phys. Rev. B **83**, 41301 (2011).

[109] J. Pingenot and K. Mullen, arXiv , 1105.1804 (2011).

[110] M. E. Raikh and T. V. Shahbazyan, Phys. Rev. B **49**, 5531 (1994).

[111] T. Sander, S. Holmes, J. Harris, D. Maude, and J. Portal, Physical Review B - Condensed Matter and Materials Physics **58**, 13856 (1998).

[112] V. L. Gurevich and Y. A. Firsov, Soviet Phys. JETP **13**, 137 (1961).

[113] D. C. Tsui, T. Englert, A. Y. Cho, and A. C. Gossard, Phys. Rev. Lett. **44**, 341 (1980).

[114] V. Heine, Physical Review **138**, 1689 (1965).

[115] J. Bardeen, Physical Review **71**, 717 (1947).

[116] C. G. B. Garrett and W. H. Brattain, Physical Review **99**, 376 (1955).

[117] E. Litwin-Staszewska, W. Szymańska, and R. Piotrzkowski, Physica Status Solidi (b) **106**, 551 (1981).

[118] L. Shkedy, T. Markovitz, Z. Calahorra, I. Hirsh, and I. Shtrichman, Optical Engineering **50**, 061008 (2011).

[119] K. Ueno, E. G. Camargo, T. Katsumata, H. Goto, N. Kuze, Y. Kangawa, and K. Kakimoto, Japanese Journal of Applied Physics **52**, 092202 (2013).

[120] S. Datta, T. Ashley, J. Brask, L. Buckle, M. Doczy, M. Emeny, D. Hayes, K. Hilton, R. Jefferies, T. Martin, T. J. Phillips, D. Wallis, P. Wilding, and R. Chau, 85nm Gate Length Enhancement and Depletion mode InSb Quantum Well Transistors for Ultra High Speed and Very Low Power Digital Logic Applications, in *IEEE International Electron Devices Meeting*, pages 763–766, Washington, DC, USA, 2005, IEEE.

[121] M. Radosavljevic, T. Ashley, A. Andreev, S. D. Coomber, G. Dewey, M. T. Emeny, M. Fearn, D. G. Hayes, K. P. Hilton, M. K. Hudait, R. Jefferies, T. Martin, R. Pillarisetty, W. Rachmady, T. Rakshit, S. J. Smith, M. J. Uren, D. J. Wallis, P. J. Wilding, and R. Chau, High-Performance 40nm Gate Length InSb P-Channel

Compressively Strained Quantum Well Field Effect Transistors for Low-Power (V_{CC}=0.5V) Logic Applications, in *2008 IEEE International Electron Devices Meeting*, pages 1–4, San Francisco, CA, USA, 2008.

[122] J. A. del Alamo, Nature **479**, 317 (2011).

[123] J. Chochol, K. Postava, M. Čada, M. Vanwolleghem, L. Halagačka, J.-F. Lampin, and J. Pištora, AIP Advances **6**, 115021 (2016).

[124] Y. Ma, J. Zhou, J. Pištora, M. Eldlio, N. Nguyen-Huu, H. Maeda, Q. Wu, and M. Cada, Scientific Reports **6**, 38784 (2016).

[125] R. M. Lutchyn, E. P. A. M. Bakkers, L. P. Kouwenhoven, P. Krogstrup, C. M. Marcus, and Y. Oreg, Nature Reviews Materials **3**, 52 (2018).

[126] M. Pendharkar, B. Zhang, H. Wu, A. Zarassi, P. Zhang, C. P. Dempsey, J. S. Lee, S. D. Harrington, G. Badawy, S. Gazibegovic, R. L. M. Op het Veld, M. Rossi, J. Jung, A.-H. Chen, M. A. Verheijen, M. Hocevar, E. P. A. M. Bakkers, C. J. Palmstrøom, and S. M. Frolov, Science **372**, 508 (2021).

[127] A. E. G. Mikkelsen, P. Kotetes, P. Krogstrup, and K. Flensberg, Physical Review X **8**, 31040 (2018).

[128] C. F. McConville, T. S. Jones, F. M. Leibsle, and N. V. Richardson, Surface Science Letters **303**, L373 (1994).

[129] C. F. McConville, T. S. Jones, F. M. Leibsle, S. M. Driver, T. C. Q. Noakes, M. O. Schweitzer, and N. V. Richardson, Physical Review B **50**, 14965 (1994).

[130] G. Goryl, O. Boelling, S. Godlewski, J. J. Kolodziej, B. Such, and M. Szymonski, Surface Science **601**, 3605 (2007).

[131] A. A. Davis, R. G. Jones, G. Falkenberg, L. Seehofer, R. L. Johnson, and C. F. McConville, Applied Physics Letters **75**, 1938 (1999).

[132] T. S. Jones, C. F. McConville, F. M. Leibsle, and N. V. Richardson, Surface Review and Letters **1**, 513 (1994).

[133] P. R. Varekamp, M. Björkqvist, M. Göthelid, and U. O. Karlsson, Surface Science **350**, L221 (1996).

[134] M. O. Schweitzer, F. M. Leibsle, T. S. Jones, C. F. McConville, and N. V. Richardson, Surface Science **280**, 63 (1993).

[135] L. J. Whitman, J. A. Stroscio, R. A. Dragoset, and R. J. Celotta, Physical Review B **42**, 7288 (1990).

[136] T. Eguchi, T. Miura, S.-P. Cho, T. Kadohira, N. Naruse, and T. Osaka, Surface Science **514**, 343 (2002).

[137] J. Wever, H. L. Meyerheim, W. Moritz, V. Jahns, D. Wolf, H. Schulz, L. Seehofer, and R. L. Johnson, Surface Science **321**, L225 (1994).

[138] M. Björkqvist, M. Göthelid, L. Ö. Olsson, J. Kanski, and U. O. Karlsson, Journal of Vacuum Science & Technology B: Microelectronics and Nanometer Structures **14**, 957 (1996).

[139] M. Nishizawa, T. Eguchi, S.-i. Omoto, and T. Osaka, Applied Surface Science **122**, 204 (1997).

[140] J. Mäkelä, Z. S. J. Rad, J.-p. Lehtiö, M. Kuzmin, M. P. J. Punkkinen, P. Laukkanen, and K. Kokko, Scientific Reports **8**, 14382 (2018).

[141] R. M. Feenstra, Physical Review B **50**, 4561 (1994).

[142] K. C. Rajkumar, P. Chen, and A. Madhukar, Journal of Applied Physics **69**, 2219 (1991).

[143] C. D. Yerino, B. Liang, D. L. Huffaker, P. J. Simmonds, and M. L. Lee, Journal of Vacuum Science & Technology B: Microelectronics and Nanometer Structures **35**, 010801 (2019).

[144] W. K. Liu and M. B. Santos, Surface Science **319**, 172 (1994).

[145] J. T. Dong, H. S. Inbar, M. Pendharkar, T. A. J. van Schijndel, E. C. Young, C. P. Dempsey, and C. J. Palmstrøm, Journal of Vacuum Science & Technology B **41**, 32808 (2023).

[146] C. L. Littler and D. G. Seiler, Applied Physics Letters **46**, 986 (1985).

[147] R. M. Feenstra and P. Mårtensson, Physical Review Letters **61**, 447 (1988).

[148] N. Ishida, K. Sueoka, and R. M. Feenstra, Physical Review B - Condensed Matter and Materials Physics **80**, 075320 (2009).

[149] G. M. Guichar, C. A. Sebenne, and G. A. Garry, Physical Review Letters **37**, 1158 (1976).

[150] A. J. Noreika, M. H. Francombe, and C. E. C. Wood, Journal of Applied Physics **52**, 7416 (1981).

[151] A. Etchells and C. W. Fischer, Journal of Applied Physics **47**, 4605 (1976).

[152] A. Förster, A. Tulke, and H. Lüth, Journal of Vacuum Science & Technology B: Microelectronics and Nanometer Structures **5**, 1054 (1987).

[153] B. Akkal, Z. Benamara, B. Gruzza, and L. Bideux, Vacuum **57**, 219 (2000).

[154] P. D. C. King, T. D. Veal, M. J. Lowe, and C. F. McConville, Journal of Applied Physics **104**, 083709 (2008).

[155] J. C. Patrin, Y. Z. Li, M. Chander, and J. H. Weaver, Physical Review B **46**, 10221 (1992).

[156] J. P. Dismukes, R. J. Paff, R. T. Smith, and R. Ulmer, Journal of Chemical & Engineering Data **13**, 317 (1968).

[157] F. Schindler, Z. Wang, M. G. Vergniory, A. M. Cook, A. Murani, S. Sengupta, A. Y. Kasumov, R. Deblock, S. Jeon, I. Drozdov, H. Bouchiat, S. Guéron, A. Yazdani, B. A. Bernevig, and T. Neupert, Nature Physics **14**, 918 (2018).

[158] C. A. Hoffman, J. R. Meyer, F. J. Bartoli, A. Di Venere, X. J. Yi, C. L. Hou, H. C. Wang, J. B. Ketterson, and G. K. Wong, Phys. Rev. B **48**, 11431 (1993).

[159] F. Reis, G. Li, L. Dudy, M. Bauernfeind, S. Glass, W. Hanke, R. Thomale, J. Schäfer, and R. Claessen, Science **290**, 287 (2017).

[160] Y. M. Koroteev, G. Bihlmayer, E. V. Chulkov, and S. Blügel, Physical Review B **55**, 045428 (2008).

[161] Z.-q. Huang, F.-c. Chuang, C.-h. Hsu, Y.-t. Liu, H.-r. Chang, H. Lin, and A. Bansil, Physical Review B **88**, 165301 (2013).

[162] T. Zhou, S. Cheng, M. Schleenvoigt, P. Schüffelgen, H. Jiang, Z. Yang, and v. Igor, Physical Review Letters **127**, 116402 (2021).

[163] I. N. Yakovkin, Journal of Physical and Chemistry of Solids **129**, 277 (2019).

[164] J. T. Dong, H. S. Inbar, C. P. Dempsey, A. N. Engel, and C. J. Palmstrøm, Nano Letters **24**, 4493 (2024).

[165] M. König, S. Wiedmann, C. Brüne, A. Roth, H. Buhmann, L. W. Molenkamp, X.-l. Qi, and S.-c. Zhang, Science **318**, 766 (2007).

[166] L. Du, I. Knez, G. Sullivan, and R.-r. Du, Physical Review Letters **114**, 096802 (2015).

[167] S. Wu, V. Fatemi, Q. D. Gibson, K. Watanabe, T. Taniguchi, R. J. Cava, and P. Jarillo-Herrero, Science **359**, 76 (2018).

[168] S. Sun, J.-y. You, S. Duan, J. Gou, Y. Z. Luo, W. Lin, X. Lian, T. Jin, J. Liu, Y. Huang, Y. Wang, A. T. S. Wee, Y. P. Feng, L. Shen, J. L. Zhang, J. Chen, and W. Chen, ACS Nano **16**, 1436 (2022).

[169] T. Hirahara, G. Bihlmayer, Y. Sakamoto, M. Yamada, H. Miyazaki, S.-i. Kimura, S. Blügel, and S. Hasegawa, Physical Review Letters **107**, 166801 (2011).

[170] F. Yang, L. Miao, Z. F. Wang, M.-y. Yao, F. Zhu, Y. R. Song, M.-x. Wang, J.-p. Xu, A. V. Fedorov, Z. Sun, G. B. Zhang, C. Liu, F. Liu, D. Qian, C. L. Gao, and J.-f. Jia, Physical Review Letters **109**, 016801 (2012).

[171] T. Nagao, T. Doi, T. Sekiguchi, and S. Hasegawa, Japanese Journal of Applied Physics **39**, 4567 (2000).

[172] S. Hatta, Y. Ohtsubo, S. Miyamoto, H. Okuyama, and T. Aruga, Applied Surface Science **256**, 1252 (2009).

[173] F. Reis, *Realization and Spectroscopy of the Quantum Spin Hall Insulator Bismuthene on Silicon Carbide*, PhD thesis, Universität Würzburg, 2021.

[174] S. Yaginuma, T. Nagao, J. T. Sadowski, M. Saito, K. Nagaoka, Y. Fujikawa, T. Sakurai, and T. Nakayama, Surface Science **601**, 3593 (2007).

[175] T. Nagao, J. T. Sadowski, M. Saito, S. Yaginuma, Y. Fujikawa, T. Kogure, T. Ohno, Y. Hasegawa, S. Hasegawa, and T. Sakurai, Physical Review Letters **93**, 105501 (2004).

[176] J. S. Alden, A. W. Tsen, P. Y. Huang, R. Hovden, L. Brown, J. Park, D. A. Muller, and P. L. McEuen, Proceedings of the National Academy of Sciences of the United States of America **110**, 11256 (2013).

[177] M. R. Rosenberger, H. J. Chuang, M. Phillips, V. P. Oleshko, K. M. McCreary, S. V. Sivaram, C. S. Hellberg, and B. T. Jonker, ACS Nano **14**, 4550 (2020).

[178] D. Edelberg, H. Kumar, V. Shenoy, H. Ochoa, and A. N. Pasupathy, Nature Physics **16**, 1097 (2020).

[179] N. P. Kazmierczak, M. Van Winkle, C. Ophus, K. C. Bustillo, S. Carr, H. G. Brown, J. Ciston, T. Taniguchi, K. Watanabe, and D. K. Bediako, Nature Materials **20**, 956 (2021).

[180] M. H. Naik and M. Jain, Physical Review Letters **121**, 266401 (2018).

[181] D. Kang, Z. W. Zuo, Z. Wang, and W. Ju, RSC Advances **11**, 24366 (2021).

[182] L. Ju, Z. Shi, N. Nair, Y. Lv, C. Jin, J. Velasco, C. Ojeda-Aristizabal, H. A. Bechtel, M. C. Martin, A. Zettl, J. Analytis, and F. Wang, Nature **520**, 650 (2015).

[183] H. Yoo, R. Engelke, S. Carr, S. Fang, K. Zhang, P. Cazeaux, S. H. Sung, R. Hovden, A. W. Tsen, T. Taniguchi, K. Watanabe, G. C. Yi, M. Kim, M. Luskin, E. B. Tadmor, E. Kaxiras, and P. Kim, Nature Materials **18**, 448 (2019).

[184] L. Jiang, Z. Shi, B. Zeng, S. Wang, J.-h. Kang, T. Joshi, C. Jin, L. Ju, J. Kim, T. Lyu, Y.-r. Shen, M. Crommie, H.-j. Gao, and F. Wang, Nature Materials **15**, 840 (2016).

[185] L. Jiang, S. Wang, Z. Shi, C. Jin, M. I. B. Utama, S. Zhao, Y.-r. Shen, H.-j. Gao, G. Zhang, and F. Wang, Nature Nanotechnology **13**, 204 (2018).

[186] G. X. Ni, H. Wang, B. Y. Jiang, L. X. Chen, Y. Du, Z. Y. Sun, M. D. Goldflam, A. J. Frenzel, X. M. Xie, M. M. Fogler, and D. N. Basov, Nature Communications **10**, 1 (2019).

[187] N. Tilak, G. Li, T. Taniguchi, K. Watanabe, and E. Y. Andrei, Nano Letters **23**, 73 (2023).

[188] C. Liu, Y. Zhou, G. Wang, Y. Yin, C. Li, H. Huang, D. Guan, Y. Li, S. Wang, H. Zheng, C. Liu, Y. Han, J. W. Evans, F. Liu, and J. Jia, Physical Review Letters **126**, 176102 (2021).

[189] I. V. Lebedeva and A. M. Popov, Physical Review B **99**, 1 (2019).

[190] I. V. Lebedeva and A. M. Popov, Journal of Physical Chemistry C **124**, 2120 (2020).

[191] N. D. Lisgarten, S. J. Peppiatt, and S. J. R, Journal of Physics C: Solid State Physics **7**, 2263 (1974).

[192] G. Cantele and D. Ninno, Physical Review Materials **1**, 014002 (2017).

[193] I. K. Drozdov, A. Alexandradinata, S. Jeon, S. Nadj-Perge, H. Ji, R. J. Cava, B. A. Bernevig, and A. Yazdani, Nature Physics **10**, 664 (2014).

[194] B. Liu, T. Wagner, S. Enzner, P. Eck, M. Kamp, G. Sangiovanni, and R. Claessen, Nano Letters **23**, 3189 (2023).

[195] A. Gold and L. Calmels, Physical Review B **48**, 11622 (1993).